University of Stuttgart
Germany

Atom Probe Study on CuNi Thin Films-Miscibility Gap and Grain Boundary Segregation

Dissertation

Rüya Duran

Institute of Materials Science

Chair of Materials Physics

2023

Atom Probe Study on CuNi Thin Films- Miscibility Gap and Grain Boundary Segregation

Von der Fakultät Chemie der Universität Stuttgart zur Erlangung der
Würde eines Doktors der Naturwissenschaften (Dr. rer. nat.)
genehmigte Abhandlung

Vorgelegt von
Rüya Duran
Aus Cayiralan (Türkei)

Hauptberichter:	Prof. Dr. Dr. h. c. Guido Schmitz
Mitberichter:	Prof. Dr. Rainer Niewa
Prüfungsvorsitzende:	Prof. Dr. Cosima Stubenrauch

Tag der mündlichen Prüfung: 26.10.2023

Institut für Materialwissenschaft der Universität Stuttgart
2023

Atomsondentomographie an CuNi-Dünnschichten – Mischungslücke und Korngrenzsegregation

Von der Fakultät Chemie der Universität Stuttgart zur Erlangung der
Würde eines Doktors der Naturwissenschaften (Dr. rer. nat.)
genehmigte Abhandlung

Vorgelegt von
Rüya Duran
Aus Cayiralan (Türkei)

Hauptberichter:	Prof. Dr. Dr. h. c. Guido Schmitz
Mitberichter:	Prof. Dr. Rainer Niewa
Prüfungsvorsitzende:	Prof. Dr. Cosima Stubenrauch

Tag der mündlichen Prüfung: 26.10.2023

Institut für Materialwissenschaft der Universität Stuttgart

2023

Zusammenfassung

In dieser Arbeit wurde die Lage der Mischungslücke, und die Korngrenzsegregation im Legierungssystem, Kupfer-Nickel, per Atomsondentomographie (APT) analysiert.

Zur Untersuchung der Mischungslücke eines binären Systems mit langsamer Diffusion wurde ein neues Verfahren verwendet. Multilagen aus Cu- und Ni- Dünnschichten wurden mittels Ionenstrahlbeschichtung (IBS) auf Wolframpfosten beschichtet und durch fokussierte Ionenstrahlung (FIB) geformt. Bei drei unterschiedlichen Temperaturen, zwischen 573 und 673 K, wurden isotherme Auslagerungssequenzen an einem Ultrahochvakuumofen (UHV) durchgeführt und der Mischungsprozess analysiert. Ein Modell des Diffusionsprozesses wurde mittels mathematischer Überlegungen erstellt. Durch das Fitten der experimentellen Kompositions-profile mittels dieses Modells konnten die Gleichgewichtskonzentrationen der Schichten auch mit relativ kurzen Auslagerungszeiten ermittelt werden. Darüber hinaus konnten aus den diffusionskontrollierten Zeit- und Temperaturdaten physikalische Eigenschaften wie der effektive Diffusionskoeffizient (Gitterdiffusion einschließlich Defektdiffusion) bestimmt werden. Dieser betrug $D_{eff} = 1.86 \cdot 10^{-10}$ m^2/s $\cdot$ exp(−164 kJ mol^{-1}/RT). Während dem Vermischen wurde die Änderung der multilagigen Mikrostruktur bis zur vollständigen Mischung bei 623 und 673 K beobachtet, wobei Korngrenzen als schneller Diffusionsweg eine wichtige Rolle spielen. Bei 573 K wurde Nichtmischbarkeit experimentell deutlich nachgewiesen, wobei die Phasengrenzen bei c_{Ni}=26 at.% und c_{Ni}=66 at.% liegen. Mit diesen Phasengrenzen wurde die Mischungslücke über eine Redlich-Kister-Parametrisierung der Gibbs'schen freien Energie über den gesamten Konzentrationsbereich rekonstruiert. Hierin wurde für die kritische Temperatur, T_C, 608 K bei einer Konzentration von 45 at% Ni gefunden.

Im zweiten Teil wurde die Korngrenzsegregation durch die FIB/tEBSD- (Transmissions-Elektronen-Rückstreubeugung) Technik, in Korrelation zu APT-Messung charakterisiert. Vier Legierungen mit einem Ni-Anteil zwischen 25 und 85 at.% wurden auf Wolframpfosten per IBS beschichtet, und bei 700 K für 24 h wärmebehandelt. Die Segregation von Cu in die Korngrenzen wurde beobachtet. Durch die Verwendung eines theoretischen Models wurde die Exzess-Kurve über den

gesamten Konzentrationsbereich, und die Korngrenz-Formationsenergie auf Basis der experimentellen Daten berechnet.

Die tEBSD-Analyse während der FIB-Präparation erlaubt die Identifikation der Körner und deren Orientierung. Ein neues Verfahren wurde entwickelt, um mithilfe der Orientierung benachbarter Körner, Berechnungen zur Ermittlung der Korngrenzorientierung durchzuführen und somit die Orientierung natürlicher Korngrenzen zu bestimmen. Mit diesem Verfahren konnte der zeitliche Aufwand dieser anspruchsvollen Auswertung (verglichen zur herkömmlichen Methode mittels TEM-Untersuchung) stark reduziert werden, so dass eine quantitative Analyse vieler Korngrenzen möglich wurde. Aus den einzelnen Korngrenzorientierungen wurde die Korngrenzrotation, und die jeweiligen Anteile an Kippung und Drehung berechnet. Eine Abhängigkeit der Feststoffsegregation vom Kipp- und Drehanteil der Korngrenze wurde beobachtet, die am kleinsten für die reine Kipp- und Drehrotation war.

Die ermittelten Segregationsweiten sind signifikant größer als die strukturellen Korngrenzweiten und bewegen sich zwischen 12 und 85 Å. Dieses Verhalten wurde durch eine künstliche Verbreiterung der Korngrenze erklärt, die durch eine Flugbahnabweichung der Korngrenzatome während der Verdampfung verursacht wurde. Eine Korngrenzweite von w_0 = (10.1 ± 1.5) Å wurde für eine unverfälschte Korngrenze gefunden.

Abstract

In this work, the location of the miscibility gap, and the grain boundary (GB) segregation is analyzed via atom probe tomography (APT) on the Copper–Nickel system.

For the investigation of the miscibility gap of a binary system with slow diffusion, a new procedure was applied. Multilayers of Cu and Ni thin films were sputtered on Tungsten posts using Ion Beam Sputtering (IBS) and shaped via Focused Ion Beam (FIB) milling. At three different temperatures, between 573 and 673 K, isothermal annealing sequences were carried out in an Ultra-High Vacuum (UHV) furnace and the mixing process was analyzed. A model for the diffusion process was made using mathematical considerations. By fitting the experimental compositions profiles with this model, the equilibrium concentrations of the layers were determined, even though the annealing times were quite limited. Furthermore, from the diffusion-controlled kinetics, physical properties like the effective interdiffusion coefficient (lattice diffusion including defect diffusion) was determined, resulting in $D_{eff} = 1.86 \cdot 10^{-10}$ m^2/s $\cdot$ exp(-164 kJ mol^{-1}/RT). During the mixing experiment, the change of the multilayered microstructure to a homogeneous mixture was observed for 623 and 673 K, whereby grain boundaries play an important role as fast diffusion paths. At 573 K, immiscibility was clearly detected experimentally, localizing phase boundaries at c_{Ni}=26 at.% and c_{Ni}=66 at.%. With these phase boundaries, the miscibility gap was reconstructed, using a Redlich-Kister-Parametrization of the Gibbs free energy. Herein, its critical temperature, T_C, was found to be 608 K at a concentration of 45 at% Ni.

In the second part, GB segregation is characterized by means of a FIB/tEBSD (Transmission Electron Backscatter Diffraction) technique, in correlation with APT measurements. Four alloys with a Ni content between 25 and 85 at.% were sputtered onto Tungsten posts via IBS, and heat treated at 700 K for 24 h. A segregation of Cu to the GBs was observed. By using a theoretic model, the Excess-curve over the whole composition range and the GB formation energy was calculated, based on the experimental data.

The tEBSD analysis during FIB preparation allowed the identification of grains and their orientation. A new technique was developed to determine the grain boundary orientation by calculations considering the orientation of adjacent grains and thus, to determine the orientation

of natural grain boundaries. With this technique, the time effort of this challenging evaluation (in comparison to the usual method by TEM investigation) could be greatly reduced, making possible a quantitative analysis of multiple grain boundaries. From the individual GB orientations, the GB rotation was defined, and the tilt/twist fractions were calculated. A dependency of the solute segregation on the tilt- and twist fraction was observed. It is the lowest for pure tilt and twist rotations.

The segregation widths were found to range between 12 and 85 Å, being significantly larger than the structural GB width. This behaviour is explained by an artificial broadening of the GBs caused by trajectory aberrations of the GB atoms during evaporation. A GB width of w_0 = (10.1 ± 1.5) Å was found for the undistorted GBs.

Table of Contents

Zusammenfassung I

Abstract III

Table of Contents V

List of abbreviations VII

1 Introduction 1

2 Theoretical background 6

2.1 Thermodynamics of alloys 6

2.1.1 Phase diagrams 8

2.1.2 Phase boundaries in Cahn-Hilliard: thermodynamics of inhomogeneous systems 11

2.2 Diffusion in solids 13

2.2.1 Short circuit diffusion 14

2.2.2 Diffusion-controlled mixing 15

2.3 Grain Boundaries 16

2.3.1 Grain Boundary description 16

2.3.2 The structure of grain boundaries 17

2.3.3 Grain boundary orientation 19

2.3.4 Grain boundary plane orientation 23

2.3.5 Equilibrium GB segregation 26

2.3.6 GB segregation according to an extension of the Butler equation 30

2.3.7 GB segregation kinetics 31

2.4 The CuNi system 32

3 Experimental procedures 35

3.1 Electropolishing 35

3.2 Sample coating 36

3.2.1 Analysis of the miscibility gap 37

3.2.2 GB analysis 38

3.3 Annealing 39

3.4 Sample preparation 39

3.5 Electron backscatter diffraction (EBSD) 42

3.5.1 EBSD in transmission geometry (tEBSD) 44

3.5.2 Orientation determination by tEBSD 47

3.6 Atom Probe Tomography (APT) 49
  3.6.1 Reconstruction 50
  3.6.2 Detector efficiency 54
  3.6.3 Density artefacts in the reconstruction 55
4 Results and Discussion 57
4.1 Thickness calibration 57
4.2 Miscibility gap 58
  4.2.1 As prepared samples 59
  4.2.2 Isothermal development 61
  4.2.3 Microstructural change during annealing 65
  4.2.4 Determination of miscibility 68
  4.2.5 Determination of the diffusion coefficient 70
  4.2.6 Determination of the phase boundaries of the miscibility gap 74
4.3 Detector efficiency 81
4.4 Grain Boundary Segregation 83
  4.4.1 Density correction 84
  4.4.2 Grain boundary evaluation 86
  4.4.3 Grain boundary solute excess 87
  4.4.4 GB formation energy 91
  4.4.5 Segregation width 95
4.5 Grain Boundary Orientation 98
  4.5.1 Determination of the GB plane normal 98
  4.5.2 Correlation between atom probe and tEBSD 100
  4.5.3 Calculation of tilt and twist boundary contribution 102
  4.5.4 GB segregation: Dependency on the misorientation angle 103
  4.5.5 GB segregation: Dependency on the GB planes 106
  4.5.6 GB segregation: Dependency on tilt and twist contribution 108
5 Summary and conclusion 112
6 Bibliography 117
List of publications 1

List of abbreviations

AEM	Auger Electron Microscopy
APT	Atom Probe Tomography
CALPHAD	Calculation of Phase Diagrams
CI	Confidence Index
CSL	Coincidence Site Lattice
EAM	Embedded Atom Method
EBSD	Electron Backscatter Diffraction
EDX	Energy Dispersive X-ray Spectroscopy
FIB	Focused Ion Beam
GB	Grain Boundary
HAGB	High Angle Grain Boundary
HRTEM	High Resolution Transmission Electron Microscopy
IBS	Ion Beam Sputtering
IPF	Inverse Pole Figure
IQ	Image Quality
LAGB	Low Angle Grain Boundary
OIM	Orientation Map
PF	Pole Figure
PTE	Periodic Table of Elements
SEM	Scanning Electron Microscopy
SIMS	Secondary Ion Mass Spectroscopy
STEM	Scanning Transmission Electron Microscopy
tEBSD	Transmission Electron Backscatter Diffraction
TEM	Transmission Electron Microscopy
DIGM	Diffusion Induced Grain Boundary Migration
MD	Molecular Dynamics

1 Introduction

Nanocrystalline metals often show different physical properties, as compared to their coarse-grained equivalents. This is mostly due to the increased volume fraction of grain boundaries (GBs). GBs are known to be fast diffusion paths for atomic transport [1]. However, because of the GB Excess energy, the system's total energy is higher for nanocrystalline materials, and consequently the microstructure is not stable, tending to grain growth. This can be possibly inhibited by alloying the material with an element having a lower interfacial energy. The atoms of this component will segregate to the GBs and lower the GB- and so the system total energy [2].

A convenient model alloy, where this segregation phenomenon can be studied, is CuNi. Herein, Cu has the lower interfacial energy (γ_{Cu} = 1.83 Jm^{-2} < γ_{Ni} = 2.45 Jm^{-2}) and tent to segregate to the GBs [3]. Although CuNi alloys are well known material for technical applications, a detailed experimental investigation of its GB segregation behavior is missing. The reason is the difficulty of analyzing the composition of these defects in atomic resolution, since GBs have just a few atomic layers in thickness and are normally hidden in the bulk volume. Nevertheless, some attempts were made by intergranular fracturing and subsequent surface analysis through Auger Electron Microscopy (AEM) [4, 5] or Secondary Ion Mass Spectroscopy (SIMS) [6, 7]. A drawback of these destructive techniques is, that they are restricted to systems with brittle GBs. Additionally, metallic surfaces tend to oxidize quite fast, which will distort the GB composition. Another option are microscopic methods with ultra-high resolution, like high-resolution (HRTEM) or scanning transmission electron microscopy (STEM), combined with energy dispersive X-ray (EDX) analysis. Herein, precipitates and impurity sites can also be analyzed. However, this technique requires time-consuming sample preparation and the light elements cannot be analyzed via EDX. More important, the mentioned methods provide a two-dimensional analysis and therefore are just barely suitable for GBs, which are normally curved and twisted, especially in nanocrystalline materials [2].

Recently, Fischer et. al could predict GB segregation in CuNi for a simulated ideal GB using the embedded-atom-method (EAM) [8, 9]. It was found that the highest segregation of Cu was observed for Ni-rich compositions at low temperatures, close to the miscibility gap (Figure 1).

Additionally, a dependence of the segregation on the GB orientation was found. So, a high-energetic Σ5 GB had a ten-times higher segregation than a low-energetic coherent twin GB [8]. This result coincides with other theoretical research, that shows that the amount of segregation strongly depends on the grain boundary character and can be explained by the different atomic constellation of each GB leading to different site energies [10].

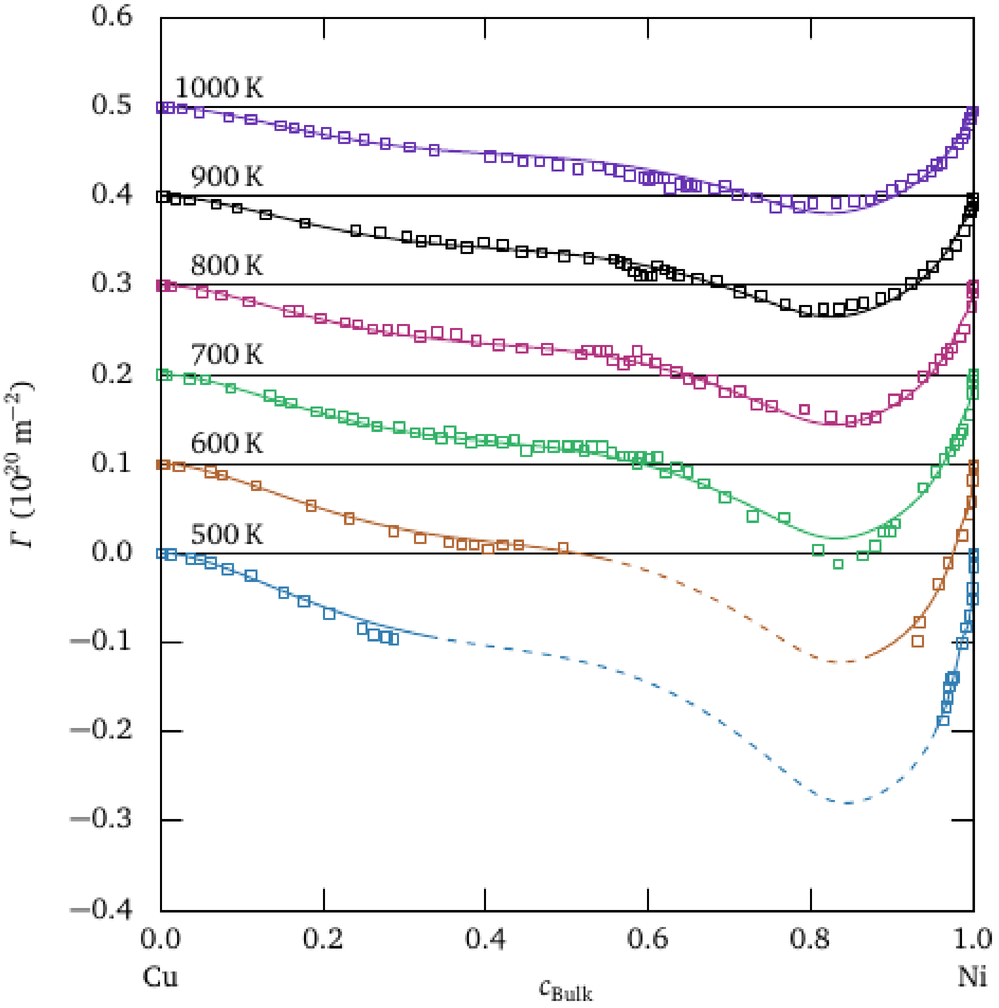

Figure 1: Simulated data for Cu solute excess at various temperatures for the CuNi alloy [9]. The dashed lines for 500K and 600K represent the miscibility gap (so no solute excess possible). The solute Excess describes the segregation of atoms of an element into a certain region, here, GBs. The negative values describe the depletion of Ni atoms, meaning the higher the absolute value, the higher the Cu segregation.

Although experimental research on GB segregation in dependence to the GB orientation is quite challenging, some investigations were made, using a correlative study of TEM and APT [11, 12]. A disadvantage is, however, the time-consuming sample preparation. The method requires the GB to be placed perpendicular to the surface for the TEM image, and the samples must be needle shaped for the following APT analysis. Therefore, the GB of interest is first isolated from a bulk sample and arranged to be perpendicular to the surface. Then, it's placed on an APT sample post and shaped to a nanometer-sized needle, having a diameter of around 100nm for TEM measurement, and afterwards thinned again to remove the residues from TEM analysis before it is measured by APT. Therefore, the analysis of large amounts of GBs is not possible which prevents quantitative research. As a simplification, Babinsky et. al presented a correlative technique, where the GB orientation can be determined just during the APT sample preparation [13]. By using Electron Backscattered diffraction (EBSD) the grain orientation is determined during the FIB cut. From this, the GB orientation might be calculated by matrix algebra.

For the already mentioned theoretical work of Fischer et. al, pair potentials are necessary, which can be calibrated from Redlich-Kister parametrizations of the Gibbs free energy, considering contributions of the mixing enthalpy. Therefore, the materials mixing behavior is of great interest. However, for CuNi alloys, the mixing tendency at low temperatures is still controversial. Although the existence of a miscibility gap is clear, the exact temperature and composition range could not be clarified. The very slow kinetics at low temperatures prevent direct experimental measurements of the phase boundaries being carried out in reasonable times. Therefore, available analysis was made by theoretical modelling and only indirect experimental investigations. This led to the apparent variation in a wide range of different solubility boundaries, without clear evidence [14, 15, 16, 17]. Some exemplary miscibility gaps from former studies are shown in Figure 2 to demonstrate the variation in temperature and composition.

To fill this gap of information, the present experimental investigations on the miscibility gap and GB segregation was undertaken. Both investigations need high resolution in chemical analysis. Therefore, Atom Probe Tomography (APT) is excellently suitable. This technique provides a sub-nanometer resolution in all three dimensions and chemical analysis in single atom sensitivity. With its three-dimensional tomographic reconstruction, it is ideal for finding nanometer-sized features hidden in a volume and analyzing their composition directly.

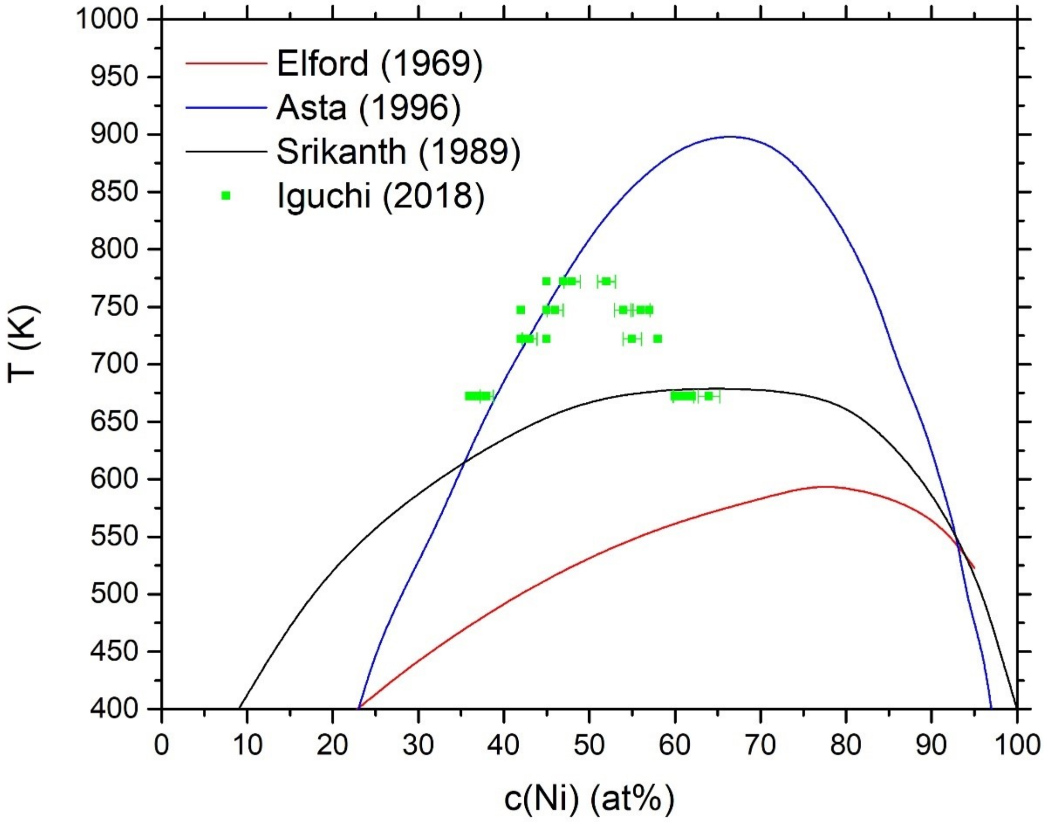

Figure 2: Some example diagrams for the variety of found miscibility gaps taken from [14, 15, 16, 17]

In the first part of this work, the phase boundaries of the miscibility gap in the CuNi system are determined. Therefore, both alloying components were deposited on substrates and annealed in an ultra-high-vacuum (UHV) oven at different temperatures until thermodynamic equilibrium was reached. The main difficulty was the reasonable reduction of the annealing times. This was accomplished by using thin film configurations of just a few nanometer thicknesses to shorten the diffusion length. Since the diffusion of Cu in Ni is 1000 times slower than vice versa [18], additional pre-alloying of Ni with Cu was performed for partly compensating this asymmetric diffusivity. In case that equilibrium has been still not reached, the diffusion process was modelled mathematically, and fitted to the experimental composition profiles. By this, the equilibrium concentrations were also determined theoretically. As a further result, the effective interdiffusion coefficient *D* was determined, confirming wether the selected annealing times are sufficient. *D* describes the diffusion in both directions, Cu into Ni and Ni into Cu, and includes all kinds of defect transport of the nanocrystalline microstructure (GB and dislocation diffusion). The statistical significance is increased by using multi-layered diffusion couples with 10 or 20 layers of each. With the received phase boundaries, the Redlich-Kister coefficients were determined and the whole miscibility gap over the bulk concentration was calculated.

In the second part of the work, the concentration dependency of GB segregation was quantitatively investigated and described by thermodynamic models. For this purpose, homogeneous thin film layers of CuNi with different concentrations were deposited and annealed for 24 h at 700 K, until thermodynamic equilibrium. The GB segregation was determined as the solute excess. With these results, and by using an extension of the Langmuir-McLean segregation model, the excess over the full concentration range was modelled. Combining the results with the Redlich-Kister parametrization of the miscibility gap obtained in the first part of this work, the change in the GB formation energy with bulk concentration was calculated and compared to data of simulated GBs taken from [9]. As a final investigation, an attempt was made to determine the orientation dependency of the experimental GB segregation. Therefore, the method introduced by Babinsky et al. [13] was used to determine the grain orientations during FIB-cutting of the APT tip. For the determination of the GB orientation, a new procedure is established which calculates the GB plane orientation from the three-dimensional reconstruction of the APT measurement and expresses it in relation to its adjacent grain orientations, determined by tEBSD.

2 Theoretical background

Metals have a characteristic atomic structure, stemming from the specific metallic bonding, consisting of an ordered array of the positively charged atom cores and their valence electrons (electrons from the outermost shell), surrounding them in form of an electron gas. Thereby, the metal cores are periodically arranged to a lattice with the unit cell as the smallest repetition unit. If this lattice is undisturbed, the array is called a single crystal or a grain. A material structure can typically consist of several grains, being differently oriented to each other. These materials are called polycrystalline. The atoms localized at the border of the two adjacent grains don't fit into the periodic arrays and are therefore in a less ordered environment. This region is the so-called grain boundary (GB) [19].

2.1 Thermodynamics of alloys

Alloys are mixtures of two or more elements, with at least one metal and the atoms of the other elements are distributed in the lattice of the metal. Due to the metallic bonding, alloys still have metallic properties. Depending on the alloyed component, the mechanical properties can be largely modified. A well-known example for this is steel, where the alloying of iron with small amounts of carbon increases the hardness by orders of magnitude [20, 21].

Alloys may decompose into heterogeneity, consisting of different phases. The transformation between the phases can be predicted via thermodynamic calculations. Thermodynamics follow the rule that a system is trying to reach the state of highest probability. This state is defined over the Gibbs free energy $G = H - TS$. A driving force toward phase transformation is only given if G is reduced. So, the change in the Gibbs free energy is defined as:

$$\Delta G = \Delta H - T\Delta S. \tag{1}$$

where H is the enthalpy, describing the heat/energy content of a system consisting of the kinetic and potential energies of the systems atoms, and S the entropy, which is a measure of the molecular disorder.

Having achieved energetic minimum, G doesn't change anymore, meaning $dG = 0$. Then, the system is in thermodynamic equilibrium and stable.

In binary systems, the Gibbs energy not only depends on the average energy of the pure components, but also on the change of the Gibbs energy when mixing takes place, ΔG_{mix}. So, G of a binary system is expressed as:

$$G = x_A G_A + x_B G_B + \Delta G_{mix} \tag{2}$$

Where ΔG_{mix} is defined as:

$$\Delta G_{mix} = \Delta H_{mix} - T\Delta S_{mix}. \tag{3}$$

With x_A and x_B as the molar fractions of element 1 and 2, and ΔH_{mix} and ΔS_{mix} denoting the heat and entropy difference between the pure and the mixed state [21].

When both elements form a homogeneous solution at every composition and temperature, total miscibility is given, and the system is described as an *ideal solution*. In this case, no difference in the heats of mixed and unmixed state are given and $\Delta H_{mix} = 0$. Therefore, according to Eq. (3), ΔG_{mix} is only affected by the change in entropy. Generally, ΔS_{mix} is a sum of the thermal and configurational entropy. However, the thermal entropy, which describes the additional disorder caused by the vibration spectrum, is largely independent of the mixing state and so only the configurational entropy becomes relevant, which is the entropy, stemming from the different arrangement of the alloyed species. If a substitutional lattice is built (where all atomic neighborhoods are equally possible), ΔS_{mix} is defined as:

$$\Delta S_{mix} = k_B \ln \frac{(N_A + N_B)!}{N_A! N_B!} \tag{4}$$

With k_B as the Boltzmann's constant and $N_{A,B}$ as the number of A and B atoms. By further simplification, using the Avogadro's number, N_a, the universal gas constant R, and the Stirling's approximation, ΔG_{mix} of an ideal system becomes:

$$\Delta G_{mix} = TR(x_A \ln x_A + x_B \ln x_B), \tag{5}$$

with $x_{A,B}$ as the molar fraction of element A and B [21].

However, when the mixing of two elements requires or provides heat, a heat term must be included. For binary systems with equal atomic volumes of both elements, it's assumed that the creation of new bond types is responsible for ΔH_{mix}. Then, the bond energies of a binary alloy, stem from the balance of bonding between like atoms, A-A and B-B, and the bonding between different species, A-B. A convenient parameter to understand the thermodynamics is the pair exchange parameter:

$$\varepsilon = \varepsilon_{AB} - \frac{1}{2}(\varepsilon_{AA} + \varepsilon_{BB}), \tag{6}$$

where ε_{AA}, ε_{BB} and ε_{AB} are the bond energies between the respective atoms. Note, that the bonding energies are negative values and that, the stronger the bonding, the higher the absolute value. For $\varepsilon < 0$, the contribution of ε_{AB} is dominant, leading to a preferred bonding between the atoms of different kind. For $\varepsilon > 0$, in contrast, ε_{AA} and ε_{BB} have a higher (negative) contribution, and therefore bonding to equal atoms is preferred. The mixing enthalpy, ΔH_{mix}, is then calculated, in the pair bond model to:

$$\Delta H_{mix} = N_a z \varepsilon x_A x_B, \tag{7}$$

with *z* being the number of bonds per atom (coordination). Inserting Eq.(7) in Eq.(3) defines the change of the mixing Gibbs free energy as [21]:

$$\Delta G_{mix} = N_a z \varepsilon x_A x_B + TR(x_A \ln x_A + x_B \ln x_B). \tag{8}$$

2.1.1 Phase diagrams

Phase diagrams are generated by plotting the free energy curves of all phases as a function of the composition for each temperature in the same plot (at constant pressure). The curve minima and the interceptions of the curves represent the phase boundaries. This procedure is presented in Figure 3 for a system being miscible in the liquid state and containing a miscibility gap in the solid state. Starting at high temperatures, above the melting temperatures, T_m, of the pure elements, both, the free energy curves of the solid (blue) and liquid (red) phase are positively curved with the solid phase having higher Gibbs energies at each composition (Fig. 3a). Since the liquid phase has the lower energy, it is stable at this temperature for all compositions. With decreasing temperature, G of the liquid phase increases faster than G of the solid phase, leading to an intersection of both curves at pure A, which represents the melting point of Element A (Fig. 3b). Reducing the temperature further causes a cross-over of the solid and liquid curves, as shown in Fig. 3c, which indicates a two-phase region. By using the common tangent method, the three regions may be distinguished by their compositions. Between pure A and the point, a, the liquid phase is energetically favored, between b and B the solid phase and between a and b a two-phase region. By further decreasing the temperature, G of the liquid phase becomes higher than G of the solid phase, having an interception of the curves, only at pure B, representing the melting point of compound B (Fig. 3d). Finally, the temperature is reduced so much that the Gibbs free energy of the solid phase is always lower than the one of liquid phase (Fig. 3e), a single solid phase is stable. Depending on the curvature of the Gibbs energy, another two-phase region might be present, which is also known as a miscibility gap. If the mixing enthalpy of the solid phase is positive, which happens due to preferred bonding between like atoms, the Gibbs energy curve will become negatively curved for sufficient low temperatures and intermediate compositions, as shown in Fig. 3f. In this case, two local energy minima coexist, leading to the formation of two solid phases, whereas the composition in-between is not stable due to the high energy costs. The local minima are approximately the compositions of the stable phases, and the system tends to demix for the compositions c to d, exactly defined by the touching points of the common tangent.

Now, by plotting the characteristic points of the free energy curves in a temperature-composition map, the phase diagram is generated, as shown in Fig. 3g [21].

Phase diagrams can also be prepared over computational methods. This is the CALPHAD (calculation of phase diagrams) approach, which uses thermodynamic considerations for calculating the phase equilibria of the system. Since G is a function of temperature, pressure and composition, its dependency on these variables must be defined [22]. The temperature dependency is described by a series of temperature functions resulting in the heat capacity according to [23, 24]:

$$C_p = m_3 + m_4 T + m_5 T^{-2} + m_6 T^2 + \cdots. \tag{9}$$

with m_i as adoptable coefficients.

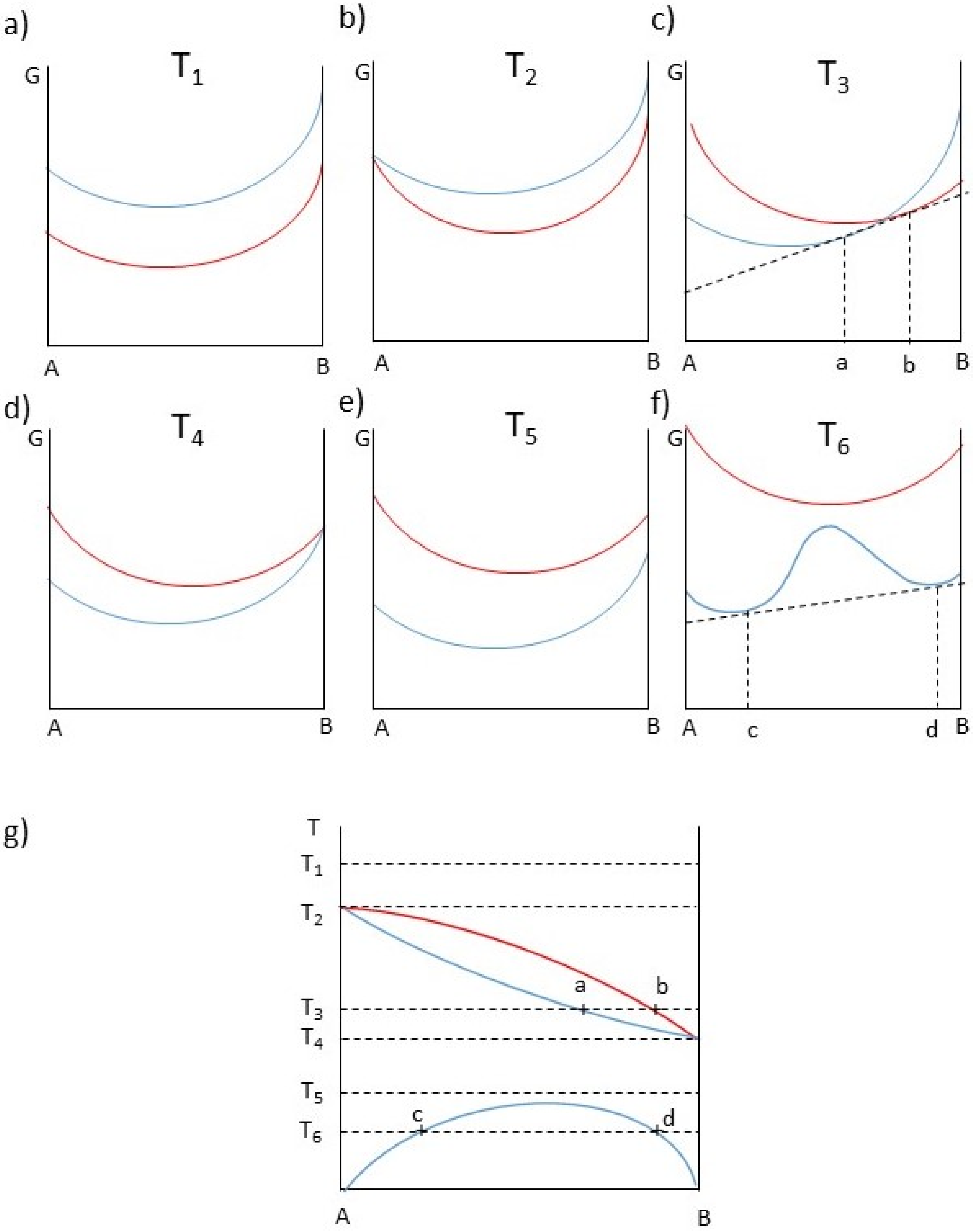

Figure 3: Construction procedure of a phase diagram for an alloy, containing a miscibility gap. a-f show the Gibbs free energy curves of the solid (blue) and liquid (red) phase at characteristic temperatures. g is the created phase diagram containing the specific points generated by interceptions of the both Gibbs free energy curves in a-f.

The pressure dependency is given as:

$$-R\ ln\left(\frac{p}{p_0}\right) \tag{10}$$

And the composition dependency as:

$$g = x_A g_A + x_B g_B + R(x_A lnx_A + x_B lnx_B) + g_{ex} \tag{11}$$

In this equation, the first two terms describe the mechanic mixing, the third the ideal solution and the last term is the excess Gibbs energy, which is generally given as a Redlich-Kister polynomial according to [23, 25]:

$$g_{ex} = x_A x_B \sum_{i=0}^{n} L_i (x_A - x_B)^i, \tag{12}$$

with L_i as free coefficients adapted to measured data.

Using this formula and fitting it to experimentally determined physical properties results in an optimized set of thermodynamic parameters for modelling the full range of the phase diagram and giving additional information about the remaining unknown parameters [26].

2.1.2 Phase boundaries in Cahn-Hilliard: thermodynamics of inhomogeneous systems

A mathematical approach to describe the interface between two phases was given by Cahn and Hilliard [27].

Herein, the local free energy of a binary system with a spatial change of the composition (at the interface) was calculated. The introduction of an interphase into an undisturbed system increases the total free energy.

It was shown that the total free energy of a volume, *F*, can be expressed as a sum of two contributions. One is the free energy that the volume would have if it would be homogeneous, f_0, and the other one is the gradient energy being a function of the local composition variation $\kappa(\nabla c)^2$. For cubic lattices, the general equation maybe formulated as:

$$F = N_V \int_V \left[f_0 + \kappa(\nabla c)^2\right] dV \tag{13}$$

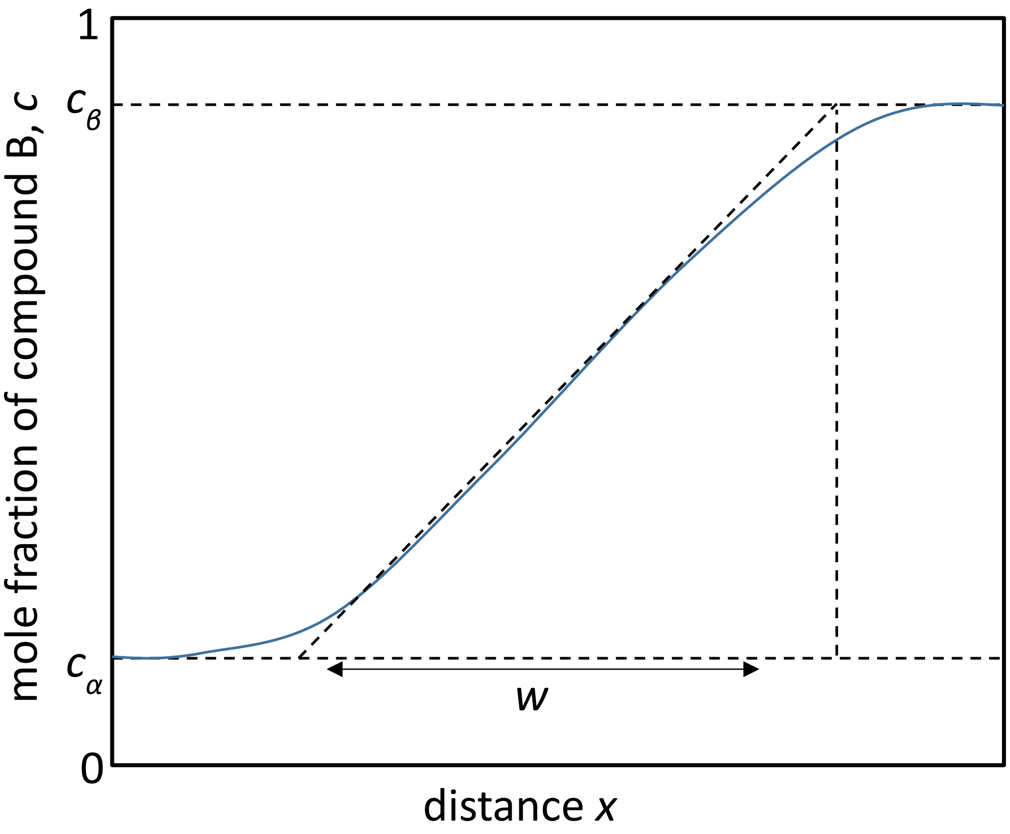

Figure 4: Representation of the interface width w of a material with a flat interface as a function of the composition of component B [27]

With N_V as the number of molecules per unit volume and κ as the gradient energy coefficient. With the definition of the interfacial free energy, σ, and by expanding f_0 in a Taylor series, the composition variation at a flat interface can be expressed as:

$$c(x) = 1 - \frac{2}{\exp\left(\frac{-4x}{w}\right)+1}. \tag{14}$$

Here, $c(x)$ is the normalized composition, with:

$$c(x) = \frac{\tilde{c}(x)-c_\alpha}{c_\beta-c_\alpha}. \tag{15}$$

c_α and c_β are defined according to Figure 4. The interface width, which is defined as *w* in Eq. (14), is given as

$$w_{(T\sim T_c)} = 2\sqrt{\frac{2\kappa}{\beta(T_c - T)}}, \tag{16}$$

near the critical temperature, T_c. β is a constant, which is defined from the curvature of the free energy as $\beta = \left(\frac{\partial^2 f_0}{\partial T \partial c^2}\right)\frac{1}{2!}$. Eq.(16) shows that with increasing temperature, the interface thickness increases, too, and is maximal for $T = T_c$.

2.2 Diffusion in solids

The phenomenological description of diffusional fluxes is given by the Fick's laws. The Fick's first law describes the flux of diffusing atoms driven by a concentration gradient, with the diffusion coefficient *D* as a proportionality factor (Eq.(18)). The Fick's second law considers the conservation of matter. This means, the balance of income and outcome flux *j* in a certain volume is equal to the time-dependent concentration change, according to:

$$\frac{\partial c}{\partial t} = -\frac{\partial j}{\partial x} \tag{17}$$

with

$$j = -D\frac{\partial c}{\partial x} \tag{18}$$

as the diffusion flux. This means, diffusion is a concentration dependent kinetic process. Since atomic jumps need thermal activation, it is temperature dependent. Therefore, the diffusion coefficient is often presented in an Arrhenius dependency:

$$D = D_0 \exp\left(-\frac{H}{RT}\right), \tag{19}$$

with D_0 as the pre-exponential factor and *H* as the activation enthalpy.

To describe the diffusional process by Fick laws usually boundary and initial (*t* = 0) conditions are defined, representing the experimental setup, like the finite/infinite source of diffusant. As an example, the diffusant can be deposited as a thin layer on the surface of a sample (finite source), or by joining two materials differing in their composition (infinite source) in a diffusion couple. For both examples, diffusion takes place in one direction but with different diffusant amounts. If the diffusant source is inside the sample as a slab or as a 3-dimensional structure, diffusion in two or more directions takes place. Thus, the concentration flow is modeled either as an exponential or a periodic function [28].

For a multilayer stack, as it is the case for the samples used in this project, the diffusant source is a periodic, plane layer with a finite amount of diffusant atoms. Its time-dependent concentration profile can be described therefore by harmonic oscillations that are increasingly damped. So, the concentration profile can be mathematically described by a Fourier series:

$$c(z,t) = \bar{c} + \sum_{n=1}^{\infty} e^{-(\frac{2\pi n}{\delta})^2 Dt}\, a_n \cos\left(\frac{2\pi n}{\delta}(z - z_0)\right), \tag{20}$$

where the Fourier coefficient a_n are obtained by integrating the starting profile as:

$$a_n = \frac{2(c_1 - c_2)}{\pi n}\sin(\frac{\pi n \delta_1}{\delta}) = \frac{2(c_1 - c_2)}{\pi n}\sin(\frac{\pi n(\bar{c} - c_1)}{(c_1 - c_2)}). \tag{21}$$

With $\bar{c}$ as the mean concentration, c_1 and c_2 as the initial layer concentrations of the periods δ_1 and δ_2, $\delta = \delta_1 + \delta_2$ as the period of the whole profile and z_0 as the spatial offset [26].

2.2.1 Short circuit diffusion

In metals, the periodically atomic structure of crystals is disturbed by interstitials or vacancies. These point defects generally make diffusion possible and partly belong to the thermal equilibrium. Beside these point defects, metals often contain dislocations and GBs, which were proven to accelerate diffusion and increase the diffusivity. In these disturbed lattice regions, the atomic transport may be easier due to the less dense atomic packing caused by distortion. In general, the diffusivities can be ordered as follows:

$$D_{\text{crystal}} < D_{\text{dislocation}} < D_{\text{GBs}}$$

The diffusion in a single crystal is controlled by pure bulk diffusion, meaning here, the diffusion is the slowest. The diffusivity increase, with increasing dimensionality of the defect since the constraints of the diffusing atoms decrease. This means, that GB diffusion is the fastest transport mechanism inside a material possibly elevated by many orders of magnitude with respect to the bulk. Especially in nanomaterials, the atomic transport in GBs is of huge importance. Here, the volume fraction of GBs is so large that GB diffusion is the rate-determining step and controls the material properties and the material stability (due to grain growth for example). Figure 5 shows a comparison of the GB and bulk diffusion coefficients for the transport process of Ni in Cu in a polycrystalline thin film investigated by Johnson et al. [18]. Obviously, the GB diffusion is 100000 times faster than bulk diffusion.

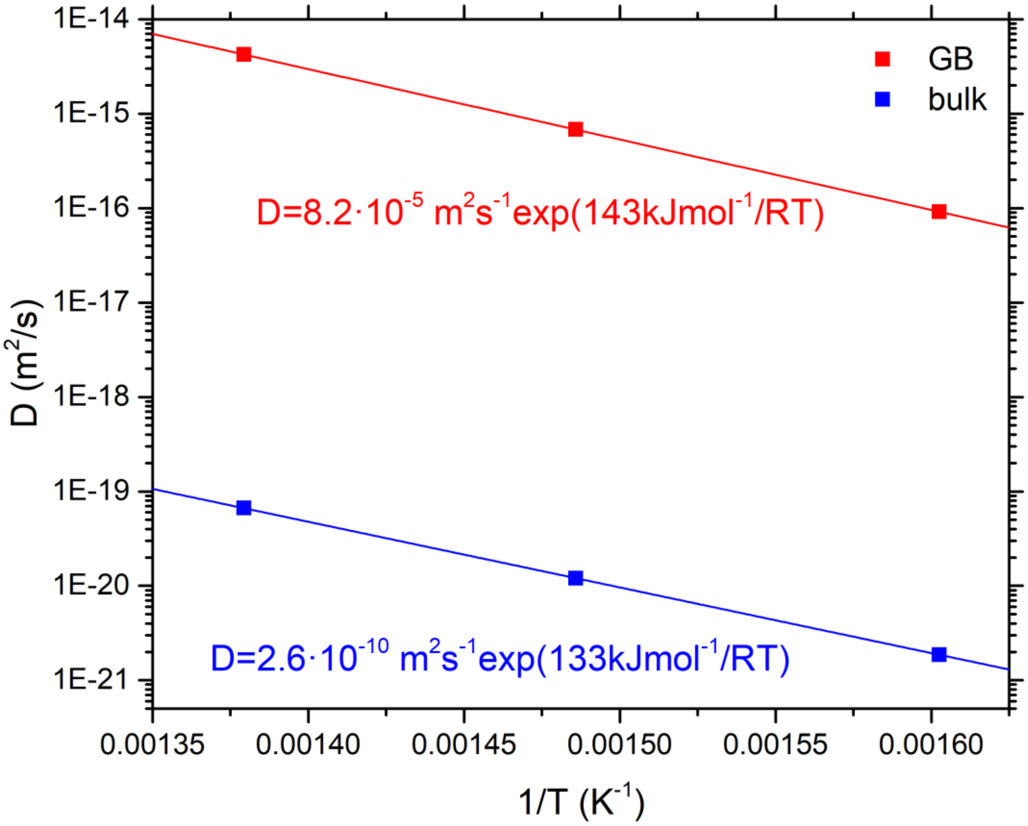

Figure 5: Arrhenius plots of diffusion data comparing GB and bulk diffusion for the transport of Ni into Cu [18].

2.2.2 Diffusion-controlled mixing

By allowing diffusion for an infinitely long time, the system will reach thermodynamic equilibrium. Even in a fully miscible system, a single phase with homogeneous distribution, a solid solution may be produced over nucleation and growth processes if bulk mobility is limited. Herein, the new (mixed) phase is first nucleated at a high energetic region, like GBs, phase boundaries or dislocations. Via GB transport, atoms will diffuse to this nucleus which will grow. During this process, the volume of the freshly generated phase will grow. This process usually requires interface migration. In case of a nucleation at a GB, the process is termed diffusion induced GB migration (DIGM). Since the development of the new phase with different composition will need long-range diffusion of the surrounding atoms, the growth rate of the phase can still be controlled by the crystal (or lattice) diffusion. In this case, the intermixing is called to be diffusion controlled. The alternative is the interface-controlled intermixing, which is the case, when atomic transport across the interface is the rate-determining step [21, 29].

2.3 Grain Boundaries

Depending on their dimensionality, crystal defects are classified in point defects (0-dimensional), line defects (1-dimensional) and planar defects (2-dimensional). Point defects are e.g. vacancies or interstitials. Here, either an atom is missing at a certain lattice position, or an additional atom is present in-between the lattice sites. All crystals contain a certain number of these defects in thermodynamic equilibrium. They play an important role in diffusion, since they enable the position exchange of atoms. Most prominent line defects are dislocations, the border of incomplete lattice planes, located in-between the atomic planes of the ideal crystal. They are responsible for easy gliding of atomic planes, so for plastic deformation in crystals. Planar defects are e.g. grain boundaries. Due to the high number of GBs, the atomic transport in polycrystalline materials is typically faster than in single crystals, especially when the grain sizes are small, leading to different physical properties. Therefore, these materials have their own classification, being known as nanomaterials [30, 31].

2.3.1 Grain Boundary description

Grain boundaries separate two grains of different orientation. This means, that already three degrees of freedom (DOF) are necessary to describe the misorientation between the adjacent grains (for example by defining a rotation axis and angle to bring both grains in coincidence). Additionally, GBs are planar defects, which can be differently oriented in the three-dimensional space. This orientation can be described by the planes normal vector, so additional two DOF. In total, five DOFs are necessary to fully define a GB, which can be unambiguously denoted in the form $\vartheta°[hkl](h_1k_1l_1)/(h_2k_2l_2)$, with $\vartheta°$ being the misorientation angle, [hkl] the misorientation axis, being identical for both grains and $(h_1k_1l_1)/(h_2k_2l_2)$ being the GB plane, being (redundantly) expressed in the lattice systems of both grains. Due to the numerous amounts of GBs, they were evaluated not individually, but by grouping them into classes with structural similarities, like the GB type (tilt and twist boundaries) their symmetry or the size of the misorientation angle [2].

2.3.2 The structure of grain boundaries

In GBs, the atoms are not arranged in regularly ordered patterns as it is the case for crystals. Instead, it was believed that GBs are regions of atomic disorder. Therefore, the GB types were characterized according to the symmetry operation necessary to bring the adjacent grains into coincidence. Thus, an important property is the orientation of the rotation axis, which can be in two prominent cases either perpendicular or parallel to the GB plane. If the rotation axis is perpendicular to the GB plane, the GB is called a twist grain boundary. If the rotation axis is parallel, a tilt grain boundary. Depending on the GB plane, tilt GBs are further divided into symmetrical and asymmetrical. When the adjacent grains are mirror imaged at the GB, the GB is symmetrical, else it is asymmetrical. Natural GBs often have facetted contributions from both. Then, they are called random or mixed GBs [30, 2].

Another classification is made according to the misorientation angle. GBs with angles smaller than 15° are understood as low-angle grain boundaries (LAGBs). The misorientation of these GBs is so small that a kind of periodicity is still given, and the GBs are described as an array of dislocations. While tilt GBs are built of edge dislocations, twist GBs consist of screw dislocations. For LAGBs, the GB energy can be calculated using the dislocation model from Read and Shockley. GBs with misorientation angle above 15° are termed high-angle grain boundaries (HAGBs). For these, the dislocation model fails due to the high density of dislocations which are overlapping, so that they cannot be considered as individual defects anymore. Nevertheless, the atoms in HAGBs are not randomly distributed in the GB, but follow a periodic arrangement of a few building units, which differ from the LAGBs. Considering that atoms have energy-efficient positions in ideal crystals, the total energy of the system will increase when the atom positions deviate from these. To keep the energy as low as possible, the system tends to place the atoms on these ideal positions, even in the GB. This means that crystallographic planes exist, that even extend beyond GBs and that the atomic positions of these crystallographic planes located at the GB are called coincidence sites. Since the crystal lattice is periodic, the coincidence sites must be periodic, too, spanning a lattice, known as the coincidence site lattice (CSL). The inverse fraction of the coincidence sites is given according to:

$$\Sigma \mathrm{n} = \frac{V_{CSL}}{V_{crystal}} \tag{22}$$

With V_{CSL} as the volume of the CSL unit cell and $V_{crystal}$ as the volume of the crystal lattice unit cell. This equation means, that every nth lattice site is a coincidence site. So, the smaller n, the higher is the GB periodicity and typically the lower the energy costs for the system.

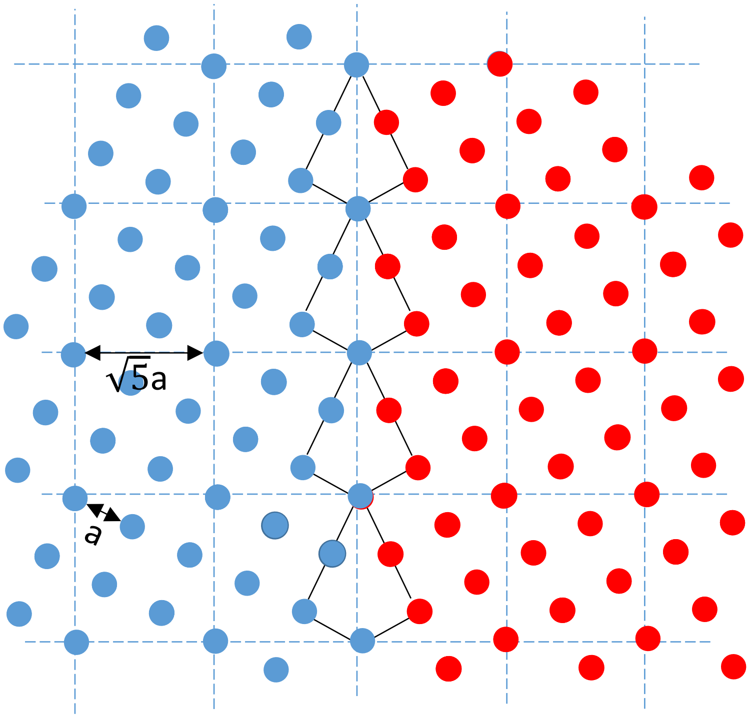

Figure 6: Schematic CSL of a symmetric Σ5 tilt GB (36.9° (100)) in an fcc lattice with the GB plane perpendicular to the paper plane. Every 5th atom of grain 1 (blue) and grain 2 (red) coincides (marked in black lines). The CSL unit cells are marked by blue dashed lines [30].

An example of a CSL lattice is given in Figure 6 for a GB in a fcc-lattice with a rotation of 36.87° around a (100)-axis. At the GB plane, which is normal to the sheet plane, every 5th atomic position belongs to the crystallographic sites of both grains. According to Eq. (22), it's $(\sqrt{5}a)^2 a/a^3$, and therefore it is a $\Sigma 5$-GB. The dashed lines indicate the CSL lattice [30].

2.3.3 Grain boundary orientation

Generally, a grain orientation is described as the alignment of the unit cell coordinate system in a reference coordinate system. The reference system, on the other hand, is linked to the specimen orientation. For simplification, the specimen coordinate system which can be chosen arbitrary, is arranged according to the sample geometry or the processing directions. For a flat rolled specimen, for example, it is usual to mark the direction normal to the surface (ND) as the z-axis, the rolling direction (RD) as the x-axis and the transverse direction (TD) as the y-axis (Figure 7). In case of wire samples, the wire axis can be used as z direction, whereas the perpendicular axis can be selected arbitrarily.

Considering that the unit cell has its own coordinate system, its directions can be easily adapted, if the lattice symmetry is orthonormal, like in case of a cubic lattice. For a hexagonal or trigonal lattice, however, first, an orthogonal frame and a normalization of the axis must be carried out by multiplying the coordinate axes with a suitable transformation matrix. With both coordinate systems being orthonormal, the orientation can be expressed as a rotation to transfer the specimen coordinate system (C_S) to the crystal coordinate system (C_C) according to:

$$C_C = C_S \cdot g \tag{23}$$

With g being the rotation matrix. In g, every row stands for the direction cosine of the three crystal axes to the specimen coordinate system, whereas every column stands for the direction cosine of the specimen axes to the crystal coordinate system (see Figure 7). With this matrix, a rotation is unambiguously defined. However, since the definitions of both coordinate systems are not unique, different ways for representing the crystallographic orientation are possible [32].

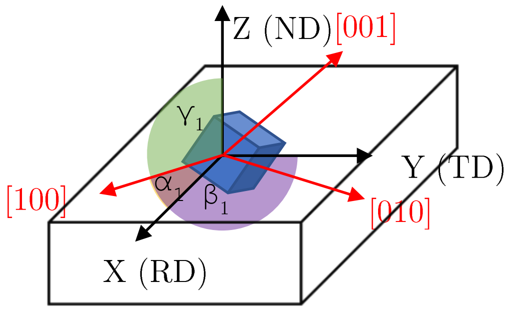

$$\begin{array}{cccccc} & X & Y & Z & & \\ & \downarrow & \downarrow & \downarrow & & \\ g = & \left(\begin{matrix} cos\alpha_1 \\ cos\alpha_2 \\ cos\alpha_3 \end{matrix}\right. & \begin{matrix} cos\beta_1 \\ cos\beta_2 \\ cos\beta_2 \end{matrix} & \left.\begin{matrix} cos\gamma_1 \\ cos\gamma_2 \\ cos\gamma_3 \end{matrix}\right) & \begin{matrix} \leftarrow \\ \leftarrow \\ \leftarrow \end{matrix} & \begin{matrix} [100] \\ [010] \\ [001] \end{matrix} \end{array}$$

Figure 7: Relation between specimen (black) and crystal (red) coordinate system. The angles between the [100]-crystal directions and the sample coordinate axes are colored. They form the direction cosine of this crystal direction and build the first row of the rotation matrix (left).

The crystallographic directions are normally given as Miller Indices, in which a coordinate system is defined according to the crystals unit cell and the plane sets are expressed by their reciprocal interception points with the coordinate axis. For defining the grain orientation, one method is to define the crystal direction being parallel to the sample x axis, and a crystal plane parallel to the sample z direction. This correspondent to the first and third column of the rotation matrix. Then, the orientation is expressed as (hkl)[uvw]. For non-cubic crystals, however, the relation between Miller Indexing and rotation matrix is more complex and so this definition becomes inconvenient.

Another representation is the use of angle/axis pairs. Since for every rotation a common axis exists, which is identical for the reference and the rotated volume, a rotation can be expressed by this common (rotation) axis and the rotation angle, according to $\theta/(r_1r_2r_3)$. Angle/axis pairs are frequently used for representing misorientations (orientation of one grain expressed in relation to the other grain), since they are very convenient for grain relationships.

By using this notation, the specific orientations of the GBs are given. However, due to crystal and sample symmetry, the designation of orientation relation is not unique, and the same orientation can be expressed in different ways by using alternative equivalent rotation axis. Therefore, the angle/axis pair with the smallest rotations angle (also known as disorientation) is taken to limit the possibilities [32, 30].

2.3.3.1 Orientation representation: spherical and stereographic projection

The orientation of crystals in 3-D space is described via plane normal vectors of each crystallographic plane. For this process, a reference sphere is used, which surrounds the crystal. By extending the crystals plane normal vectors to intersect with the reference sphere surface (pole), a spherical projection is obtained (Figure 8a).

Usually, the crystallographic orientation is presented two-dimensionally. For that, the spherical projection needs to be converted onto a plane. In crystallography, the stereographic projection is used most often, since it displays angular relationships (Figure 8b). An orientation given by spherical projection can be achieved as follows: The south pole of the reference sphere (S) is used as the point of projection for poles being on the northern hemisphere and the north pole (N) as point of projection for poles on the southern hemisphere. The crystal lies in the center and the equatorial plane is the plane of projection. The pole P intersects the reference sphere at a certain point. By connecting this pole with the south pole, an intersect point (p) on the equatorial plane occurs, which is the stereographic projection of the pole.

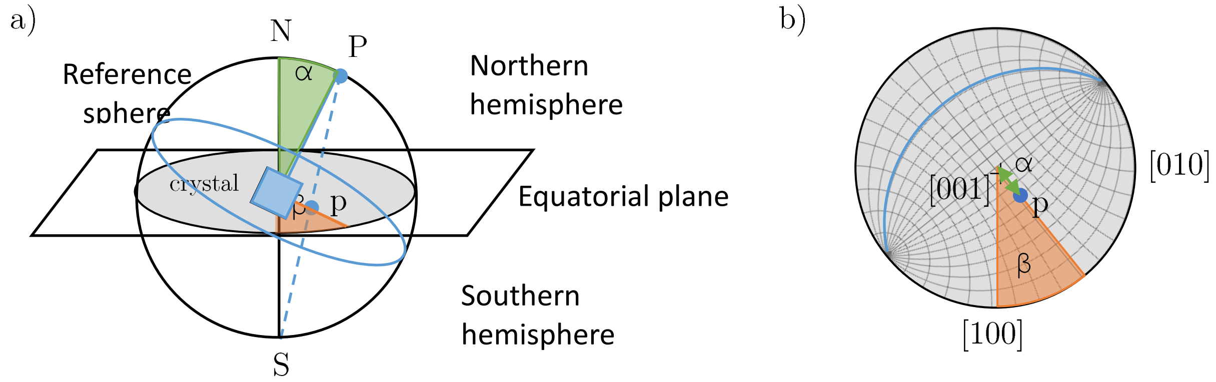

Figure 8: a) Scheme of the spherical projection with the crystal (blue cube) in the center of the reference sphere with north pole (N), south pole (S), pole (P), plane trace (blue arch) and the projection of the Pole on the equatorial plane (p) to construct a stereographic projection. b) Stereographic projection of pole p from a) with plane trace (blue arc) and the angles α (green line) and β (orange segment).

Another possibility is to define the plane over its plane trace, which passes through the sphere center (blue arc in Figure 8). It is the intersection line of the crystal plane with the reference sphere. The resulting line is called zone line. Since the zone line represents a plane, the angle in between two poles lying at the same plane can be measured along the trace line, whereas its pole is orthogonal and has always an angle of 90° to the trace (Figure 8b). The top view of this plane is the stereographic projection.

A pole is uniquely defined by two angles, one, describing the angle to the north pole α, and another one describing the angle to the equatorial axis β. For determining the angles, a Wulff net can be used which is a grid constructed of several plane traces dividing the stereographic projection in equal angular pieces.

For orthogonal crystals, like cubic crystals, it is convenient to arrange the [001] crystal axis to the north pole ($\alpha = 0°$), the [100] axis to be vertical ($\beta = 0°$) and the [010] axis to be horizontal ($\beta = 90°$), so that [100] shows to the bottom and [010] to the right in the stereographic projection (Figure 8b). It is easy to draw the {110} poles in this projection since they have a 45° angle to these axes. Considering the orthogonality of the axes, the {111} poles can be received by a linear combination of {100} and {110} and can be drawn at the interception of traces connecting these poles. The obtained stereographic projection, shown in Figure 9 is divided into 24 triangles, each with {001}, {011} and {111} poles at their corners. These triangles represent the cubic symmetry meaning, the triangles are crystallographically equivalent. So, it’s already enough to use only one (unit) triangle for displaying all crystallographic directions [32]. The stereographic projections can also be presented with other poles being at the center. Therefore, the pole is simply rotated to the projection center [30].

For representing the orientation, however, one pole is not sufficient since the crystal might still rotate around this pole. So, for unambiguity, at least one additional pole of the same {hkl} family is necessary. For that, pole figures are used, which are stereographic projections of several poles where the spatial arrangement between the poles is included considering the sample coordinate system. If vice versa the pole figure of the sample coordinate axis is shown relative to the crystal coordinate system, then the inverse pole figure is generated. Inverse pole figures are generally used for measuring changes of orientation according to a sample axis of interest, like a mechanical stressed axis or a wire axis [32].

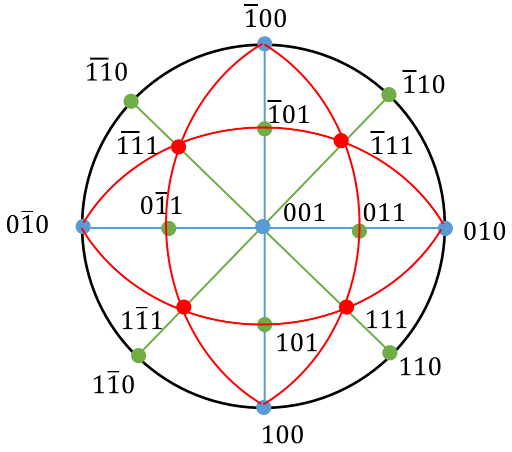

Figure 9: Stereographic projections of an fcc crystal with {001} at the center

2.3.4 Grain boundary plane orientation

With the grain orientations, the three DOFs for misorientation are determined. For a complete characterization of GB orientation, however, the grain boundary plane orientation must be defined, which requires a three-dimensional characterization. For the investigation of specific grain boundaries, this task was fulfilled by producing artificial GBs from bicrystals with known crystal orientation and with predefined planes [33, 34]. Methods for characterizing the orientation of naturally occurring GBs are techniques based on diffraction patterns, obtained with TEM or SEM. For TEM, the GB plane is received by tilting the sample, until the interface width between the adjoining grains becomes lowest. Then, the GB normal is perpendicular to the beam and the normal vector can be calculated by the tilt angle on the goniometer [35]. However, the analysis via TEM needs samples with limited thickness in the nanometer range. This means, the sample preparation is very time-consuming, since the GB of interest probably had to be cut from a bulk material. Additionally, the GB must be visible in the SEM, for the cutting step. However, this is not the case for nanometer-sized grains since the SEM resolution is limited.

Another technique, using the diffraction patterns for orientation determination is the analysis via SEM, making use of the EBSD. To measure the GB plane orientation, an inclination angle must be determined which describes the tilt of the GB plane relative to the sample depth direction. The inclination angle is determined by the ‘two-surface trace analysis’-method which was first introduced by Andrejeva et al. [36] for GB orientation measurements using x-ray diffraction and implemented later to electron microscopy by Randle et al. [35]. In this process, a GB containing specimen with orthogonal surfaces (like a rectangle, for example) is tilted in a way, that a common edge between two orthogonal surfaces is perpendicular to the electron beam. Then, both surfaces are showing to the electron beam and the diffraction patterns of the grains can be analyzed on both surfaces simultaneously at the common edge. Since the GB plane is also visible on both surfaces, the inclination angle can be determined according to trigonometric considerations as shown in Figure 10 [35].

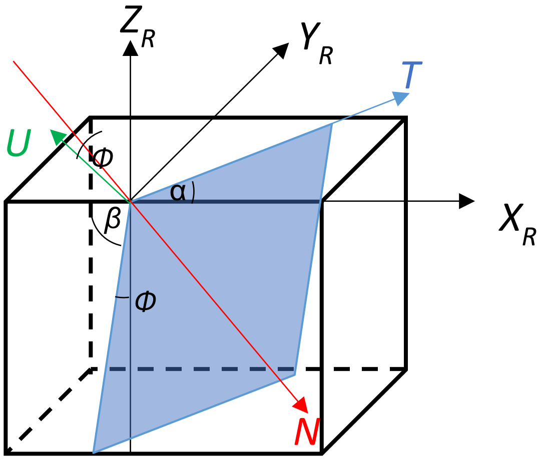

Figure 10: Illustration of a GB plane together with the trigonometric considerations for calculating the plane orientation according to [35]. $X_RY_RZ_R$ are the specimen reference axes. α is the angle between the GB trace T and the X_R-axis on the surface. β is the angle of the GB plane with the X_R -axis and ϕ is the inclination angle. N is the plane normal and U the direction perpendicular to T on the xy-plane.

Alternatively, the GB plane can be determined from the pole figures of the adjacent grains. This procedure is a further development of the ‘two-surface trace analysis’-method from Mandal [37] and is shown in Figure 11. Herein, first, the misorientation angle and axis were determined, which is automatically done by the EBSD analysis software, and the CSL-type is received. The pole figures of the adjacent grains are plotted onto the same Wulff net, and the GB trace is drawn into it. Since the GB plane normal is perpendicular to the trace, a line perpendicular to the trace line is drawn.

By using the GB inclination angle, which is an angle formed by the same GB on two surfaces of a rectangular sample geometry at the common edge (α in Figure 11), the poles of both grains are marked, which overlap with the inclination angle. These poles describe the GB plane normal in relation to the axes of both grain orientations.

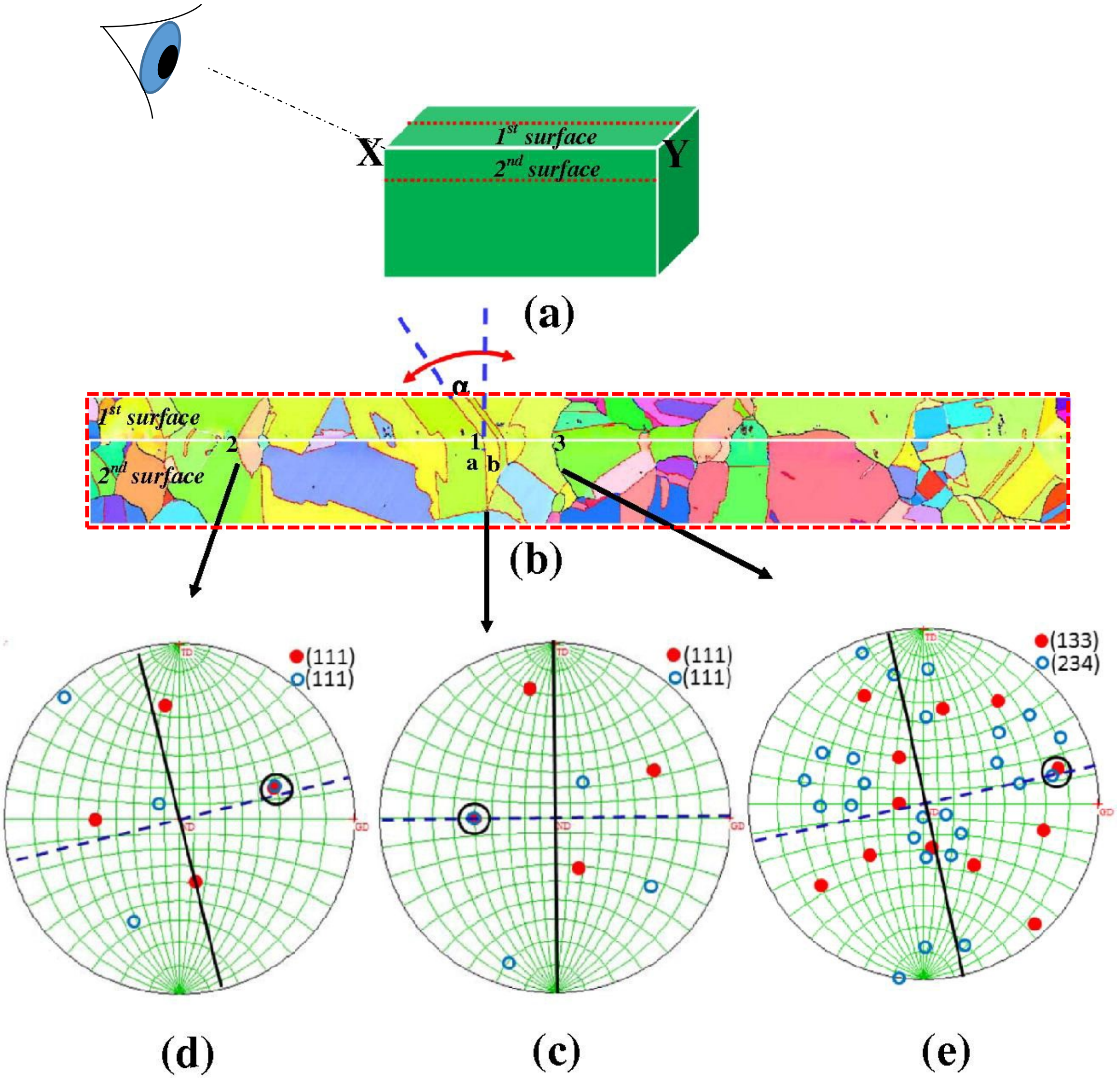

Figure 11: Determination of the GB plane normal by using the 'two-surface trace analysis'-method and pole figures of the adjacent grains. (a) is a scheme of the specimen box with the two surfaces and the sharp edge (XY) used for EBSD analysis (surrounded by a red dotted line). (b) is the IPF map of the marked region in (a) with α as the inclination angle between both surfaces. Three GBs are numbered. (c-e) show the pole figures of the adjacent grains (red and blue dots) for GB1-3. The GB trace line (black), the GB plane normal (dashed blue line) and α (open black circle) are marked. The intersection of the GB trace and α with the poles of both grains indicate the GB plane normal according to the grain's orientation [37].

In Figure 11a, the specimen box is shown as a green cuboid and the common edge for EBSD analysis is marked between the 1st and 2nd surface. Figure 11b shows the inverse pole figure (IPF) map of this region. As can be seen, a GB trace is continuously visible on both surfaces, but having a certain inclination angle α between the traces at both sides of the common edge. The pole figures of some selected GBs are shown in c), d) and e) for the GBs 1, 2 and 3. The GB trace line (black) and the plane normal line (dashed blue line) for a coherent twin boundary (c), a coherent twin with deviation (d) and a random HAGB are shown. Note, that for the coherent twin boundary the poles defining the GB plane normal are identical and therefore overlapping, whereas they are different for the HAGB [37]. A disadvantage of this procedure is, that the GB must be accessible from two perpendicular and even planes. Therefore, this method cannot be used for non-cuboid specimens.

Using the same EBSD-technique, a further way for analyzing the GB plane orientation was introduced, but not demonstrated by Babinsky et. al [13]. Herein, just the grain orientations are determined by EBSD. With the additional measurement of the sample via a three-dimensional method, like the atom probe tomography (APT), the GB plane normal can be calculated with the orientation information gained from the EBSD.

2.3.5 Equilibrium GB segregation

Polycrystalline materials have an increased total free energy, due to the higher energy costs of grain boundaries with respect to an ideal crystal. However, alloys have the possibility to reduce this energy by segregation of the species with the lower surface energy towards the GBs, which is known as GB segregation. By this, the chemical composition of grains and GBs will vary [2].

2.3.5.1 Thermodynamics

A thermodynamic description of interfaces (grain boundaries) was first established by Gibbs [38, 39]. He defined it as an inhomogeneous thin layer, a dividing surface, separating the masses of two fluids. The total energy of the system is given by the internal energy U as:

$$\mathrm{d}U = T\mathrm{d}S - P\mathrm{d}V + \textstyle\sum_{i=1}^{N} \mu_i dn_i + \gamma dA. \tag{24}$$

Were P is the pressure, V the Volume, μ_i the chemical potential of the i^{th} (i=1,2, …, N) component, A the GB area and γ the GB formation energy. An ideal system (without GB) would not contain the last term on the RHS of this equation. So, this term is the additional energy-increase for a system containing an interface. It is defined as the change of internal energy per GB unit area. By using thermodynamic conversions, the upper equation can be rewritten in:

$$\mathrm{d}\gamma = -\textstyle\sum_i \Gamma_i \mathrm{d}\mu_i, \tag{25}$$

which is the well-known Gibbs adsorptions isotherm. It describes the decrease of the GB formation energy in relation to the solute excess Γ_i of each component *i*, which stands for the number of segregated atoms per GB area [39]. Therefore, a polycrystalline system might be stabilized by GB segregation. Note that Eq. (25) is generally not valid for solid but fluid systems. According to [40] [41], for solid systems, a term considering the GB tension must be included. However, for binary systems with atoms of nearly the same radii, and therefore no lattice mismatch, this GB tension can be neglected, according to:

$$\mathrm{d}\gamma = -\Gamma \mathrm{d}\Delta\mu + \textstyle\sum_{i=1,2}(\tau_{ii} - \gamma)\mathrm{d}\varepsilon = \left(-\Gamma \frac{\partial \Delta\mu}{\partial c} + \sum_{i=1,2}(\tau_{ii} - \gamma)\left(\frac{\partial \varepsilon}{\partial c}\right)\right)\mathrm{d}c \approx -\Gamma \frac{\partial^2 \mathrm{g}}{\partial c^2}\mathrm{d}c. \tag{26}$$

With $\Delta\mu = \mu_2 - \mu_1$ being the chemical potential difference between both components, ε the lattice expansion and τ_{ii} the two in-plane GB tensions. Note that the integral of $\Delta\mu$ is the Gibbs free energy g. Eq. (26) shows that the Gibbs adsorption isotherm contains a term, representing the necessary elastic work against the GB tension τ, caused upon expansion through alloying.

For quantitative analysis, the specific excess Γ is calculated according to Cahn [27] by the total solute excess $[N_2]$, representing the additional amount of component 2 atoms in the GB area, in comparison to a homogeneous bulk, relative to the GB area [42]:

$$\Gamma = \frac{[N_2]}{A}. \tag{27}$$

2.3.5.2 McLean isotherm

Alternatively, GB segregation was described by Langmuir and McLean in terms of local concentration of the segregating element [43, 44, 45]. Langmuir first defined the GB layer to have a fix number of adsorbing sites, namely the sites of a complete monolayer of atoms. Using this assumption, McLean calculated the total free energy, F_{GB} of the system considering the distribution of solute atoms *P* and *p* among lattice planes, *N*, and "distorted", GB sites, *n*:

$$F_{GB} = pe + Pe_L - k_B T[\ln n!\,N! - \ln(n-p)!\,p!\,(N-P)!\,P!] \tag{28}$$

With e and e_L as the free energies of the solute atoms in the GB and lattice. The last term on the RHS is the configurational entropy of the solute atom arrangement in the GB and lattice. Assuming, that the most probable atomic arrangement is the one in the equilibrium state (when the total free energy is minimized), and by assuming ideal solution behavior, the formulation of the Langmuir-McLean segregation isotherm, describing the concentration of the GB monolayer in terms of the bulk concentration is given:

$$c_{\mathrm{GB}} = \frac{c_{\mathrm{Bulk}} \exp\left(-\frac{Q}{k_{\mathrm{B}}T}\right)}{1 - c_{\mathrm{Bulk}} + c_{\mathrm{Bulk}} \exp\left(-\frac{Q}{k_{\mathrm{B}}T}\right)}\,. \tag{29}$$

with k_{B} as the Boltzmann constant. *Q* is a constant segregation parameter and can be determined e.g., by fitting, when c_{GB} and c_{Bulk} are measured.

Further research showed that GB segregation is not limited on just one monolayer, but several atomic layers around the GB are involved. Additionally, the assumption of an ideal solution is not valid for every binary solution. Therefore, several extensions of this model were formulated to improve these deficits. They are summarized, e.g. in [2]. An extension, proposed in [9, 44] not only considers the mentioned drawbacks, but also the applicability of the formalism to experimental data. Eq. (29) contains the GB concentration which is probably determined as a peak maximum from a composition profile across the GB. However, this value has a dependence on the profiles' binning size and the spatial resolution of the analysis, meaning it is not unambiguous. Therefore, instead the GB concentration, the solute excess *Γ* should be used for thermodynamic calculations [42]. Hence, a model function results, being similar to the Langmuir-McLean isotherm:

$$\Gamma(c_{\mathrm{Bulk}}) = \rho \cdot w_{\mathrm{eff}}(c_{\mathrm{eff}} - c_{\mathrm{Bulk}}) = \rho \cdot w_{\mathrm{eff}}\left(\frac{c_{\mathrm{Bulk}} \exp\left(-\frac{Q_{\mathrm{eff}}(c_{\mathrm{Bulk}})}{k_{\mathrm{B}}T}\right)}{1 - c_{\mathrm{Bulk}} + c_{\mathrm{Bulk}} \exp\left(-\frac{Q_{\mathrm{eff}}(c_{\mathrm{Bulk}})}{k_{\mathrm{B}}T}\right)} - c_{\mathrm{Bulk}}\right), \qquad (30)$$

with w_{eff} as the effective width of the GB layer, c_{eff} as the effective concentration, in analogy to c_{GB} in the Langmuir-McLean isotherm, ρ as the atomic density and Q_{eff} as the composition-dependent effective segregation parameter.

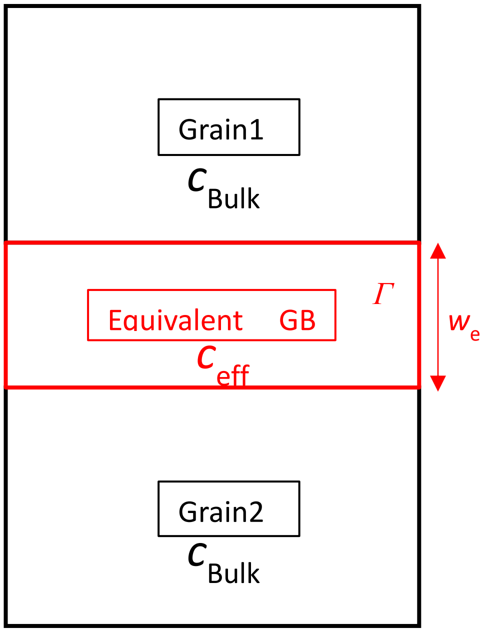

Figure 12: Scheme of the equivalent hypothetical GB layer in-between two grains.

In this model, the GB monolayer was replaced by an equivalent hypothetical layer with just one kind of lattice sites (in relation to McLean) that have, by definition, the same segregation behavior as the real physical GB (Figure 12). Since this hypothetical layer considers only one kind of lattice sites, it also displays just an average segregation behavior. However, this helps simplifying the mathematical description and still reflecting the segregation of the complete physical GB. Note that in Eq. (30), w_{eff} and Q_{eff} are describing the hypothetical system and have therefore no direct physical meaning. Though this formulation can be fitted to experimental data to model Γ and to calculate $\mathrm{d}\gamma$ by using Eq. (26).

2.3.6 GB segregation according to an extension of the Butler equation

Beside the McLean isotherm, the GB segregation can be described by a modulation of the Butler equation as described in [46]. Herein, the GB energy is expressed as a function of the bulk concentration, temperature, pressure, and GB orientation. Assuming an infinite source of the segregating compound, formalisms for partial GB energies of all alloy components were defined. With the knowledge of some physical parameters of the pure components (which can also be estimated by known methods), the GB energy and segregation can be evaluated as a function of the bulk composition. Assuming ideal solution behavior and equal atomic sizes of all components, the GB composition of a binary alloy can be expressed as:

$$c_{\mathrm{GB}} = \frac{c_{\mathrm{Bulk}} \exp\left(\frac{\omega(\sigma_A - \sigma_B)}{k_{\mathrm{B}}T}\right)}{1 - c_{\mathrm{Bulk}} + c_{\mathrm{Bulk}} \exp\left(\frac{\omega(\sigma_A - \sigma_B)}{k_{\mathrm{B}}T}\right)} . \qquad (31)$$

With ω as the molar interfacial GB area and σ_A, σ_B as the partial GB energies of the both components. Note that Eq.(31) is equal to Eq.(29) when $-Q = \omega(\sigma_A - \sigma_B)$. In [46], this calculation was made for the CuNi system at a temperature of 1200K. Figure 13 shows these plots for the GB mole fraction (a) and GB energy (b) as a straight line. The dashed line represents the case, if no GB segregation would take place (when the GB energy is the same for both components). With increasing bulk concentration of Cu, the Cu mole fraction in the GB increases, too. However, the increase (slope) shows a deviation from linearity, which is strongest around 0.2. This result is in accordance with the findings in [9] shown in Figure 1, where the segregation of Cu reaches its maximum at the same bulk concentration for all tested temperatures. The GB energy is with 0.75 $\mathrm{Jm^{-2}}$ highest for pure Ni and is reduced with increasing Cu content to be around 0.56$\mathrm{Jm^{-2}}$.

Comparing this to the calculated GB energy at 1000K in [9], the trend is similar, however, the quantitative values show discrepancies with the maximum at 1.1 and minimum around 0.7 $\mathrm{Jm^{-2}}$. These discrepancies probably stem from the different GB orientation and temperature used for both researches. Additionally, different data for the phase boundaries of the miscibility gap were used, leading to different Gibbs energies. For the calculations in [46], the magnetic parameters, the GB energies of the pure components and the molar GB areas are necessary, which were either taken from different references or estimated by other physical considerations. Instead, for the calculations in [9], an interatomic potential in necessary.

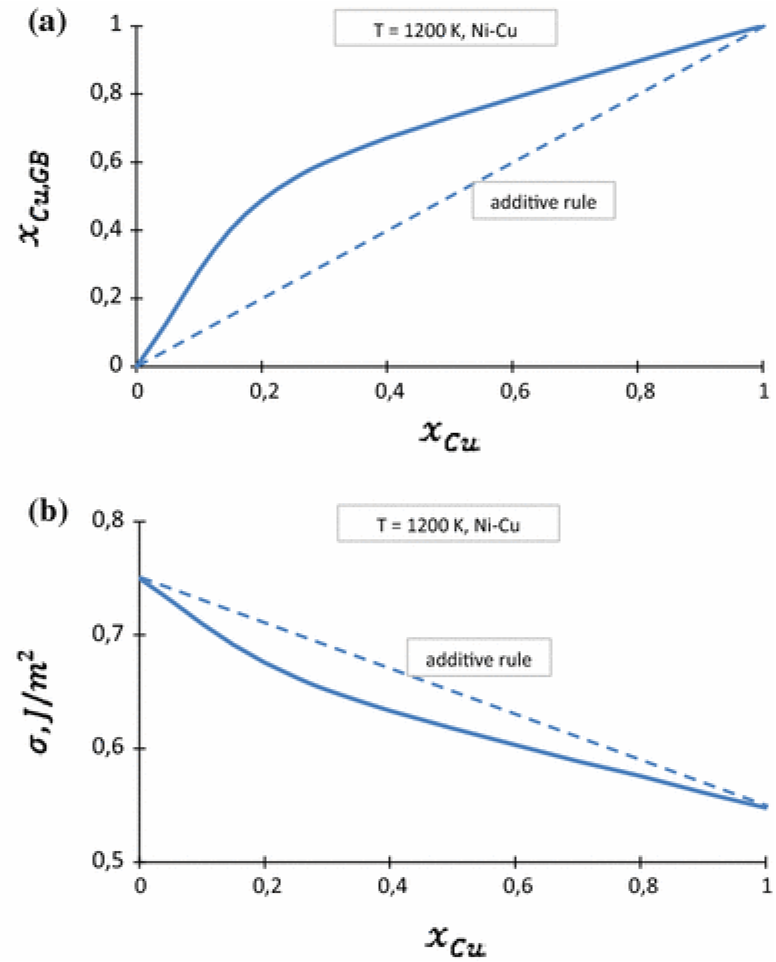

Figure 13: GB composition (a) and GB energy (b) as a function of the bulk Cu composition. The dashed lines represent the case for no GB segregation, when the GB energies of both materials are equal. [46]

2.3.7 GB segregation kinetics

If the annealing time is not sufficient, equilibrium segregation is not reached, and the segregation kinetics become important. Therefore, McLean presented a model [47], assuming volume diffusion of the solute atoms from the adjacent grains, which were described as two infinite half crystals with constant solute constant. The diffusion process itself is described by the Ficks laws and is expressed as:

$$\frac{X_\mathrm{b}(t)-X_\mathrm{b}(0)}{X_\mathrm{b}(\infty)-X_\mathrm{b}(0)} = 1 - \exp\frac{4Dt}{\beta^2 f^2}\,\mathrm{erfc}\sqrt{\left(\frac{4Dt}{\beta^2 f^2}\right)}\,. \tag{32}$$

With $X_\mathrm{b}(t)$ as the GB content at time t, D the Diffusion coefficient in the bulk. f is defined as $f = \frac{a^3}{b^2}$ and gives a relation for the atomic sizes of the solute, a, and matrix, b, and β is defined as $\beta = \frac{c(x)_{GB}}{c(x)_{bulk}}$, which is the ratio of the solute atoms in the GB and in the adjacent atom layer of the bulk. The model further assumes that β is constant, which is only true for dilute systems with low segregation amounts. Generally, β decreases with the segregation process since the GB becomes saturated [48]. This case was investigated by Rowlands and Woodruff [49]. By considering several saturation levels from no saturation (McLean behavior) to full saturation, the following graphs were calculated:

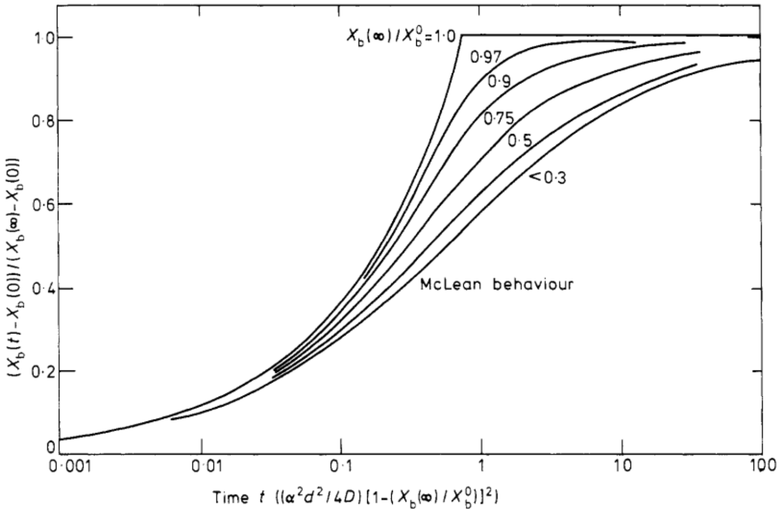

Figure 14: GB segregation kinetics. the normalize GB segregation concentration as a function of the time for several saturation levels according to Rowlands and Woodruff [48]

2.4 The CuNi system

Copper is the first element in the first side group (11th elemental group) in the periodic table of the elements (PTE) and stands in the 4th period. It is the only metal having a reddish color, which stems from the electronic transition between the fully occupied 3d-orbitals and the half-filled 4s orbital. It has a face-centered crystal structure with a density of 8.92 gcm^{-3} and therefore belongs to the heavy metals. It has a high electric and thermal conductivity, which is the highest after silver and due to its high ductility it's easy to process mechanically. Thus, the main application for Cu is in the electrical industry. Moreover, Cu has a high corrosion resistance, which makes it an attractive material for seawater applications [50, 51].

Table 1: Physical properties of Cu and Ni [52]

	Cu	**Ni**
Atomic number	29	28
Elemental group (IUPAC)	11	10
Crystal structure	fcc	fcc
Melting temperature T_m / K	1358	1728
Molar mass M / g mol^{-1}	63.456	58.893
Isotopes	^{63}Cu (69.2%) ^{65}Cu (30.8%)	^{58}Ni (68.1%) ^{60}Ni (26.2%) ^{62}Ni (3.63%) ^{64}Ni (0.93%)
Density ρ / g cm^{-3}	8.92	8.91
Atomic density ρ_N / nm^{-3}	84.9	91.4
Atomic radius r / pm	149	145
Cohesive energy E_{coh} / eV	3.49	4.44
Surface energy E_S / Jm^{-1}	1.79	2.38
Evaporation field E_{evap} /V nm^{-1}	30	35
Lattice parameter a / nm	0.3597	0.3499
Electric conductivity AV^{-1}m^{-1}	$58.1 \cdot 10^6$	$13.9 \cdot 10^6$
Thermal conductivity Wm^{-1}K^{-1}	400	91

Ni is the first element of the 8th side group (10th elemental group according to IUPAC) in the PTE and stands in the 4th period. It's the left neighbor of Cu and has therefore similar physical properties, like the density of 8.91 gcm^{-3}, the fcc crystal structure, the atomic radius and the lattice parameter (see Table 1). In comparison of these two metals, a great difference is seen for their surface energies, with the one for Ni being larger. This correlates with the melting temperatures of both metals and thus, their cohesive energies.

Since Ni is a good processable material, it's used for the coin fabrication. Other than Cu, Ni has a low electric and thermal conductivity, and is ferromagnetic with a Curie temperature of 354°C, and therefore interesting in magnetic applications. Because of its high chemical stability and corrosion resistance, it is a good material for laboratory equipment or as coating for metallic components (especially iron). The main application of Ni, however, is its use as alloying component in the metal industry. By alloying steel with Ni, the corrosion resistance is increased, and the ductility is improved [50, 51, 53]. Other alloys with industrial importance are the CuNi alloys. This alloy is one of the oldest known in civilization and was used already in the 3rd century in China for the arm and coin production, due to its high mechanical stability and good deformability. After its reproduction in Europe, in the 18th century, effort was taken to investigate and improve the alloy by changing the alloy composition. By this, different CuNi alloys with different properties arise, which opened new application areas like in sea water, marine hardware [54].

With the increasing understanding in material science, further development was gained by considering the microstructure of the alloys. So, by reducing the layer thickness, the resistivity and thermal sensitivity could be increased, as shown by Yang et. al [55]. This opens new application fields in the high-end technologies, like in micro-electrical devices as resistors or as thermocouples in thermo-electric applications [56].

3 Experimental procedures

In this project, two tasks were accomplished, namely the determination of the miscibility gap, meaning localization of the phase boundary with the critical temperature T_C, and the characterization of grain boundary segregation. For both, APT experiments were carried out, though with different sample geometries. Starting from the preparation of the sample substrates, the particular steps for sample preparation and the physical principles of the lab equipment will be presented in the following chapter.

3.1 Electropolishing

For the APT measurements, needle-shaped samples of around 100 nm curvature radius are necessary. For their production, first, needle posts were generated serving as sample substrates which were then coated by the material of interest. As a substrate material, tungsten was chosen due to its high hardness and conductivity. Additionally, the evaporation field of W is so high, that an ordered evaporation during APT analysis is ensured.

The preparation of W-post is done by electropolishing. Herein, an electrochemical cell is built, using a W-wire as anode (positively charged electrode). By oxidizing the wire surface, the material is slowly removed, and the wire becomes thinner. This set-up is shown schematically in Figure 15. Together with a graphite rod, serving as the counter electrode, the W-wire is inserted into a cuvette, filled with an electrolyte solution. A voltage power supply was connected on both electrodes, so that an electrical circuit is produced. Using short AC pulses, the wire surface is oxidized slightly below the electrolyte/air interface and water soluble tungstate WO_4^{2-} is formed with each pulse [57] [58]. The tungstate is continuously removed by the surrounding aqueous solution and the wire surface is always metallic W, which oxidates again. So, after some pulses, a narrowing at the wire is observed (necking), where it finally brakes. The prepared tip can be shortened and broadened by some additional pulses for more stability and a larger coating surface. At the end, the reaction impurities were removed by dipping the tip in a 50%- ethanol solution. The electropolishing of the tip was observed through a light microscope with 50 times magnification, mounted in front of the cuvette.

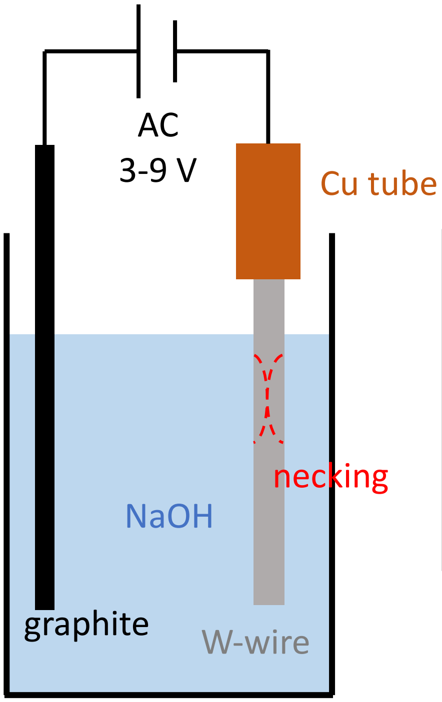

Reaction:

Cathode: $6\ H_2O + 6\ e^- \rightarrow 3\ H_2 + 6\ OH^-$

Anode: $W + 8\ OH^- \rightarrow WO_4^{2-} + 4\ H_2O + 6\ e^-$

Total: $W + 2\ OH^- + 2\ H_2O \rightarrow WO_4^{2-} + 3\ H_2$

Figure 15: Schematical drawing of the electropolishing equipment with a graphite cathode, the W wire as anode and NaOH as electrolyte solution.

3.2 Sample coating

The substrates were coated with CuNi thin films using Ion beam sputtering (IBS). For that, a custom-built IBS system was used, consisting of a UHV chamber with a residual gas pressure of $1 \cdot 10^{-8}$ mbar. It's equipped with an ion gun from Veeco Inc, model 3FC. This gun creates electrons from a tungsten cathode filament, working as an emitter. These electrons collide with Ar-atoms, stemming from a pipeline, connected directly to the gun, and produce positively charged gas atoms. At the gun outlet, a grid system samples the gas ions at the inner grid, whereas an outer grid accelerates the ions away, forming a directed beam. Outside the gun, another W filament provides electrons to neutralize the beam plasma.

In front of the ion gun, sputtering targets (plates of metal or alloy) to be deposited were placed on a rotating holder. These targets were irradiated by the plasma beam to eject target atoms and deposit them on the substrate, being placed close to the targets, also on a rotating holder. The deposition thickness is controlled via a quartz crystal thickness monitor with the quartz being parallelly arranged beside the substrate, to guarantee that substrate and quartz are exposed with the similar material thickness (see Figure 16) [59].

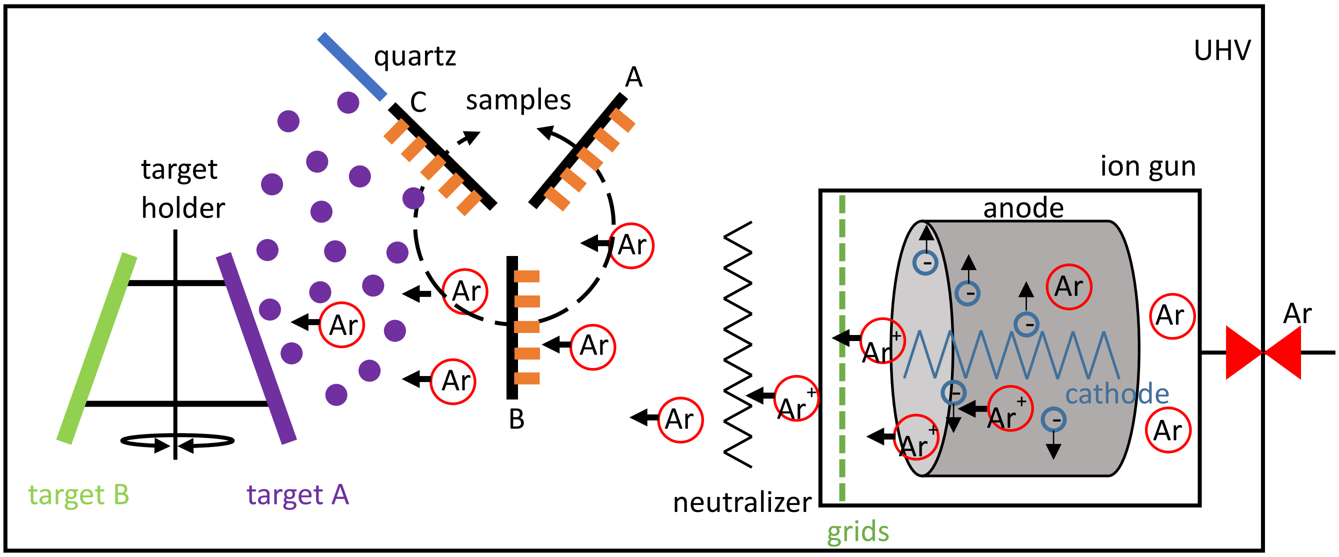

Figure 16: Schematic drawing of the IBS chamber

3.2.1 Analysis of the miscibility gap

For the analysis of the miscibility gap, multi-layered CuNi thin films were prepared. The layers consist of pure Cu with 3 nm thickness, and Ni-rich CuNi layers of 70 at.% Ni with 8nm, so that the overall concentration is 50 at.%. In total, 10 or 20 alternating layers were sputtered on a post. At the top, a pure Ni cap of 30 nm thickness was sputtered to protect the multilayers from oxidation during annealing. After annealing, an additional layer of 300nm Cr was sputtered as protection during tip sharpening (see Figure 17a).

Since the layer thicknesses were so small, a calibration of the thickness monitor was made first by sputtering single layers of pure Cu and pure Ni with 25 nm thickness, and an additional multilayer of ten CuNi bilayers with 10 nm thickness on a plane SiO_2 substrate. From these samples, TEM lamellae were prepared using the FIB lift-out technique. As protection during FIB milling, a cap layer of 500nm Cr was deposited, too.

3.2.2 GB analysis

For the grain boundary analysis, CuNi alloys with varying Cu concentration were prepared. Therefore, CuNi alloys with predefined concentrations were sputter-deposited directly on W posts with a thickness of 600 nm from alloyed sputtering targets (see Figure 17b).

To ensure observing grain boundaries, the grain sizes must be lower than 200nm, since this corresponds to the final tip diameter. This was confirmed by sputtering with the same conditions on SiO_2 as for W posts and by analyzing the grain size distribution using Electron Backscatter Diffraction (EBSD).

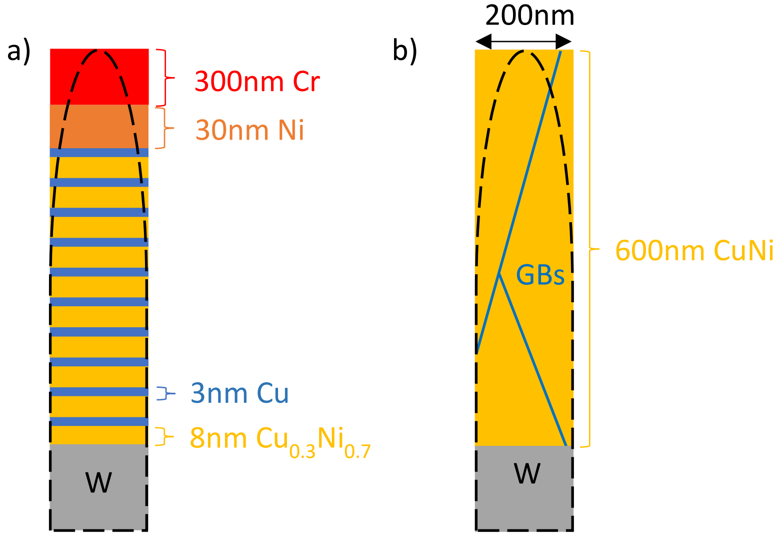

Figure 17: Different sample coatings used in this project, where a) are multilayered samples for miscibility gap analysis and b) alloy samples for grain boundary analysis.

3.3 Annealing

The samples were annealed in a UHV quartz tube oven with a residual gas pressure below $3 \cdot 10^{-7}$ mbar (Figure 18). It has a thermocouple welded on the tube opening which can be connected to the substrate holder. With this, the temperature at the samples can be observed directly.

Before usage, the quartz tube was baked out at 1073 K to make sure that no impurities will affect the annealing treatment. Then, the samples were inserted, and the tube was pumped overnight. The desired temperature was arranged at the tube-oven, which was then slid over the quartz tube after constant temperature was established.

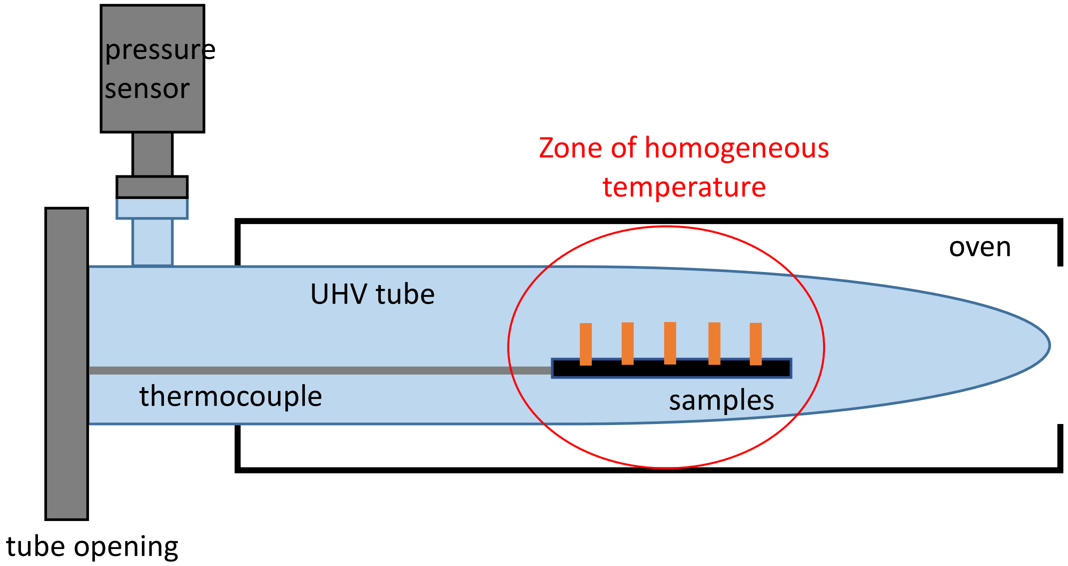

Figure 18: Schematic drawing of the UHV tube oven

3.4 Sample preparation

The needle-shaped posts for APT analysis were produced out of tungsten using the electropolishing procedure as described in section 3.1. For that, a 2.5 cm piece was cut from a W-wire (99.95 % purity) with 75 µm diameter. For easier handling, it was climbed in a Cu-tube of 1 cm length and 0.2 cm outer diameter. Using a graphite rod from a pencil as counter electrode, and a 1 molar NaOH solution as electrolyte, the wire was thinned with short pulses of 9 V (rough thinning) and 3 V (fine thinning). Then, the needle was cleaned from electropolishing residues by washing with a 50%- ethanol/water solution.

After electropolishing, the tips were flattened to posts. For that, a focused ion beam (FIB) with an integrated scanning electron microscope (SEM), here, the Scios Dual Beam from FEI was used. This instrument is equipped with a Ga^{2+} source and mills precisely through samples in a micrometer scale leaving a smooth surface behind. By aligning the tip axis being perpendicular to the ion gun and milling the apex with a rectangular pattern along the tip, planar surfaces of 2-3 µm diameter were prepared (Figure 19). For this, beam currents of 3 nA for cutting, and 300 pA for fine polishing were used at an accelerating voltage of 30kV. This preparation technique was adopted from Stender et. al [59].

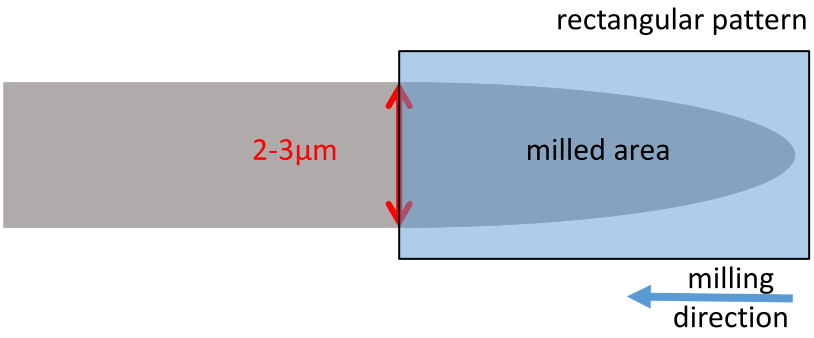

Figure 19: FIB milling of the substrate to form a planar and smooth surface.

In the next step, the W posts were coated with CuNi thin films via IBS. Therefore, the posts were placed on a substrate holder and inserted, together with the desired targets in the UHV chamber (position A in Figure 16). To achieve a low pressure, the chamber was pumped overnight. Before coating, the targets were cleaned for 15 to 20 minutes and the posts for 1 minute (position B in Figure 16) by direct irradiation with the ion gun. The used beam voltages and currents were 400V and 10mA for post cleaning, and 600V and 20mA for target cleaning and final sputtering.

Table 2: Annealing times and temperatures for the multilayered samples. 623 has different starting concentrations with $c_1 = 0.44$ and $c_2 = 0.7$.*

T / K	t / d					
673	1	2.5	4.5	7	11	14
623	7	14				
623*	7	16	30	44	60	
573	88	214	458			

The coating is performed according to Figure 16 with the substrate holder being at position C. Afterwards, the samples were annealed according to section 3.3. For the analysis of the miscibility gap, the annealing temperatures were 573 K, 623 K and 673 K for varying annealing times (see Table 2), whereas the alloy samples for the segregation experiments were all annealed at 700 K for 24 h.

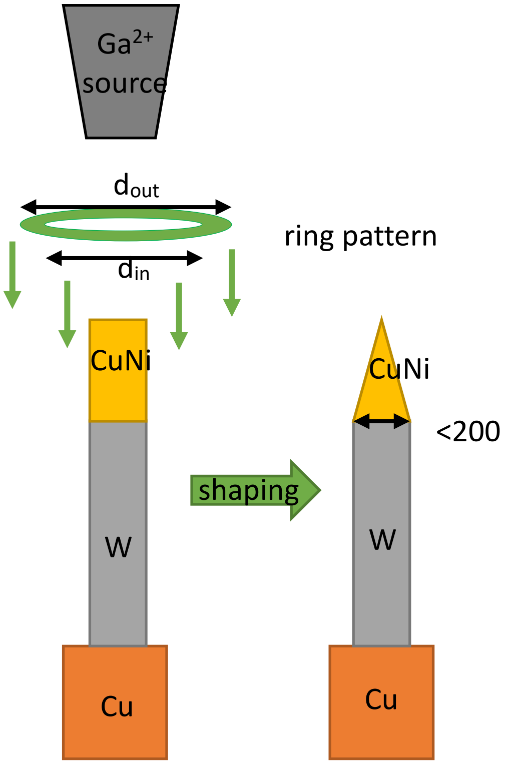

Figure 20: Schematic drawing of the FIB milling procedure

Finally, the samples were sharpened to nanometer-sized tips, using the FIB. This time, the samples were aligned parallel to the Ga^{2+} source and ring-shaped exposure patterns were used for milling [59]. Starting with a pattern of 2µm outer and 1µm inner diameter, the diameters were stepwise reduced to 300nm and 100nm (Figure 20). The progress of milling was observed via SEM snapshots and the radius of the tip was controlled. When the radius reached the arranged inner ring diameter, the milling was stopped and the diameter was reduced. With that, the sample was formed to a cone with an apex diameter of <200nm. For milling, a starting current of 0.3 nA was used, which was reduced stepwise to 50 pA for the smallest pattern at a voltage of 30 kV.

3.5 Electron backscatter diffraction (EBSD)

Using the electron beam during the FIB process, crystallographic information of the samples can be received. This method is called EBSD and utilizes diffraction of the electron beam on the sample lattice planes in reflection geometry. Principally, the incident electron beam will be scattered randomly when entering the sample. Due to the diffuse character of the beam, some electrons will also be scattered elastically from the sample lattice planes, fulfilling the Bragg condition (Figure 21) and forming an intensive reflected beam by positive interference. Considering all possible source beam directions that can be reflected within the Bragg angle θ, all diffracted beams together form a cone with the vertex being the point of impact on the lattice plane and the angle being 180° - 2θ (Figure 22). The double cone in Figure 22 is due to irradiation of the same lattice plane from both sites since every beam source is reflected on both neighbored lattice planes. From these so-called Kossel cones, the Kikuchi lines are formed, being the lines in the diffraction pattern, by section of the Kossel cone surface with the image plane of the detector.

For each lattice plane, two parallel lines are visible with an angular distance of 2θ, which is proportional to the interplanar spacing d according to the Bragg law (Eq.33), where λ is the beam wavelength. The intensities of these lines, however, are different. This is due to the inclination angle of the lattice planes with the incident beam. The reflected beam from the higher angle of divergence ($\theta+\varepsilon$ in Figure 21) will have higher intensity and therefore called excess line. Conversely, the low-angle beam will have low intensity and is the defect line. In the defect line, the Bragg reflections cause more electrons to be reflected away and so they cannot contribute to the intensity. For the excess line, the inelastically scattering has a high contribution and the background intensity is increased.

$$\lambda = 2dsin\theta \approx 2d\theta \rightarrow 2\theta \propto d^{-1} \qquad (33)$$

The Kikuchi line pairs or bands, with their specific line widths are unique for each crystallographic plane. When all crystallographic planes of the sample form Kikuchi lines, a Kikuchi pattern is created, and the image will consist of several bands with a certain angular relationship to each other. Thus, crystallographic information can be extracted from this [32] [60].

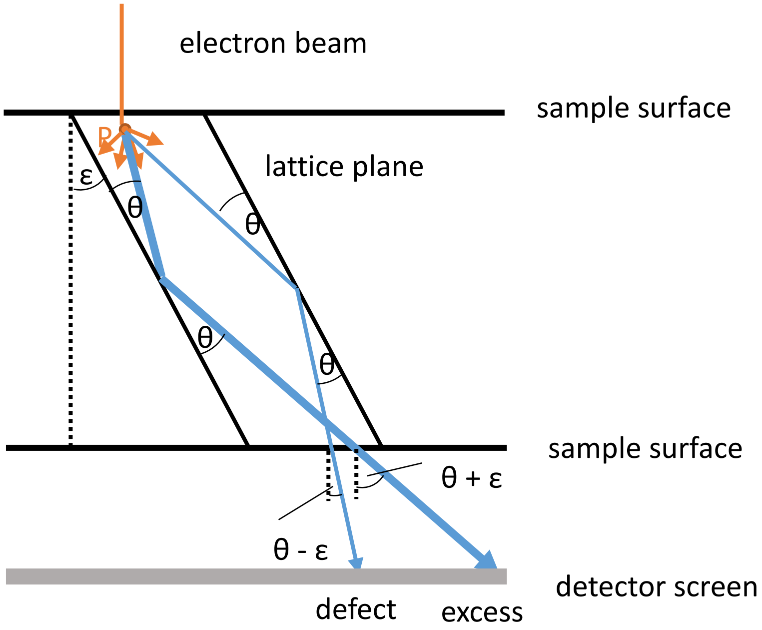

Figure 21: Creation of Kukichi lines. The electron beam (orange) enters the crystal and is inelastically scattered at point P. Some of the diffusely scattered beams hit the sample lattice planes in Bragg condition (angle ϑ) and get elastically scattered (blue) on a detector screen. Since the beam is scattered on both adjacent lattice planes, two Kikuchi lines are formed which differ in intensity according to the inclination angle ε of the lattice planes to the beam origin. The beam with the lower angle of divergence has a higher intensity (thick blue line)

To define the crystallographic orientation, the Kikuchi patterns must be indexed first. With the used software, TEAMS, this is done fully automatically by transforming the lines into points in the

Hough space for easier indexing. Then, the sample axes are needed to determine the crystal orientation in dependence to a reference frame. By giving the tilt angle of the tip axis normal to the detector, TEAMS can create a coordinate system and calculates the absolute orientation. The result is an orientation matrix, from which several orientation representations can be determined. [32]

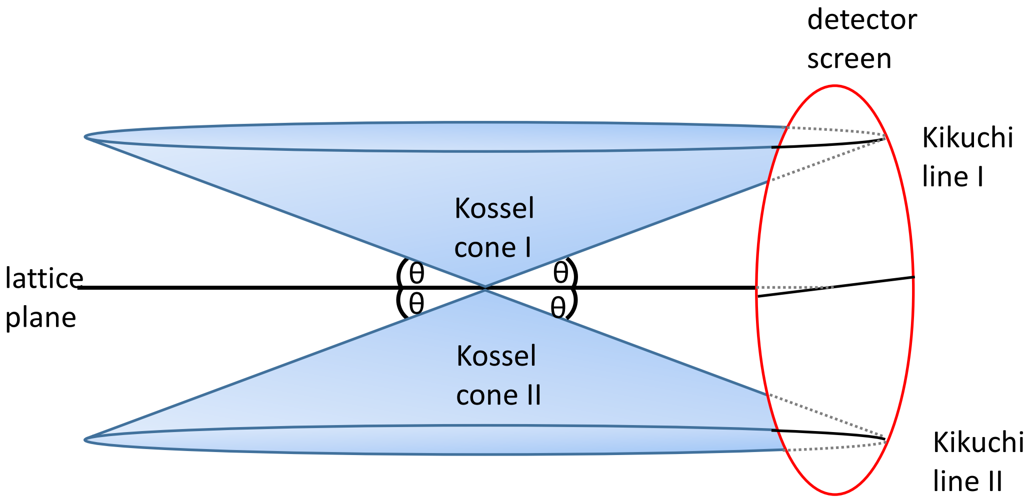

Figure 22: Formation of Kikuchi lines (black lines on screen) from Kossel cones (blue cones) on the detector (red circle) [61]

3.5.1 EBSD in transmission geometry (tEBSD)

In comparison to conventional EBSD, the tEBSD detects transmitted electrons instead of the backscattered. So, the sample tilt relative to the electron beam is different for both techniques (Figure 23). A usual tilt of 70° towards the sample surface normal is used for EBSD, with the detector being at 90°. In case of tEBSD, the tilt lies between 40 and 50°. A second difference is the sample thickness. For tEBSD, the samples must be electron transparent which means that the thickness should be under 100nm, whereas for EBSD, micrometer-sized samples are more suitable. Generally, the tEBSD provides a higher resolution which stems from the smaller interaction volume. While standard EBSD has a special resolution of 20-50 nm, a spatial resolution of 5-10 nm can be achieved for tEBSD. This makes is very convenient for crystallographic analysis of APT samples, especially because it can be directly included to the sample preparation step. [62]

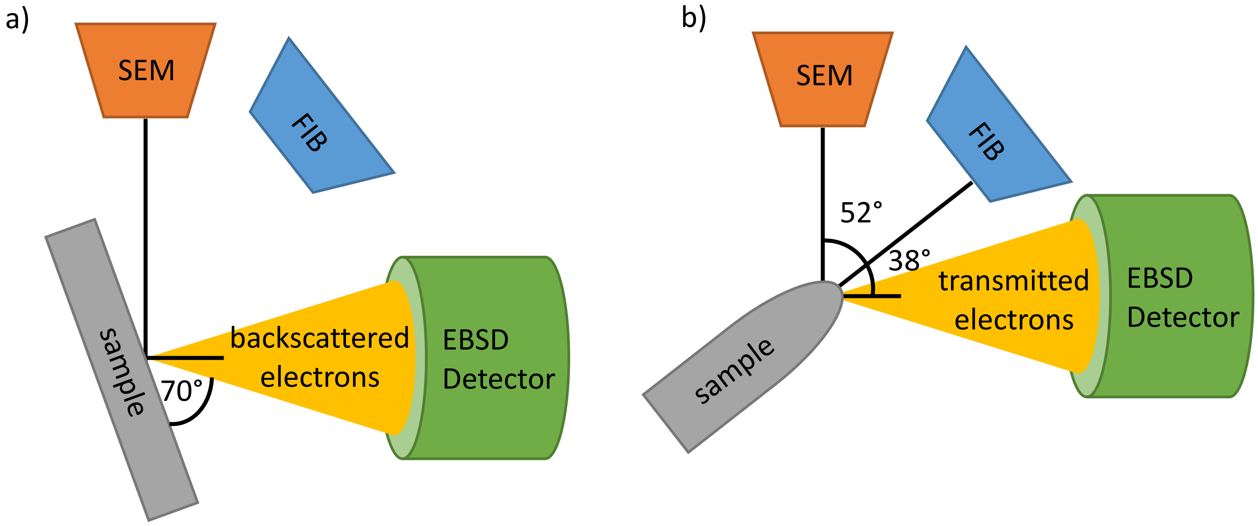

Figure 23: Difference of the experimental setup of EBSD (a) and tEBSD (b)

Measurement parameters:

To analyze the grain orientations inside a tip, an orientation map was measured after the final FIB milling. For that, the EBSD detector, EDAX, was inserted and the electron beam was adjusted to an acceleration voltage of 30kV and a current of 1.6nA. The correct tilt of 38° (which is the tilt to the detector) had to be entered in the TEAM V4.5 software to ensure correct orientation calculations and the tEBSD mode had to be selected. A 5x5 binning was used in camera settings and an exposure time between 0.1 and 100ms was arranged. To improve the image quality, intensity histogram normalization and dynamic backscatter subtraction were used in image processing. For the Hough transformation, a medium mask was used with a binned pattern size of 120° and a θ-step size of 0.5°.

The grain orientation was determined from four sides of the tip, each with a 90°-rotation around the tip axis to easily recover the grains in both, the EBSD map and the APT reconstruction. After tEBSD, the tip surface was cleaned from analysis residues by a final FIB milling with 48pA at 5kV for 5s.

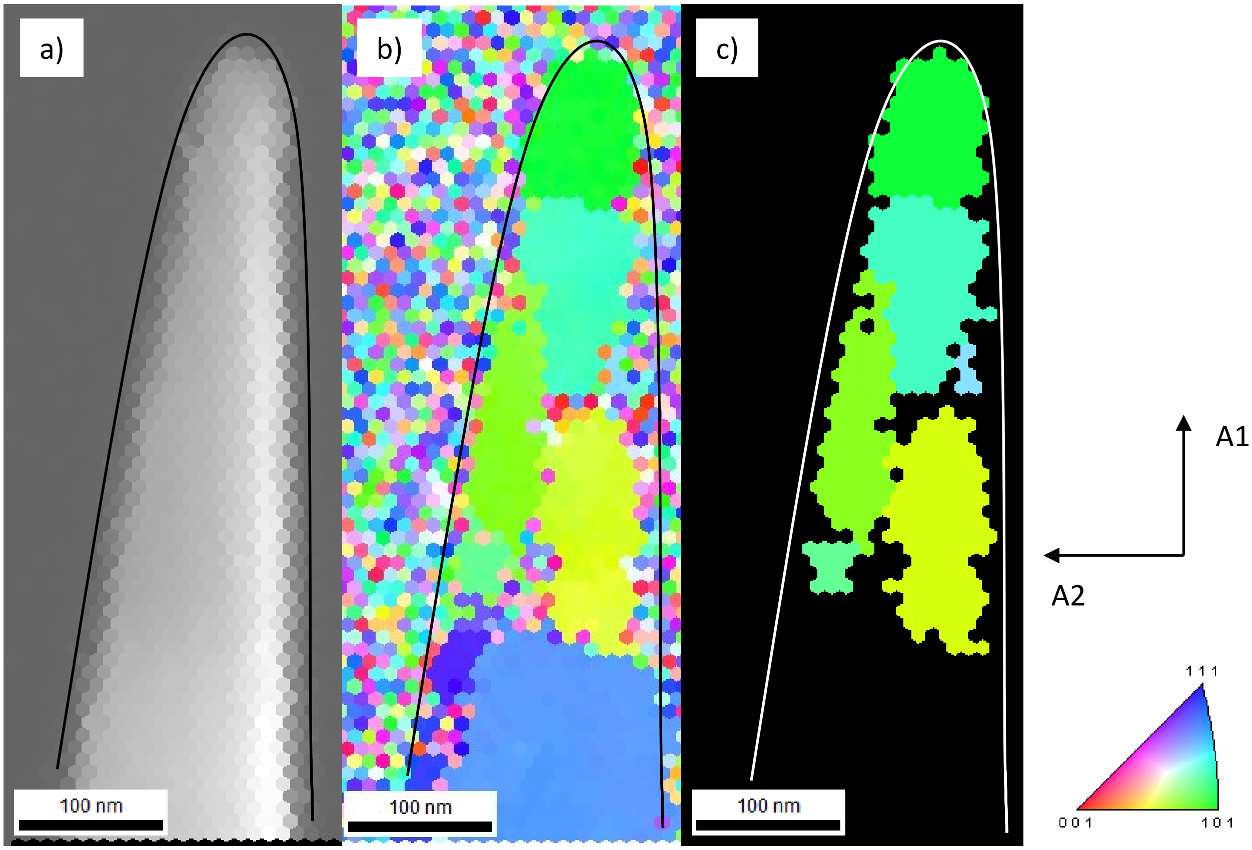

Figure 24: Grain orientation analysis with TSL OIM analysis 8 software. a) shows the SEM secondary electron image of the tip, b) the IPF map without cleaning and c) the final, cleaned data, showing just FCC measurements and filtering out signals lower than CI<0.1.

The measurements were evaluated using TSL *OIM analysis v8* software. The raw data were first cleaned up by averaging the grain orientations of each bin to a single orientation within a tolerance angle of 5°. Then, the confidence index (CI) was set to higher than 0.1. An inverse pole figure (IPF) map was created from this data, which colors grains of different orientation (Figure 24). From each grain, the orientation matrix is received. The misorientation axis and angle between adjacent grains can also be determined here.

3.5.2 Orientation determination by tEBSD

The orientation is determined from the Kikuchi patterns, which have specific Kikuchi lines and angular relations for each orientation. To construct an orientation map, the sample coordinate system is taken as a reference system. Then, any sample direction (normally the sample normal, A3) can be expressed by the crystal coordinate system. This is the so-called inverse pole figure (IPF-) map and the typical way to present orientation data. With the IPF-map, the grain orientation, and the orientation relation between the grains to each other, the misorientation is determined. The misorientation expresses basically the rotation necessary to bring a grain in coincidence with another and is displayed either as a rotation matrix or as an angle/axis pair.

The orientation determination is a fully automated step, including the measurement of the Kikuchi pattern, its indexing and setting into relation with the external (specimen) reference system. Starting with the measurement, overlapping crystallographic information, or just limited camera resolution can lead to wrong indexing and with that, to distorted orientations. To overcome this uncertainty, several strategies are given to control the quality of indexing. Therefore, the tEBSD data was further analyzed by the program *TSL OIM Analysis v8.* Several parameters exist, which helps quantify the quality of the orientation determination. One parameter is the image quality (IQ) and stands for the quality of the diffraction pattern. It is best for a perfect single crystal, and it is reduced for overlaying crystal lattices or by distortions of the crystal (for example from grain boundaries). Unsuitable volume ratio of the overlapping grains can cause wrong indexing. The fitting of the indexing with an orientation is measured over the confidence index (CI). This value ranges from 0 to 1 and indicates how likely the chosen indexing fits, in comparison to all other possibilities. Therefore, the Kikuchi lines of the pattern were arranged in all possible band triplets (combining three Kikuchi lines together) and their angular relation to each other was determined. The results were compared with a look-up table, that contains the indexing of all grain orientation relations. For a single triplet, it can happen that more than one orientation is possible. However, considering all triplets, the orientation, with the highest number of fitting triplets is determined as the pattern orientation. The CI, describes the most probable orientation O_1 subtracted by the second probable O_2, out of all possible orientations O_{total}:

$$CI = \frac{O_1 - O_2}{O_{total}}, \qquad (46).$$

where the orientation is expressed as a rotation matrix. A way for testing the quality of the determined and the measured orientation is to calculate the band for a certain orientation and to compare it with the Kikuchi pattern of the experiment. With this ‘fit’ parameter, the deviation can be quantified.

In this project, the correctness of the orientation determination was ensured by considering the orientation information of just fcc-crystals. Furthermore, the point orientations in each grain were averaged using a tolerance angle of 5°. Additionally, all mapped points with CI < 0.1 were deleted.

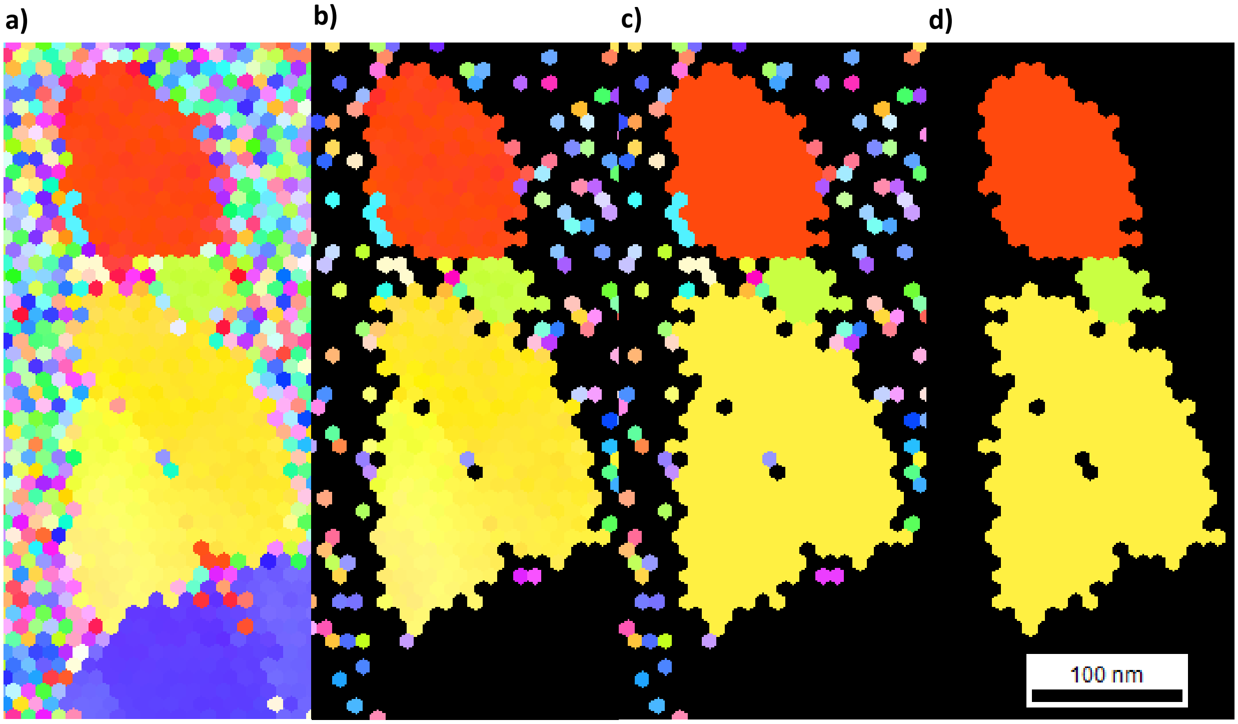

Original IPF map **Just FCC crystals** **Averaging grains** **CI > 0.1**

Figure 25: Clean-up procedure of the IPF maps: a) shows an as-measured IPF map. In b), the orientation of fcc crystals is extracted (W not included anymore since it is a bcc). In c), an averaging of the points with ±5° deviation is made, and n d) just points with a CI of more than 0.1 are shown.

3.6 Atom Probe Tomography (APT)

Finally, the samples were measured using a custom-built, laser-assisted atom probe tomograph [63]. Atom probe tomography is based on field-induced ionization of sample atoms which were then accelerated towards a position-sensitive detector. Meanwhile, their flight time is measured for chemical identification.

For ionization of a sample atom, a huge electric field strength is necessary. Therefore, the samples were prepared as nanometer-sized needles with an apex hemisphere radius (of curvature) R of <200 nm. By applying a high positive voltage V to such a tip, the electric field acting on the surface atoms is given by:

$$F = \frac{V}{k_f R}, \tag{34}$$

which is basically the field at the surface of a sphere with a contribution of a shank, considered by the field factor k_f, stemming from the cone structure of the needle. According to Eq. (34), the field strength will increase as the apex radius decreases. This explains the necessity of small R.

To evaporate atoms single by single, a pulsing mode is applied in addition to a high base voltage so that just the most prominent atoms at the very outer surface (these are affected most from the field force) have enough energy to ionize. The pulsing is realized either by applying high voltage (HV-pulsing) or by applying laser beam (laser-pulsing). The latter allows to measure also non-conductive or brittle materials. Due to a potential difference, the ionized atoms leave the sample surface toward the detector. The micro electrode in front of the detector shields from ion impacts at the outer positions. Since these atoms have huge trajectory aberrations that cannot be corrected, this improves the mass resolution.

After the removal of the prominent atoms, their neighbor atoms will be protruding and are evaporating next, until the whole atomic plane is evaporated. Then, the next layer starts evaporating. To avoid trajectory distortions by thermal vibration, and gas impurities, the experimental set-up is placed in a UHV chamber and cooled to cryogenic temperatures (see Figure 26) [64] [65].

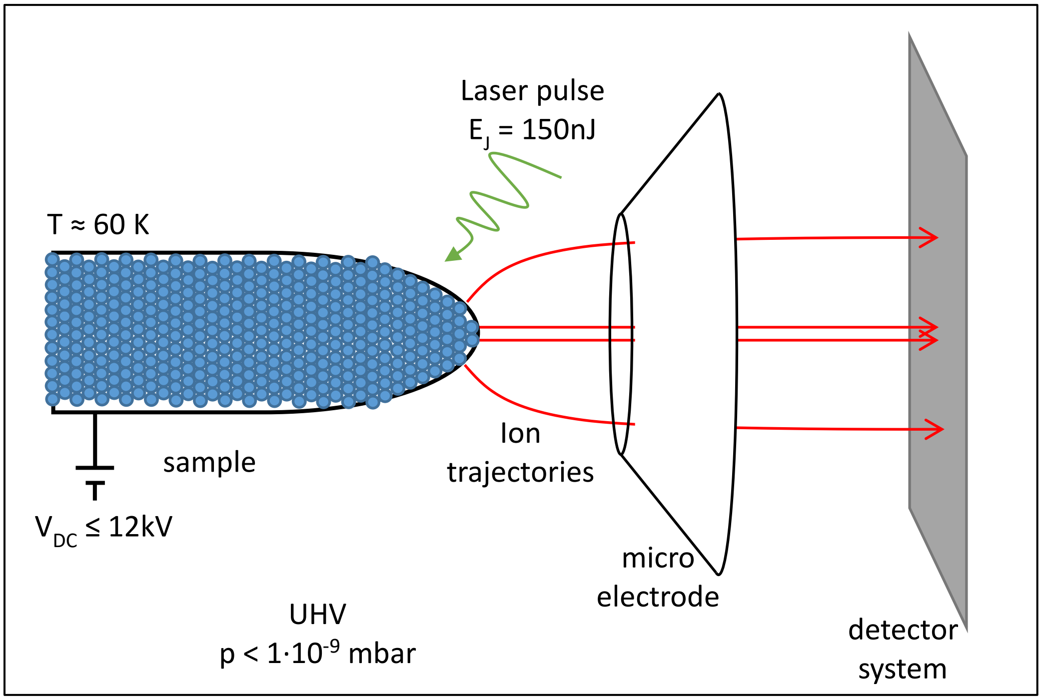

Figure 26: Schematic drawing of the APT. A high voltage is applied to the tip sample and a laser pulsing. The atoms (blue circles) are removed and accelerated towards the detector (grey) following the trajectories marked in red.

Measurement parameters:

The CuNi tips were measured at a temperature of 60 K using a femtosecond-laser from Clark with a frequency of 200 kHz and a power of 30 mW (pulse energy E_J = 150 nJ) at a wavelength of 335 nm (UV). The voltage was increased automatically according to an automated voltage control to realize an evaporation rate of atom-to-pulse ratio between 0.4 and 2%. The correct voltage was checked with a refresh rate of 0.2 s.

3.6.1 Reconstruction

With the detected positions, the initial atomic positions on the tip surface and the sample depth were calculated. This results in a volumetric reconstruction of the tip, including the chemical nature of the atoms received from the time-of-flight measurement. Herein, the time between the laser pulse and an impact on the detector is registered and measured (between 50ns and 10µs).

Assuming the ions receive their total kinetic energy E_{kin} on the sample surface when starting flying, and their potential energy E_{pot} is maximal there (and minimal at the detector), the energy conservation law can be used to equate E_{kin} and E_{pot} according to Eq.(35) and the mass to charge ratio *m/z* can be calculated:

$$\frac{1}{2}mv^2 = zeU \rightarrow \frac{m}{z} = 2eU\frac{t^2}{s^2} \tag{35}$$

Where *m* and *z* are the ion mass and charge, *e* the elementary charge number, *U* the total voltage, *t* the flight time and *s* the distance from the sample surface to the detector impact point.

For reconstructing the atom positions on the sample, the projection on the detector must be described mathematically. The point projection model reported by Bas et al. [66] is the commonly used model for this purpose. This model simplifies the ion trajectories to be straight, although curved in real, following the electric field lines. To correct this, the origin of the trajectory is not the tip sphere center *O*, but a projection point *P* slightly behind it (Figure 27). Using this model, the magnification *M* can be calculated, which is the relation between the distance of a surface atom to the tip axis *d* and its corresponding projected distance on the detector *D*. Using the intercept theorem, M is received by:

$$M = \frac{D}{d} = \frac{L+\mu R}{\mu R} \approx \frac{L}{\mu R} \tag{36}$$

With *L* being the flight path and *μR* the distance of *P* from the tip surface. *μ* is the compression factor. It is a value for the compression of the field lines and defined as $\mu=\vartheta_{crys}/\vartheta_{exp}$.

Knowing the magnification, the atom coordinates x_{tip} and y_{tip} on the tip can be calculated according to:

$$x_{tip} = \frac{X_D}{M} \text{ and } y_{tip} = \frac{Y_D}{M} \tag{37}$$

With X_D and Y_D as the corresponding atom coordinates on the detector.

The z-coordinate of the tip is described by the sequential removal of one atomic layer after another. Assuming the atom is located at the tip apex when evaporation is started, its initial position is $z_{tip}^{(i)}$. When the atoms of the apex are ionized and removed, the tip surface is incrementally shifted by one atomic layer, *dz*, and the new surface is defined as: $z_{tip}^{(i+1)} = z_{tip}^{(i)} + dz$ (from the detector). Using trigonometric considerations (see Figure 27), the tip surface is given as:

$$z_{tip}^{(i)} = R(1 - \cos(\mu\theta_{exp}) \tag{38}$$

dz can be calculated considering that the analyzed volume is the average atomic volume *Ω* of every ion *i,* divided against the part of the tip cross section A_e which is seen by the detector. Since the detector efficiency *η* is limited, it must be considered as well:

$$dz = \frac{\Omega_i}{\eta A_e} = \frac{\Omega_i M^2}{\eta A_d}. \tag{39}$$

With A_d as the open area of the detector.

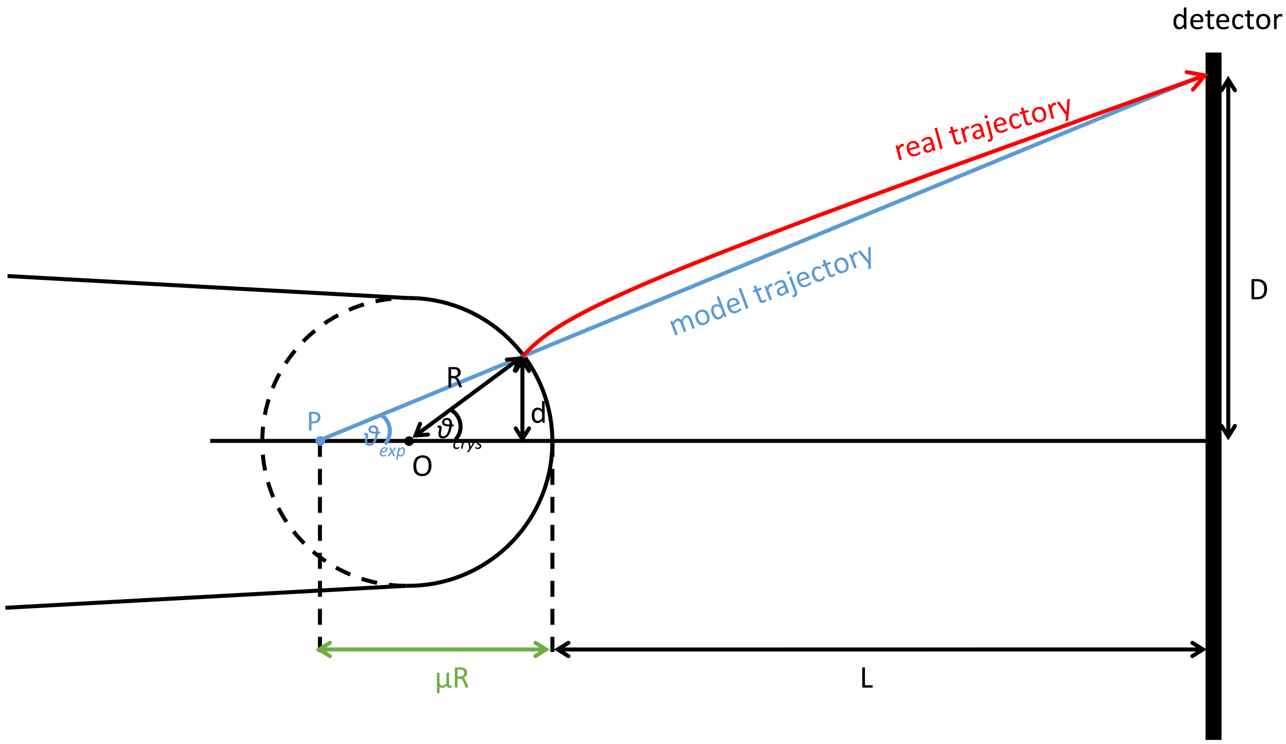

Figure 27: Schematic drawing of the point projection model

Using suitable computer software (*Scito* and *AVS* in this project), the chemical and positional information of all atoms of a sample are assembled as colored dots in a three-dimensional atomic map (Figure 28a). This atomic map gives already a first impression of the sample homogeneity or the content of defects like grain boundaries or precipitates. But to improve the visualization of chemical contrast, so-called isosurfaces can be created (Figure 28b). For this analysis, the atomic map is split into blocks and the composition is calculated. If it is over a defined threshold value, the blocks are highlighted in color. Neighbored highlighted blocks form a continuous isosurface [64] [65].

For quantitative analysis, a region of interest (ROI) is selected using geometric filters, like a cylinder or box. Then, the composition along the length of this filter is determined for a partial length size. Putting all compositions in a plot result in a one-dimensional composition profile. For further analysis, the atomic coordinates of the selected volume can be exported to use external software, like *Ovito* or *OriginLab*.

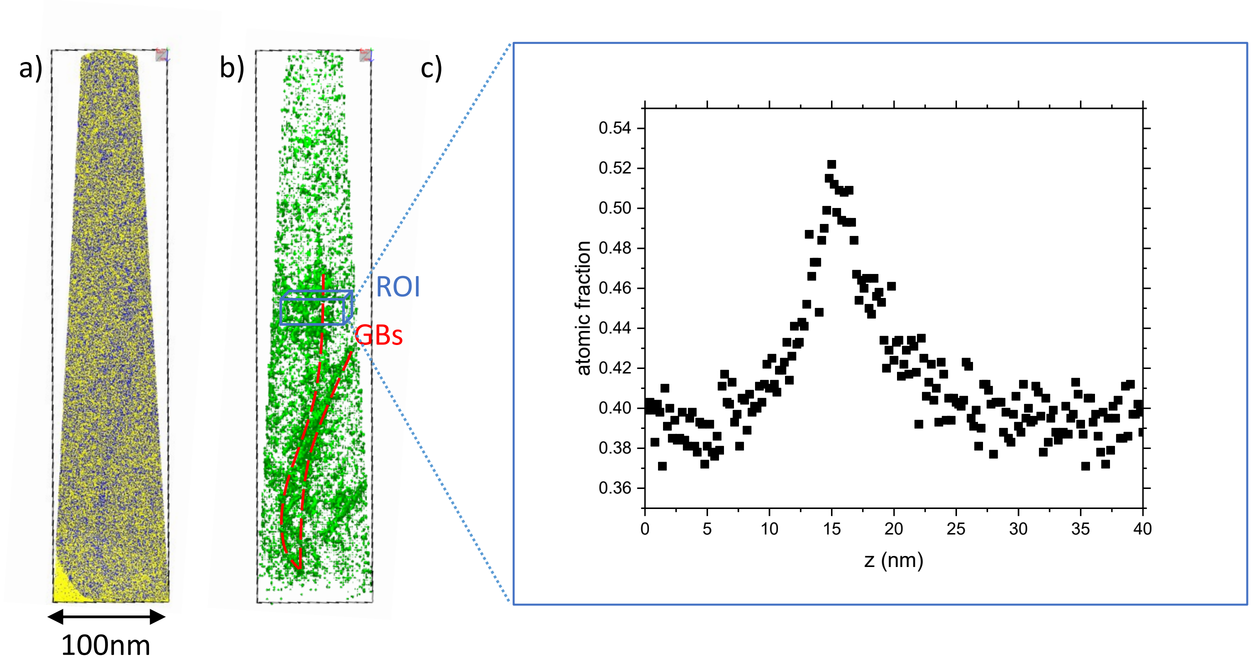

Figure 28: Atomic map (a)) and isosurface (b)) of a sample containing grain boundaries. A grain boundary is marked by a cylinder as ROI. The corresponding composition profile is shown in c).

3.6.2 Detector efficiency

The detection system of the APT consists of two microchannel plates (MCP) in chevron configuration and a delay-line electrode. The MCPs consist of many channels with honeycomb arrangement. When ions hit the inner channel wall, secondary electrons are emitted, and the signal is amplified. However, if the ions hit the front cross-section or go through the tubes, without contact, they will not be amplified and detected, so that a loss of detection events is recognized. This loss can be quantified as the detector efficiency η, by dividing the number of measured atoms by the theoretically expected number. The knowledge of η is significant, considering that it contributes to the reconstruction depth (see Eq.39) and with that, to defect dimensions. In addition, the detection limitations are affecting several evaluations, like the nearest neighbor analysis, the cluster characterization and frequency distribution histograms.

For the determination of η, the measured atomic content in the correct sample volume must be determined. The difficulty is the investigation of the exact sample dimensions, since a feature with known dimensions for calibration is missing and the scaling is further distorted by measurement artefacts. A usual procedure is the preparation of Spatial Distribution Maps (SDM) which determines distances between atoms. By doing this for every atom pair in a certain volume, the atomic distribution is calculated (either one-dimensional as histogram or two-dimensional as atomic map) showing periodicities of atomic distances. These periodicities coincide with atomic positions in a crystal lattice and are compared to theoretical values. Correction factors can be calculated if distortions occur. The atom number of the resulting volume is counted to calculate η. [64] [67]. Using this method, the detector efficiency in [67] was determined to be around 59% for their instrument, using a measurement of crystalline tungsten.

Unfortunately, the SDM procedure cannot be used for every measurement, since a good spatial resolution is required. This is affected by high measurement temperatures and using laser-induced evaporation rather than high voltage. The higher thermal energy increases the vibration of atoms at their initial positions. When they start evaporating, trajectory aberrations occur, and the calculated atomic positions will be distorted so much that the lateral periodicity is not seen in the SDMs anymore.

Another way for calculating η is by directly measuring samples or features with known lateral and linear dimensions. These dimensions can be previously determined by TEM. This direct measurement of η was also used in this project. A sample with a vertical multilayer stack of CuNi with defined layer thicknesses was used. The linear dimension was calibrated using the Cu and Ni lattice planes, as received from APT analysis. Then, a large reconstruction volume was cut, and its lateral dimension was corrected according to the TEM results. Since the TEM has a nanometer-sized resolution for measuring the layer thicknesses, the accuracy of this method is limited to this range. To calculate η, the number of atoms from this box were divided by the theoretically expected atomic number. An advantage of this method is that variations of η with depth and radial variations of η are considered by using large sample volumes, (nearly the whole cross section and length). This is not the case for the SDM procedure. Here, the evaluated volume is limited to a few nanometers around the tip center, since this region has the best lateral resolution [68]. In [68], the detector efficiency for two instruments was successfully determined to be 77% and 50%.

3.6.3 Density artefacts in the reconstruction

Since reconstruction is based on the atom trajectories, trajectory aberration will cause artefacts. Already the reconstruction of single crystals has regions with lower density stemming from zone lines and poles (directions with high atomic density). This is due to electrical field variations at these regions induced by higher repulsive interactions between the atoms at the starting of their flight. So, the ions are deflected and their impact points on the detector distorted, leaving certain areas empty. Such a deflection is also seen for grain boundaries, since the arrangement of atoms differ in both adjacent grains with a disordered interface in between.

Another property leading to density fluctuations are chemical inhomogeneities, like precipitates or segregated grain boundaries. Different chemical environments need different field strengths for evaporation. The one that requires the lower field will evaporate first, and thus the surface will not be removed equally, forming depleted or protruded zones on the tip surface. These deformed regions will deflect ion trajectories either inwards (for low-field defects) or outwards (for high-field defects) the defect which then causes an increase or decrease of atom density on the detector.

Although density artefacts can be advantageous for defect identification, they need to be considered in quantitative composition and distribution analysis. In a classical composition profile, for example, the profile is generated by selecting a certain volume and splitting the length scale into boxes (bins) of same size. For each bin, the concentration is determined, without considering the density. However, if the selected volume contains two chemically or structurally different regions, the different evaporation behavior will cause density variations. Then, the dimensions of these regions will be artificially broadened/compressed, and the dimension cannot be evaluated correctly anymore. Especially for the evaluation of the GB widths, this is a problem. A composition profile across the grain boundary width will have a Gaussian shape. The full width at half maximum of this Gaussian may represent the chemical width of the grain boundary. However, if the density varies, the width of the profile is artificially distorted.

To overcome these difficulties, the density must be correctly homogenized. In this project, this is done by molecular dynamics correction. Herein, the atoms of the region of interest were allowed to move for a certain time period, to fit with the theoretical lattice constant, based on an interatomic embedded-atom potential [8]. For the density homogenization, a short MD run of $\Delta t = 100$ fs at a temperature of $T = 300\ \mathrm{K}$ is already sufficient.

4 Results and Discussion

In this chapter, the experimental results are presented. The findings are compared to previous literature data and discussed. For the atom probe experiments, the Micro Electrode Tomographic Atom Probe (METAP) has been used, which is a custom-built, laser-assisted atom probe, presented in [63].

4.1 Thickness calibration

First, the actual thickness of the sputtered layers was investigated. For this, the layer thicknesses of a test sputtering were analysed via TEM. The tested sample consist of a silica plate with one layer of (Cu_{25nm}/Ni_{25nm}) as buffer, ten bilayers of (Cu_{10nm}/Ni_{10nm}) and a protective layer of 500 nm Cr, (see Figure 29a). Using the standard FIB lift-out technique, a TEM-lamella of this sample was prepared. Figure 29b shows the resulting cross sectional TEM image. Although the layers can be hardly distinguished, because of the low material contrast between Ni and Cu, the structural difference at the interfaces makes them visible (some are marked by red lines). The layers are planar and uniform, and their thicknesses correspond to the aimed sputter thickness.

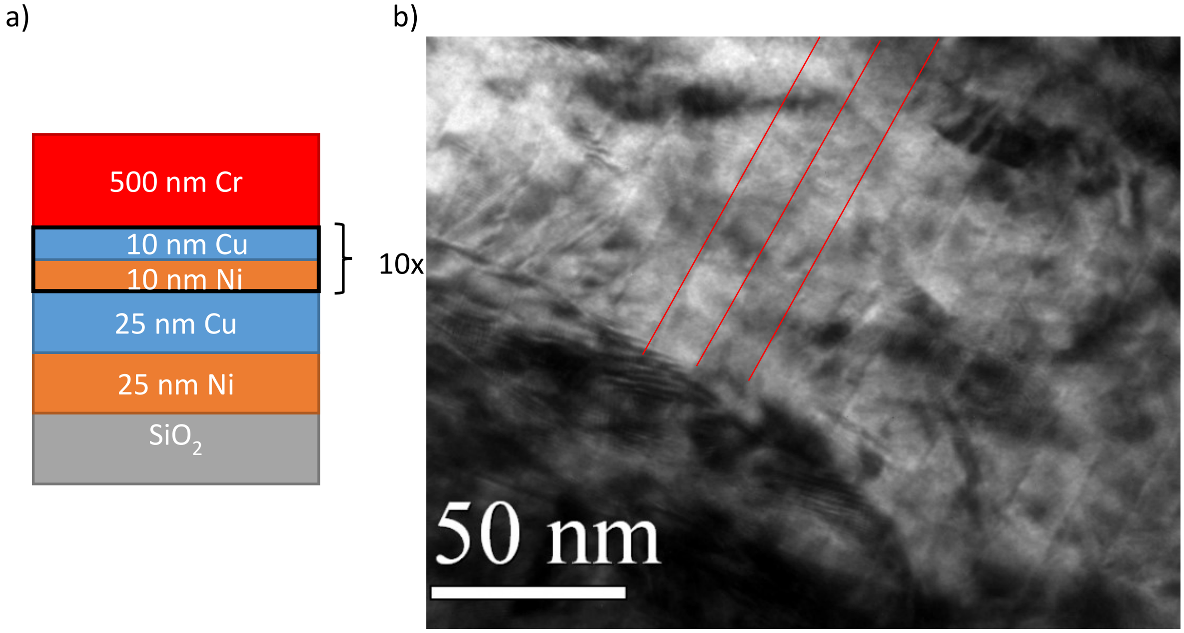

Figure 29: a) Schematic illustration of the sample for the calibration of the deposition depth and its corresponding TEM image (b).

To investigate the microstructure, a low magnification dark-field image with individual grain coloring was prepared, as show in Figure 30. The grains have a columnar arrangement, crossing several layers which indicates coherent interfaces. For the overall lateral grain diameter almost 25 nm is measured, whereas the lengths are over 100 nm. The specific chemistry of the layers is evaluated by EDX mapping with a spot size of 4 nm, as shown on the right inlet in Figure 30. The alternating layer structures for Cu (pink) and Nickel (yellow) are clearly visible, with the Ni layers being slightly thinner.

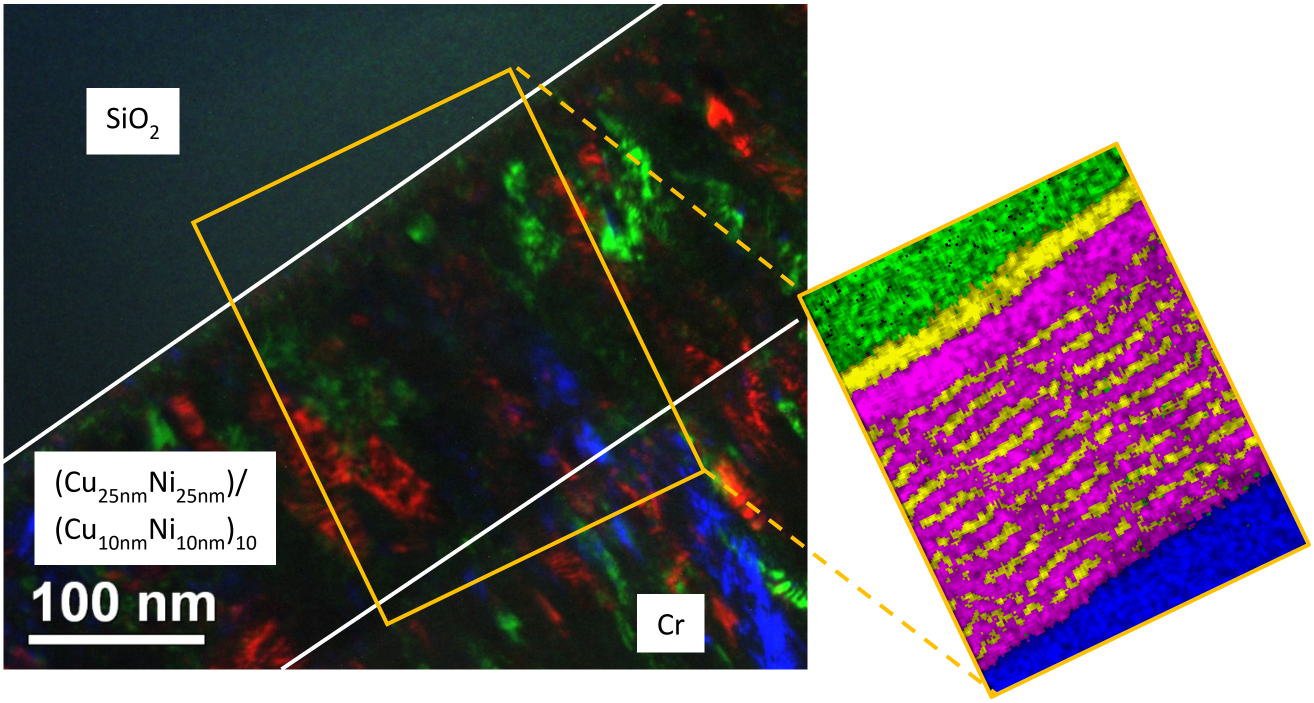

Figure 30: Colored overlay of different dark-field images from the lamella shown in Figure 29. The colors mark the different grains showing a spread through the whole layer system. On the right, an EDX map shows the layering of Cu (pink) and Nickel (yellow).

4.2 Miscibility gap

As described in section 3.2.1, multi-layered APT samples were prepared. To determine the suitability, with respect to chemical and local resolution of the alternating layers, as well as the capability of quantification, tips without annealing (as prepared) were analyzed first via METAP.

4.2.1 As prepared samples

A typical mass spectrum for a multilayered CuNi tip with 50 at.% Cu content can be seen in Figure 31. Cu and Ni are detected mainly single charged. The resolution is good enough, that even the ^{61}Ni and ^{62}Ni isotopes are visible although they have a very low isotopic abundance of 1.1 % and 3.6 %. A slight overlap occurs with ^{63}Cu and ^{64}Ni. However, the isotopic ratio of ^{64}Ni is so low (0,93 %), that this is neglected. In contrast to Cu, a small amount of Ni is detected in the double charged state. This is in accordance with the Kingham curves which predicts the necessity of a higher field for double charged Cu than for double charged Ni [69]. Despite minor residual impurities at mass ranges between 1 and 28 (hydrogen, water, N_2), which are usual for APT measurements, no further contaminations are visible.

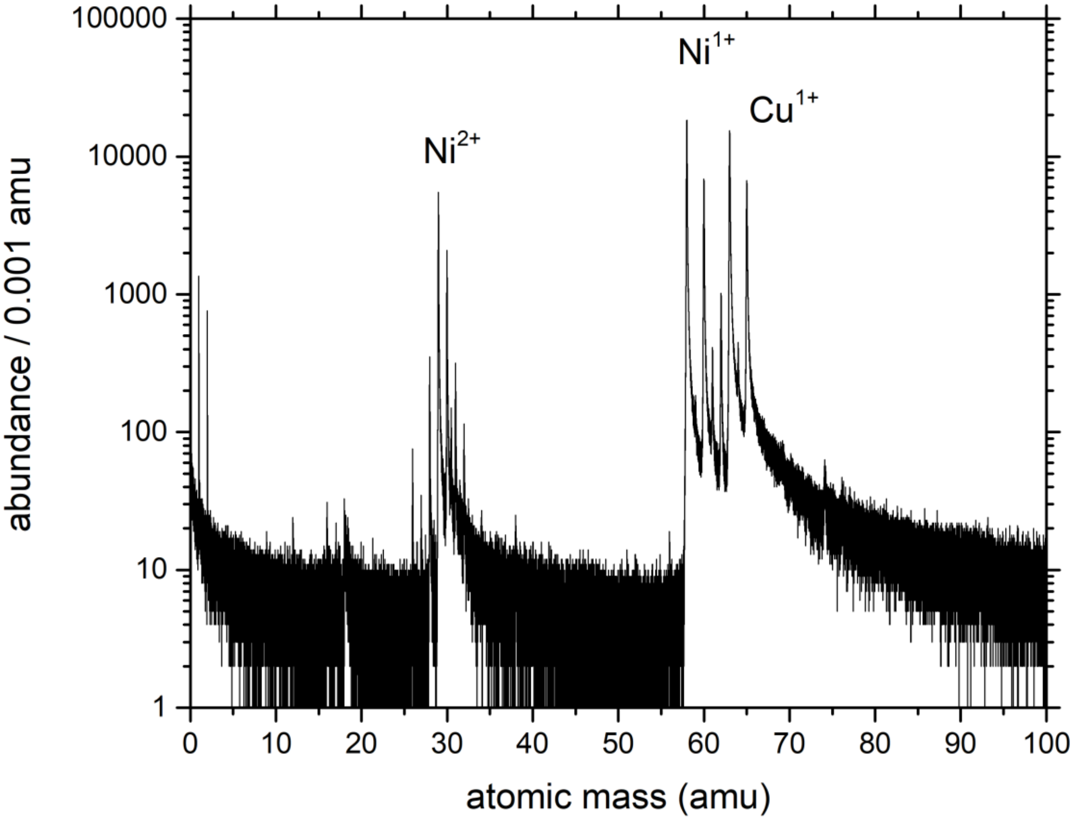

Figure 31: Exemplary mass spectrum received from an atom probe analysis of an as prepared measurement.

After the mass peaks were assigned to the corresponding elements, a three-dimensional reconstruction could be created, as shown in Figure 32. The layer structure with thin Cu layers (blue) and thick Ni-rich layers (yellow) is nicely visible. The layers are nearly straight, however, the thickness of the Cu layers varies in lateral direction and are broader at the center, and narrower outside.

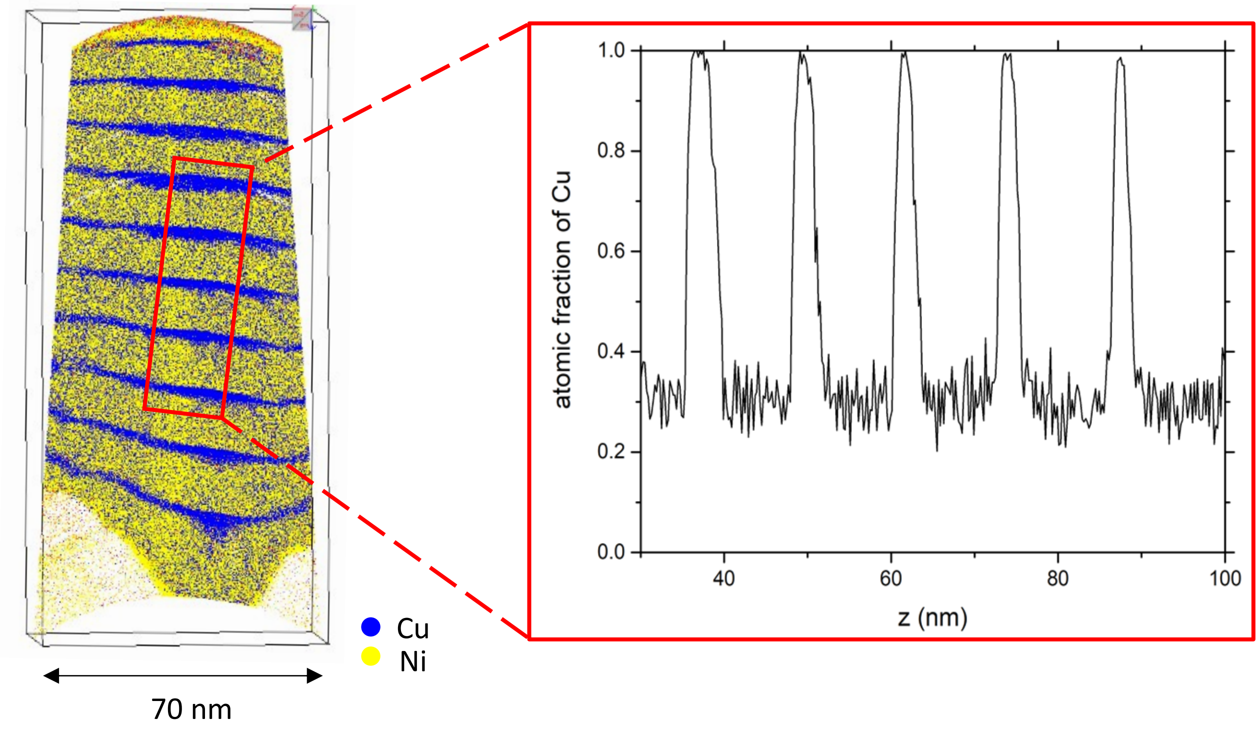

Figure 32 left: Three-dimensional reconstruction of an as-prepared tip with a layer system $\{Cu_{3nm}/(Ni_{70}Cu_{30})_{8nm}\}_{10}$*. At the bottom of the tip, low density regions on the sides are visible due to a huge difference of the evaporation field of Ni and W. Right: Composition profile of the red marked tip region.*

This observation is explained by a reconstruction artefact, caused by the planar layering and the lower evaporation field of Cu (30 V/nm) in contrast to Ni (35 V/nm). When the Ni-rich layer is on top of the tip, the tip surface is Ni-rich in the center, surrounded by Cu. Since the field to evaporate Cu is lower, the surrounding Cu is evaporated first or together with the Ni-rich center. When the Ni-rich center is completely removed, the rest of the Cu layer will be at the tip surface in the center. However, the Cu outside is evaporated already and just the centered Cu is evaporated.

The Ni-rich layer below requires a higher field, so it won't evaporate until the Cu layer is completely removed. This procedure is shown in the schematic below (Figure 33). Since the evaporation field difference between the layers is strongest for the as prepared tips, this artefact is strongest here. With annealing, mixing will be induced and the evaporation field difference between the layers diminishes.

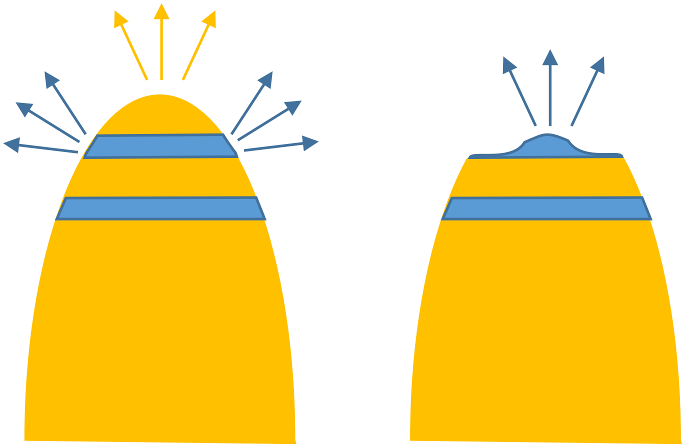

Figure 33: Schematic illustration of the evaporation procedure responsible for the inhomogeneous Cu layer thickness in the reconstruction.

For quantitative analysis, a composition profile is prepared out of the marked region in the reconstruction in Figure 32. The box has dimension of 10 x 10 x 80 nm^3 (red). With the resulting composition profile, shown on the right side of Figure 32, the layer concentrations and their thicknesses are analyzed. As expected, the Ni content in the Ni-rich layers is 70±1.4 at% and in the Cu layers 0 at% (pure Cu). The layer thicknesses are also in accordance with the aimed ones, which are 3nm for Cu, and 8nm for $Ni_{70}Cu_{30}$, although the lateral thickness variation of the Cu layers makes an exact definition difficult. However, since the aimed overall concentration is not affected by thickness variations, this is not relevant here and is therefore neglected.

4.2.2 Isothermal development

Depending on the annealing temperature and time, the samples are at different states of mixing. This can be seen already in the atomic maps of the reconstructed tips, shown after annealing at

673K in Figure 34. For easier comparison, boxes with the same sizes of 60x40x10 nm^3 are cut from tip regions with four Cu and three Ni-rich layers and were colored according to the local concentration of Ni. With increasing annealing time, the interfaces become blurry (especially between 2.5d and 7d) and the thicknesses of Cu and Ni-rich layers equalize. After 14d, the concentration difference within the layers vanishes and the layer structure is not visible anymore.

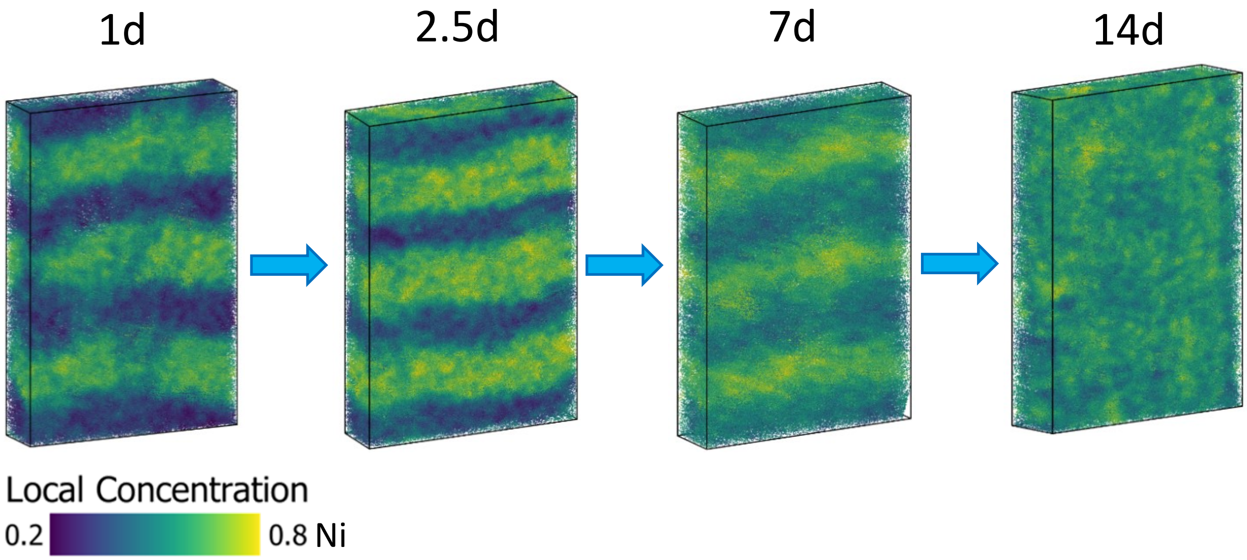

Figure 34: Local concentration plots from reconstructed tips, cropped in a box of volume 60x40x10 nm^3 annealed at 673K for different times to visualize the time-dependent intermixing.

The temporal evolution of the mixing can be clearly derived from one-dimensional composition profiles across the layers as depicted in Figure 35a, exemplary for samples annealed at 673 K. The as prepared profile (black) has a plateau at 70 at.% for the concentration of the Ni-rich layer and a peak to 0 at.% representing the Cu layer. This profile has the highest chemical contrast between the layers. With increasing annealing time, the peak concentrations merge towards complete mixing. In comparison to the as-prepared state (0d), the Ni concentration at the Ni-side for the 1d annealed sample lowers only slightly (around 4%), whereas on the Cu side, already a large step to higher concentrations is observed.

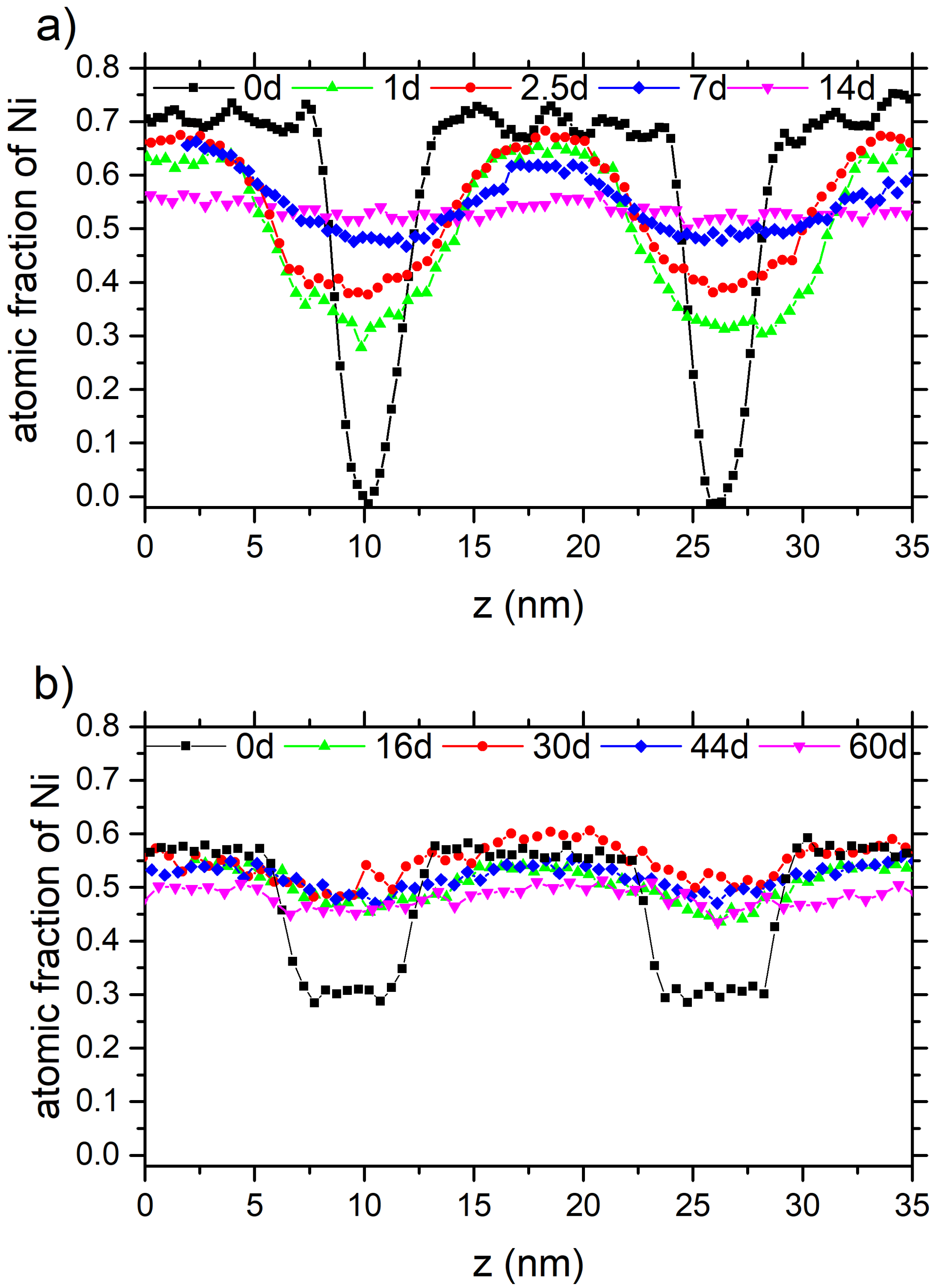

Figure 35: Measured composition profiles at 673K (a) and 623 K (b) for different annealing times.

This indicates a huge asymmetry in the diffusivities, demonstrating the concentration dependency of the diffusion coefficient, where the diffusion in Cu-rich alloys is way faster than in Ni-rich alloys. At this annealing time, the different layer thicknesses of the Cu- and Ni-rich layers equalize already. After 7d, a layering is still visible, with a concentration in the Cu layer around 50 at.%, and a Ni layer concentration of c(Ni) = 65 at.%. After 14d, however, the layer structure is nearly not visible anymore, with concentrations lying at c(Ni) = 55 at.% and c(Cu) = 53 at.%. Here, the layer concentrations may merge at the average, which varies slightly from 50 at.% due to concentration fluctuations in layer deposition.

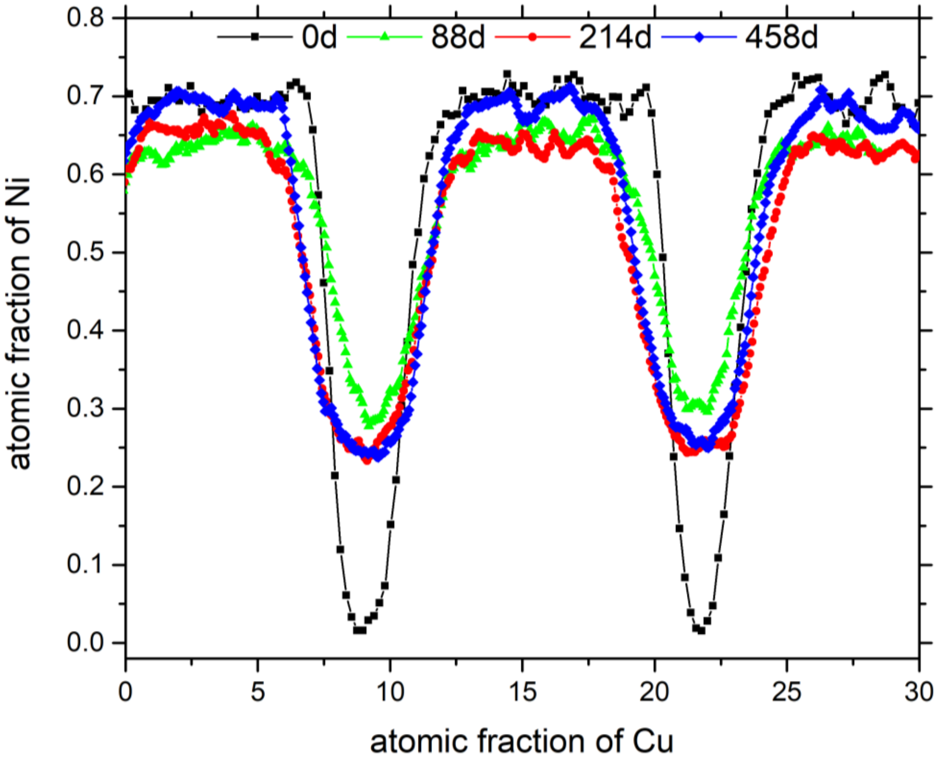

Figure 36: Measured composition profiles at 573 K for different annealing times.

Figure 35b shows a similar plot of samples annealed at 623K. To reduce the annealing time for reaching equilibrium, the starting concentrations of the layers are chosen to be 65 and 30 at.% Ni. Like the 673 K plots, a mixing is seen between Cu and Ni-rich layers with increasing time, with the highest effect after the first annealing time and an asymmetric diffusion. For the longer times, the layers merge equally to the average concentration, with small steps of around 5 at.%. Even after 60d, which is the longest annealing time investigated for this temperature, the layering is slightly visible. Whether this is a proof of limited miscibility or the annealing duration is insufficient, needs to be clarified by further investigation of the kinetics.

A crucial difference is observed for the composition profiles received after annealing at 573 K (Figure 36). Here, long-term annealing treatments for more than 1 year, namely 458d were fulfilled under UHV with a pressure of 10^{-8} mbar. In this case, after very long annealing of 88d, a merging of the layer compositions is seen. However, with further annealing up to 458d, the concentrations do not change anymore. Here, a miscibility gap is clearly evidenced.

4.2.3 Microstructural change during annealing

During mixing, Cu and Ni atoms from layers with high concentrations were transferred to regions with lower concentration, until thermodynamic equilibrium is reached. However, lattice transport requires high activation and is therefore the slowest mechanism. The transport over short circuit paths is possibly easier. Transport mechanisms like DIGM, cause heterogeneous microstructural transformation and remaining heterogeneity if the annealing times are not sufficient to reach equilibrium. For such samples, the kinetically controlled intermixing process can be analyzed, as shown in Figure 37. This figure shows the local Ni concentration maps of tip reconstructions from samples annealed at 673 K for different durations. Usual defects in thin films are grain boundaries. They are known to be fast diffusion paths with 10000 times faster diffusion [18]. Especially at low temperatures, diffusion over grain boundaries is the preferred transport route. An example of this transport mechanism is shown in Figure 37a. The alternating layer stack of the sample is disturbed by three lines representing GBs (red arrows), which are nicely visible due to their composition difference. The GB surrounding, the layer structure is disappeared, however, this is not a general case. Figure 37b shows another sample containing GBs, without a destructed surrounding layer structure. Note that the GB in Figure 37a consist mostly of Cu atoms (40 at.% Ni), while the GB in Figure 37b contains mainly Ni (65 at.% Ni). In the kinetic regime, both elements are transported over GBs, meaning both are localized in GBs and diffuse into grains. This happens faster for Cu, because of its higher mobility, resulting in high Cu content GBs. With time, the Cu atoms diffuse along the GB faster than the Ni atoms, resulting in GBs with a higher Ni content as seen in Figure 37b. So, this is a kinetic process. Then, the Ni atoms are solved in the bulk faster and just the Cu atoms are left in the GB, leading to high Cu concentrations in the GB as seen in Figure 37a. However, Cu has also a tendency to be segregated in GBs, even when equilibrium is reached, which is analyzed in more detail in section 4.4. In Figure 37a, the surrounding of the GB lost already the layered structure and become homogeneous. This indicates that the sample is closer to equilibrium than the one in Figure 37b, meaning that the Cu enrichment is may due to the equilibrium GB segregation.

Another effect during intermixing, is the formation of cluster-like structures with an increased concentration of around 70 at.% Ni (Figure 37c) or Cu (Figure 37d). This might be an effect of the fast Cu transport over GBs, getting enriched locally combined with migration of grain boundaries. Figure 37a, with GB segregation and simultaneously elimination of the surrounding layer structure represents probably the beginning of the formation of such clusters. If thermodynamic equilibrium is not reached, these structures can mistakenly be considered as clustering. However, they are not stable and vanish with increasing annealing time.

At temperatures outside the miscibility gap, some samples are observed consisting of a region which is completely mixed (52 at.% Ni) and a region, where the layer structure is still intact. Such an example is shown in Figure 37e, where the mixed and layered regions are split vertically, along the tip axis. This kind of intermixing can be almost certainly explained by diffusion induced grain boundary migration (DIGM). Herein, the equilibrium concentration is reached at the GB earlier, due to fast diffusion processes, and nucleation of the new (intermixed) phase is achieved (GBs are preferred nucleation zones). While the GB migrates further, a completely mixed region is left behind, becoming larger, the more the GB moves. So, the interface represents the GB and the mixed region represents the path of its migration.

As shown by the examples of heterogenous cases in Figure 37, the mixing development is not strictly controlled over the annealing time and bulk diffusion rates, but more by the heterogeneous microstructure. Since GBs work as fast diffusion paths, the higher the GB area, the faster the atomic transport.

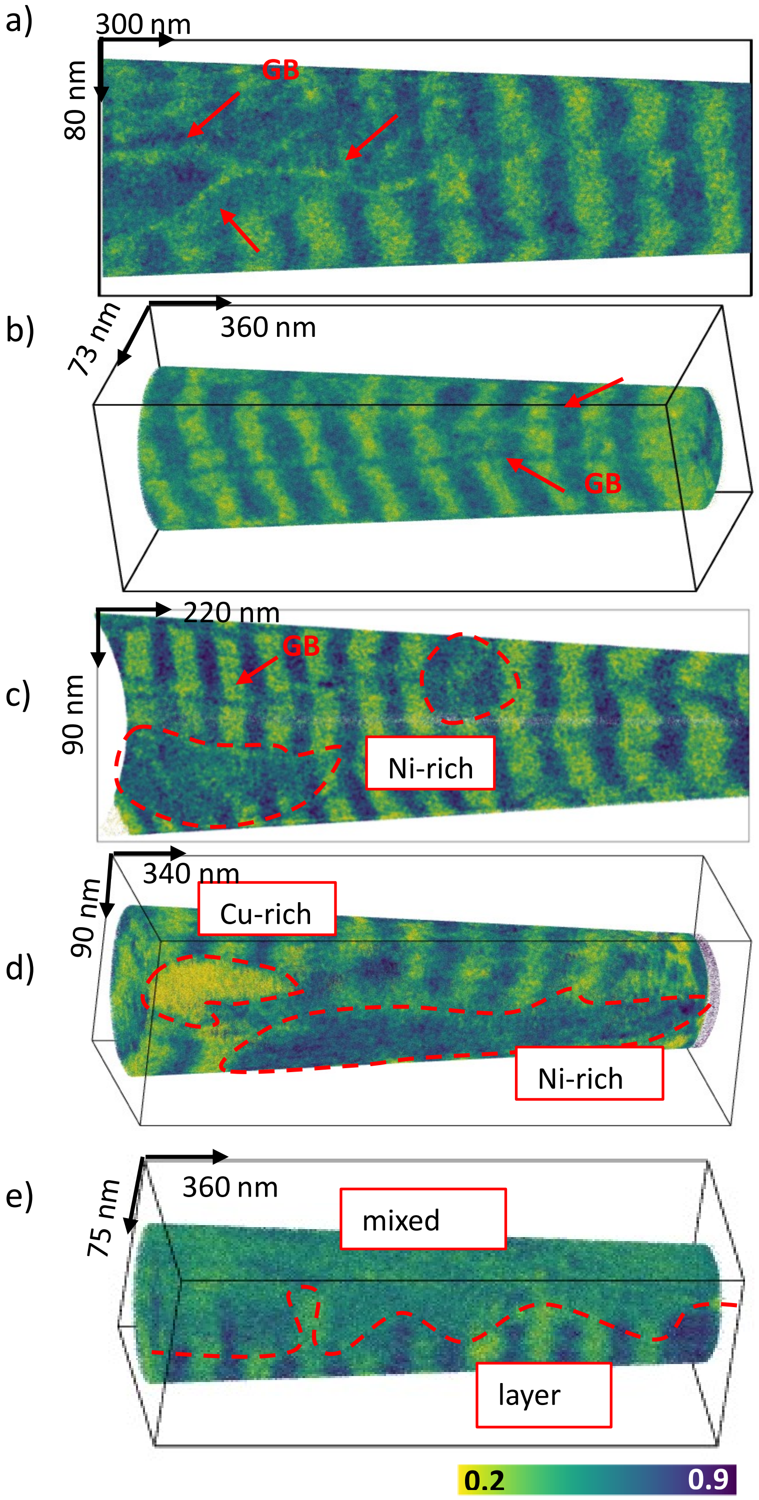

Figure 37: Local Ni concentration plots of tips in the kinetic regime annealed at 673 K with different microstructural inhomogeneities. In a) and b) atomic transport over grain boundaries is seen for tips annealed for 4.5d. c) and d) show Ni and Cu-rich volumes caused by grain boundary nucleation after 1d and 2.5d annealing. d) shows a tip with diffusion induced grain boundary migration after 4.5d annealing.

4.2.4 Determination of miscibility

To determine the phase boundaries of the miscibility gap, the time dependent concentration change at constant temperatures was investigated. Therefore, the respective layers in the composition profiles were analyzed. However, taking only the peak maxima and minima as layer concentrations is inadequate here, since contributions from interfaces will artificially reduce these values, especially for the narrow Cu layers. Instead, the profiles are analyzed as a whole and their trend is described analytically. For temperatures with diffusion-controlled mixing, the composition profiles were considered as diffusion profiles. With the knowledge of the starting layer concentrations (at $t = 0$) and the annealing time, the profiles can be fitted according to Eq. 20 and the layer concentrations can be determined. As an advantage, the effective diffusion coefficient D is received as a fitting result, too. Note that for diffusion-controlled processes, the layer concentration will vary according to the diffusion time and D will be constant, since it's independent of time. In contrast, for temperatures where phase separation occurs, the layer concentration will stay constant after a certain annealing time, and thus, the apparent D is not constant anymore. So, the possible change of the diffusion coefficient serves as an additional indicator for miscibility.

For the analysis, composition profiles as shown in Figure 35 and Figure 36 were evaluated for each annealing temperature at different annealing times. Therefore, analysis boxes of 10 x 10 nm^2 cross section and up to 80 nm length were placed in tip regions with visible layer structure and oriented perpendicular to the interfaces. Along these rectangular prisms, composition profiles were extracted and fitted according to Eq.(20), to calculate D and to investigate the temporal layer evolution. The process is diffusion controlled, if the change in the layer concentrations is in accordance with Eq.(20), and the determined D is constant. In this case, the system is understood as completely miscible at this temperature.

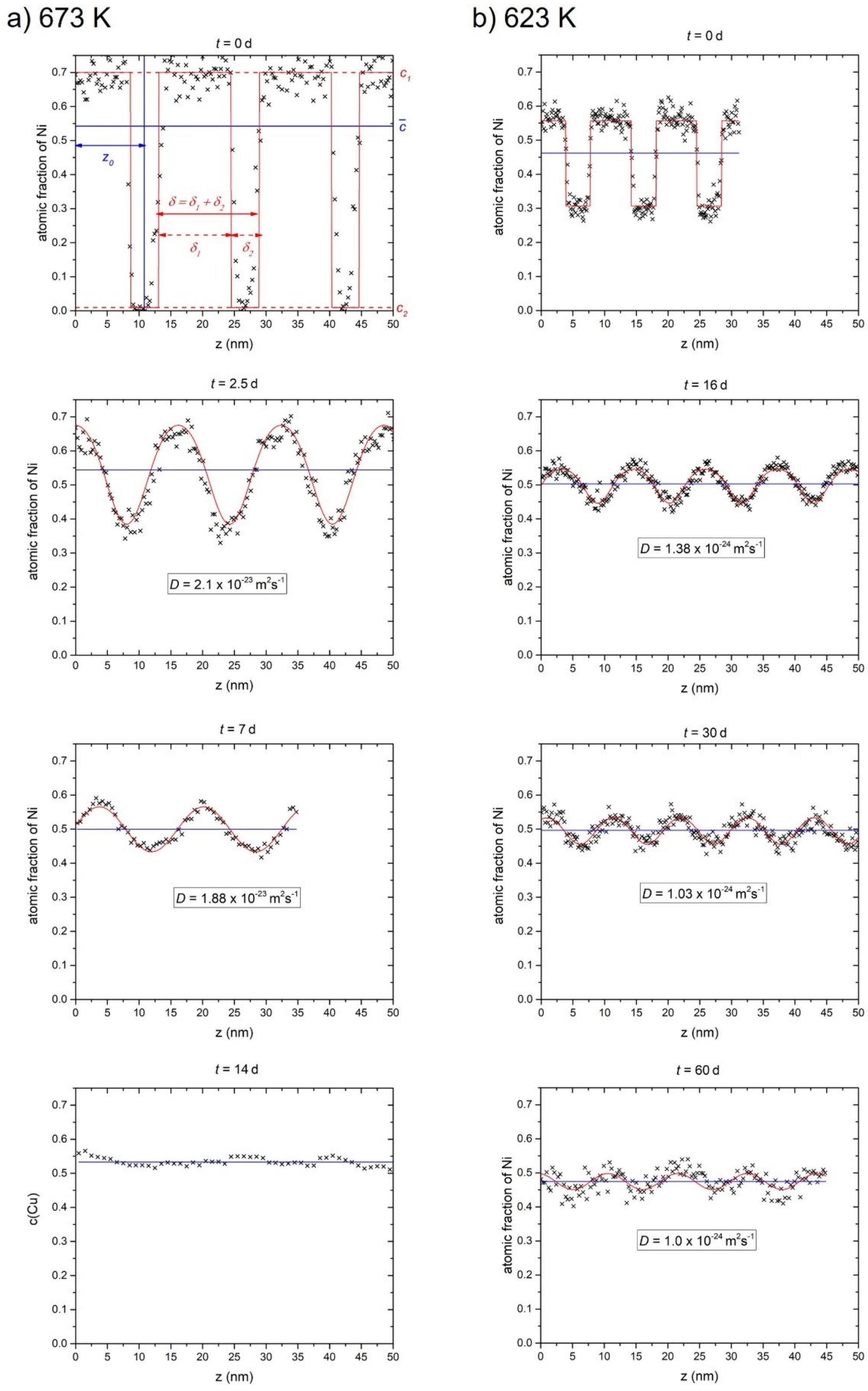

Figure 38: Exemplary fitted (red line) composition profiles according to Eq.(20) for 673 K (a) and 623 K (b) (black crosses) at different annealing times.

For the temperatures 673 K and 623 K, some exemplary fitted profiles are shown in Figure 38. The experimental profiles are marked by black crosses and the corresponding fit by red lines. The blue line represents the mean concentration, which is a result of fitting, too. Generally, the fits are in good agreement with the experimental curves. Some oscillations appear stemming from statistical fluctuations. With increasing annealing time, the peak concentrations (profile amplitudes) are damped exponentially towards the mean concentration (blue line). The diffusion coefficients determined after different annealing times remain almost constant at both temperatures. At 673 K, the profile reaches the mean concentration after 14d. Although some fluctuations are still visible, no distinct regions with differing composition were found and the general trend clearly indicates miscibility. For 623 K, a complete mixing could not be observed. Even after 60 d, a slight sinusoidal periodicity with around 5 at.% amplitude is left. However, considering the continuous decrease of the concentration amplitudes according to Eq.(20) and the constant D, it can be ensured that full mixing has just not been achieved because of still too short annealing times. Furthermore, if the system would be immiscible at this temperature, concentration plateaus would be formed at the highest mixed compositions, representing the homogeneous phases, which are not seen here.

The possibility of insufficient annealing time was further tested by using the diffusion coefficient received from all profiles at 623 K and calculating the time necessary to reach equilibrium with less than 1at.% remaining amplitude. Such annealing treatment must be at least 77 d, which explains, why complete miscibility was not observed in the experiments, where the longest annealing time was 60 d.

4.2.5 Determination of the diffusion coefficient

With the knowledge that the profiles at 673 K and 623 K represent a diffusion-controlled process, an effective diffusion coefficient, D_{eff}, can be determined, which is valid for the overall nanocrystalline microstructure of the samples used in this study. With this information, the times necessary for reaching thermodynamic equilibrium can be reliably estimated. Diffusion kinetics in NiCu was already investigated several times [70, 71, 72, 18], resulting in a wide range of different diffusion coefficients. The reason is obviously the dependency of D on the microstructure, the analysis technique, and the thermal range, since extrapolating to the required temperatures cause additional deviations. From Eq.(20) it's clear that the kinetics has a square dependency from the single layer thicknesses, which is hardly equal for all tips. Though, this fluctuation is determined in the fitting process and treated correctly to calculate the diffusion coefficients accurately. The resulting diffusion coefficients of all evaluated profiles for both temperatures are plotted against the annealing time in Figure 39. As expected, the diffusion coefficients at 623K (black diamonds) are lower than those at 673K (red circles) but both are reasonably constant, at least for the longer annealing treatment. For early stages of the annealing treatments, a slight change in D is seen, becoming lower with time. This is due to the concentration dependence of *D*, since with time, the difference in the layer concentrations vanishes and converges to be approximately 50 at.%.

The diffusion coefficients from all 54 profiles determined at T = 623 K and from all 45 profiles at T = 673 K (see Figure 39) were averaged and plotted as an Arrhenius diagram in Figure 40, together with literature data for chemical diffusion of Cu into Ni. The measured diffusion coefficients of the present study agree well with the interdiffusion coefficients from Johnson et. al, where deposited CuNi bilayers of 500 nm thickness were analyzed via Scanning Auger Microprobe [18]. Regarding the transport process, both investigations analyze the interdiffusion between nanocrystalline thin films at nearly the same temperature range. On the other hand, the diffusion coefficients measured in [71] and [72] are in good accordance to each other but have huge discrepancies to the present study. In these investigations, coarse grained Ni samples were coated with a thin Cu layer and the lattice diffusion is determined at high temperatures. So, the approaches are similar to each other but differ in comparison to the present study with respect to their microstructure and diffusant source. In coarse grained samples, the amount of fast diffusion paths like dislocations or grain boundaries is less, and the diffusion needs to take place mainly over the volume, which is the slowest form of diffusion. In thin film microstructures, however, a fast diffusion, controlled over short circuit transport is predominant, resulting in strong differences considering *D*. In our samples, the existence of GBs was confirmed over the microstructure analysis and DIGM is evidenced, so high diffusivity paths were proven.

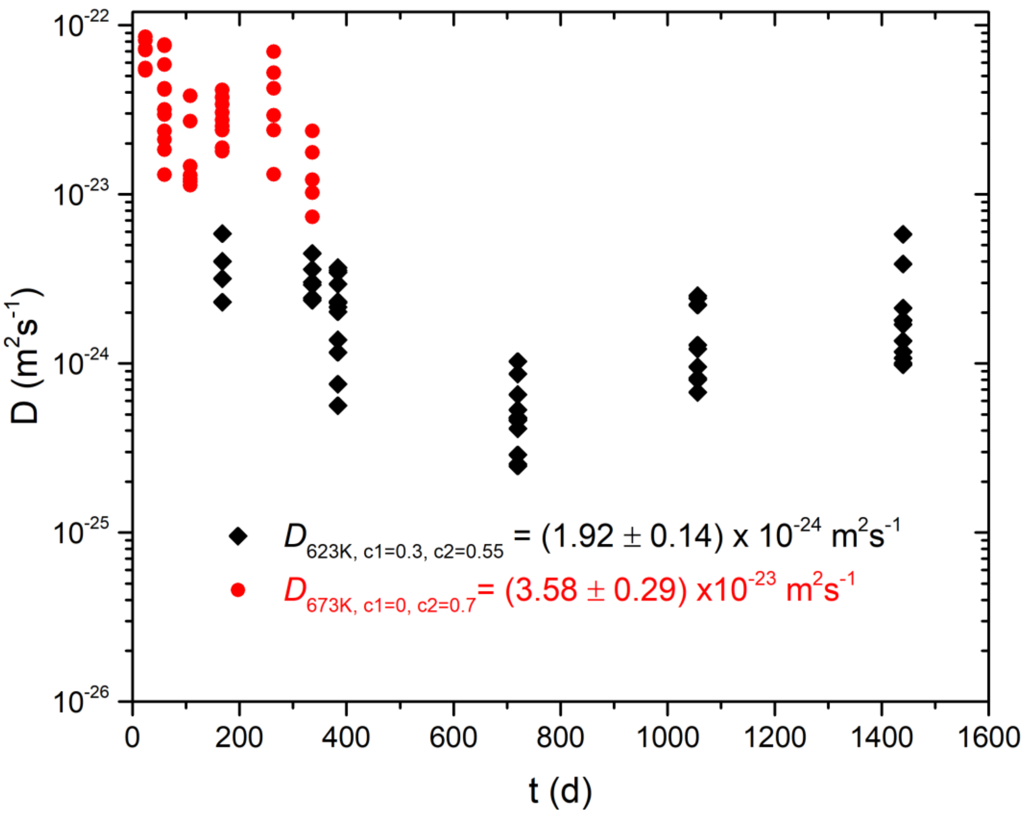

Figure 39: Diffusion coefficients D of all composition profiles measured at 673 K (red circles) and 623 K (black diamonds) in the present work.

The diffusion coefficients measured by Matano clearly deviate from the other in the Arrhenius plots, shown in Figure 40. Considering that this data represent the first diffusion study made for this system and therefore the oldest, the equipment probably didn't allow precise determination of transport data and consequently led to uncertainties.

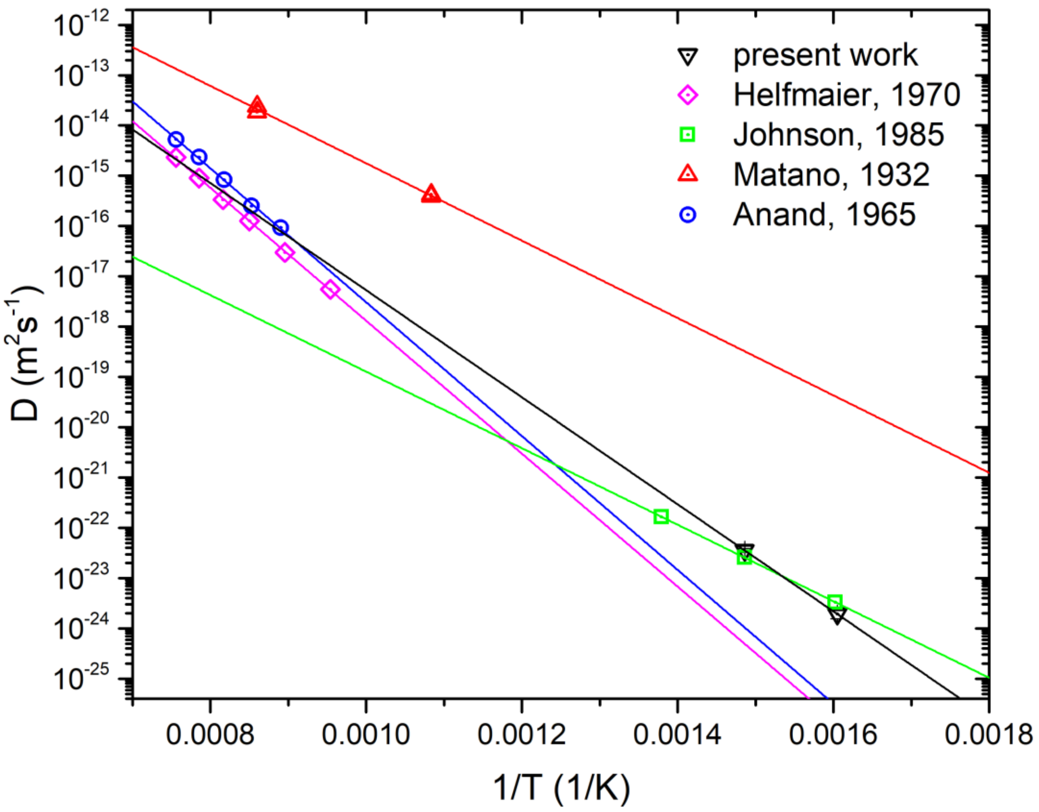

Figure 40: Arrhenius plots of diffusion data from present work (black triangles) in comparison to literature data. Helfmaier [72] (purple diamonds), Anand [71] (blue circles) and Matano [70] (red triangles) studied the Cu diffusion from a thin layer into polycrystalline Ni, whereas Johnson et al. [18] (green squares) investigated interdiffusion of CuNi thin film couples similar to this study.

From the Arrhenius plot of the present study, the characteristic parameters for D_0 and H may be determined to be $D_0 = 1.86 \times 10^{-10}$ m^{2}s^{-1} and H = 164 kJmol^{-1} although two datapoints are a weak base. These parameters are compared to the literature values presented in Table 2. Despite the fact, that the present work investigated the interdiffusion in nanocrystalline thin films (averaged on the full concentration range and with possible defect contribution from grain boundaries), they are still comparable to the diffusion data of pure Cu into Ni crystals. Since the diffusion into Ni is way slower (1000-times in the studied temperature range, according to [18]) than diffusion into Cu, the rate-determining process for the interdiffusion is obviously the volume diffusion of Cu into Ni.

Table 3: Comparison of diffusion data found in the literature for diffusion of Cu into Ni with the present study.

Source	D_0 (m^2s^{-1})	H ($kJmol^{-1}$)	Kind of diffusion	Measurement
Present work	$1.86 \cdot 10^{-10}$	161.1	Interdiffusion in thin film couple	APT
Helfmaier	$2.70 \cdot 10^{-5}$	255.3	Lattice diffusion from thin film source	Microprobe analyser
Johnson	$5.20 \cdot 10^{-12}$	145.7	Interdiffusion in thin film couple	Auger Depth Profiling
Arnand	$7.24 \cdot 10^{-5}$	255.2	Lattice diffusion wit Cu tracer	Residual Activity
Matano	$1.1 \cdot 10^{-7}$	148.5	Lattice diffusion from thin film source	X-ray studies

4.2.6 Determination of the phase boundaries of the miscibility gap

The resulting composition profiles for an isothermal annealing treatment at T = 573 K are shown in Figure 41. In addition to the assumption of phase separation at this temperature, which was made already in Section 4.2.2, these plots further confirm this when they were compared to predicted profiles, expected for diffusion-controlled intermixing for each annealing time, using Eq. (20) and *D*, extrapolated from the Arrhenius plot in section 4.2.5. The resulting profiles are shown in Figure 41 as blue dashed lines. After 88d annealing, the predicted diffusion profile is in good agreement with the experimental profile, well indicating a diffusion controlled mixing behavior valid for this annealing time. After 214d, however, a difference around 10 at.% between the model and experimental Cu layer concentration can be seen, while the concentrations of the Ni layers are similar. By increasing the annealing time to 458 d, the diffusion model predicts a merging of the layers to the average concentration with a compositional difference of just 3 at.%. This is in strong disagreement to the experimental profile, which still has the same layer concentrations as in the 214 d-profile. This clearly demonstrates a saturation of the layer concentrations, known as the phase equilibrium, and consequently the existence of a miscibility gap at this temperature.

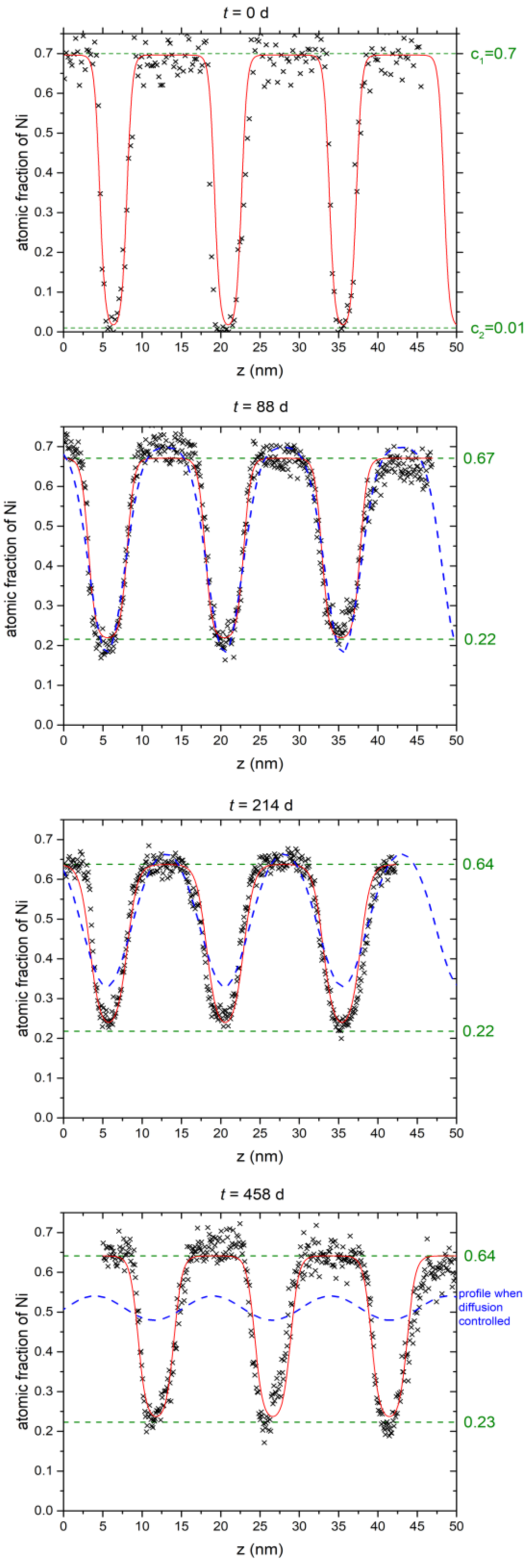

Figure 41: Exemplary composition profiles of T = 573 K for all annealing times (0d, 88d, 214d and 458d, black crosses), together with the fit according to Eq.(40) and the received plateau concentrations (green dashed line). The predicted profile according to a diffusion-controlled case is marked as a blue dashed line.

Since phase separation occurs at this temperature, the analytical model describing the concentration profile must be adjusted to clearly evaluate the equilibrium concentration. Instead of Eq.(20), a model separating two phases by an interface is necessary. Therefore, the Cahn-Hilliard approach [27] is used according to:

$$h_i(z) = \frac{1}{\exp\left(\frac{-4(z-(z_{0,\alpha}+i\delta))}{w}\right)+1} - \frac{1}{\exp\left(\frac{-4(z-(z_{0,\beta}+i\delta))}{w}\right)+1}. \tag{39}$$

Eq. (39) is derived from Eq.(15) by considering, that the composition profile consist of an periodic array, with the period δ, with one period representing one double layer. So, two sigmoid functions are summed. With $z_{0,\alpha}$ and $z_{0,\beta}$ as the interface positions. The full composition is given by:

$$c(z) = c_2 + (c_2 - c_1)\sum_{i=0}^{n-1} h_i(z) \tag{40}$$

With n as the number of periods and c_1 and c_2 as the layer concentrations in the equilibrium.

The fits according to Eq. (40) are plotted in Figure 41 as red lines, together with the equilibrium compositions, received as fitting result, which are shown as green dashed lines. The received equilibrium compositions are slightly higher than the profiles peak maxima. This is due to the narrow layer thicknesses in the Cu-layer and limited spatial resolution, so that the impact of the adjacent layers is high enough to already reduce the plateau values.

With these results, the critical temperature of the miscibility gap, T_c, can be restricted to lie between 573 K and 623 K. The phase boundaries at 573 K lie at 26.0 and 65.7 at.% Cu. Using this information, the likely phase diagram can be calculated by applying the Redlich-Kister parametrization of the Gibbs energy (Eq.(11)), [73]). In this equation, the values for L_0 and L_1 were determined, using the common tangent method to recover the measured concentrations of the phase boundaries. Once, L_0 and L_1 are known, the whole miscibility gap can be constructed.

The free coefficients were found to be L_0 = 10.006 kJ/mol and L_1 = -0.695 kJ/mol leading to the calculated miscibility gap, shown in Figure 42 (red line). The phase boundaries received experimentally are marked as red triangles. With this graph, the T_C is predicted to be at 608 K at a concentration of 45 at.% Ni.

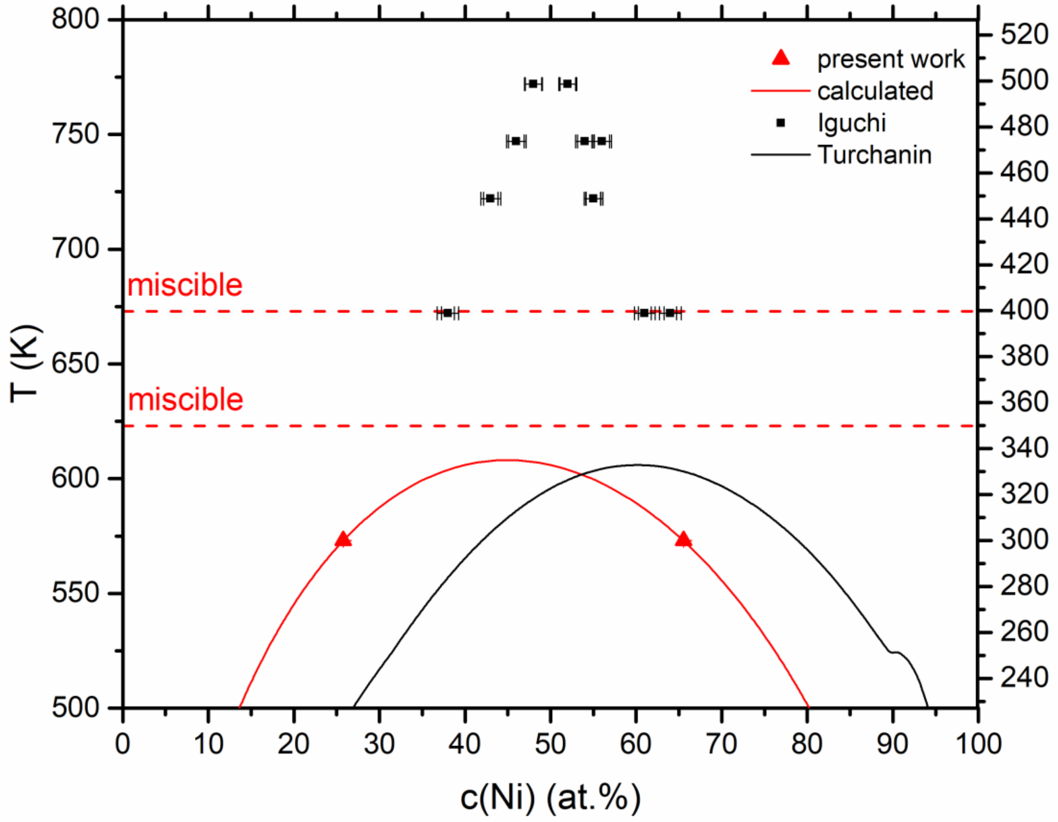

Figure 42: The experimentally measured phase boundaries (red triangles) and constructed miscibility gap (red line) together with the measured miscible temperatures (red dashed line). The black squares represent the experimentally measured miscibility gap by Iguchi et al. [17] and the black line the latest CALPHAD style miscibility gap [74].

Figure 42 contains also the latest published CALPHAD miscibility gap (black line) [74] and the only other experimental data on the miscibility gap (black squares) [17]. The form, temperature range and T_C of the CALPHAD miscibility gap is in good agreement to the recent work. However, oppositely, it is shifted to Ni rich concentrations, whereas our miscibility gap is shifted to Cu-rich concentrations. In comparison, the experimentally determined miscibility gap from Iguchi et al. is not matching at all and lies at way higher temperatures, at which our experiments have clearly demonstrated full mixing.

Beside these studies, several attempts were made, to determine the miscibility gap, leading to a broad spectrum of critical temperatures, summarized in Table 4. Starting with the research on a ternary NiCrCu-system from Meijeirng et al. [75], a phase separation of CuNi was ensured, since a three-phase equilibrium was observed which is just possible when Cu and Ni demix. By calculating an interaction parameter, T_C was determined to be 450 K, although it was referred that this is rather a rough estimate.

Further knowledge about the miscibility gap in CuNi alloys was gained by Pawel and Stansbury [76], as they investigated the specific heat of samples with 90, 75 and 50 wt.% Ni content for temperatures up to 873K. They found anomalies in the data, which was assumed to come from inhomogeneous Ni distributions. The maximum temperature for these anomalies is found at 673K for 75 wt.% Ni, which is then interpreted as the T_C.

Although these investigations support the existence of phases separation, a quantitative analysis was realized for the first time by Mozer et al. [77] using neutron diffraction scattering to measure a CuNi alloy with c_{Ni} = 47.5 at.%. The short-range order parameters were determined, and the interaction energies were calculated out of them. With this information, the critical temperature was predicted to lie between 506 and 536 K. This result is already very close to the T_C found in the present work. The discrepancies probably come from the assumptions made for the theoretical description. Additionally, the authors reduce their calculated T_C of 595 – 631 K by a factor of 15%, since this error is presumed for the used technique. Without this error estimation, the T_C fits even better to the result in the recent project. Using the same experimental procedure, Vrijen [78] made a prediction of the whole miscibility gap, applying a theoretical model from Clapp and Moss [79]. The maximum of the miscibility gap was found at 65 at.% Ni for a T_C of 613-623 K. Although T_C is in good agreement with our data, the composition of the peak maximum shows a huge discrepancy. The shift towards Ni-rich concentrations comes from the asymmetric behavior of the first-neighbor order parameters α. At the bottom end, the shift towards higher Ni concentrations with decreasing temperature, stems from a self-amplifying effect of many-particle interactions. In our experiments, the diffusion via thermal vacancies was investigated, meaning that the parameters necessary for the calculation were received from high temperature annealing. This might be the reason for the differences.

Alternatively, irradiation-induced diffusion can increase the atomic mobility and therefore reduce the annealing time, leading to a more precise prediction of the miscibility gap. This was made by Wagner et al. [80] for an CuNi alloy with 59 at.% Ni. Here, special care was taken during the annealing of the samples, since this is crucial for clustering. To improve contrast, only ^{62}Ni and ^{65}Cu isotopes were used for the scattering experiments. The resulting T_Cs were 527 K for a coherent, and 575 K for an incoherent miscibility gap. These values for T_C are slightly lower than found in [78] and in the present work, however, also the sample concentration is differed. Since in that research, not the whole miscibility gap was modelled, the real, higher T_C might occur at lower Ni concentrations, as indicated in the present study.

Another approach for determining T_C was made by Ebel [81]. Through X-ray diffraction, an increase of the lattice parameter after decomposition was measured for samples with 50 at.% Cu and Ni at T = 523 K. For temperatures higher than 573 K, no decomposition was observed, meaning the resulting T_C lies between 523 and 573 K. However, considering that the lattice parameter increases, and the measurement accuracy are both in the range of $1 \cdot 10^{-4}$ Å at this temperature, the low impacts at higher temperatures may just have not been detected.

Using the same technique, Tsakalakos analyzed the phase separation on composition modulated samples. From theoretical considerations of the peak intensities, a T_C of 603 K was determined at a composition of 45 at.% Ni, fitting very well with the results in the present work.

An analysis of the CuNi decomposition with 70 at.% Ni was made by Lopez et al. [82]. By evaluating the autocorrelation of the composition profile, the particle distribution has been detected. For both annealing temperatures, 473 K and 573 K, phase separation was measured. At this concentration and temperature, also our experiments show phase separation, however, these temperatures do not represent the T_C.

All this research is based on indirect determination of the miscibility gap by using theoretical consideration. Depending on different theoretical assumptions, the parameters used for the calculations may vary and the exact T_C is typically a calculation result. Therefore, errors were concerned just by assumption or experience, ending up in a broad variety of T_Cs. The T_C found in the present work by a direct experimental approach was compared to a recently undertaken direct experimental study of the CuNi miscibility gap from Iguchi et al. [17]. Herein, thin film samples with 30-70 nm thickness of pure Cu and Ni were investigated. Composition profiles were determined by depth profiling with SNMS (secondary neutral mass spectroscopy) pointing out to a T_C of 780 K at 50 at.% Ni. These values exceed the T_C of all other studies by far. Further, the found miscibility gap has a very narrow shape, which is unusual for a (sub)regular solution model.

For the determination of phase separation, the annealing treatment must be sufficiently long, what is ensured in this work by determining an effective diffusion coefficient and a following educated guess of the required annealing time. Since this data was missing in [17], the diffusion model of the present work was used to calculate the annealing times necessary for reaching thermodynamic equilibrium for the samples of [17]. Considering a simple layer thickness of 30 nm each, the annealing times necessary would be estimated to be 362 h for 723 K, and 2622h for 623 K, while [17] used only 168 h. Hence, the high T_C and the unusual shape of the miscibility gap may be caused by inadequate annealing.

A usual way in calculating phase diagrams from various thermodynamic data is the CALPHAD approximation. The latest CALPHAD style phase diagram from CuNi was made by Turchanin et al. [74] with a T_C of 605 K at c_{Ni} = 60 at.%. In comparison to other calculations, the phase diagram from Turchanin et al. contains various experimental research on structural, electrical, and magnetic properties. Additionally, the mixing enthalpies and activities are not just taken from liquid, but also from solid solutions. During all calculations, care was taken for a self-consistent description of all thermodynamic data.

While the T_C and the miscibility gap shape is fitting nicely with the data of the present project, the phase boundaries are shifted by around 10 at.% to higher Ni contents. Although the annealing times used in our experiments were long enough to reach equilibrium in a clear layer geometry, heterogeneous transport along the GBs can destruct the sample geometry and lead to precipitates, causing extension of the necessary annealing times. Especially on the Ni-rich side, this plays an important role due to the slow kinetics and can even shift the phase boundaries to higher Ni concentration.

Table 4: Some literature values for critical temperatures, T_C and boundary concentrations, c(Ni) in CuNi alloys

Reference	Method	T_C [K]	c_{Ni} [at%]
Meijering, 1957 [75]	Theoretical calculations of ternary phase diagram	450	
Pawel, 1965 [76]	Specific heat measurements	673	52 – 77
Mozer, 1968 [77]	Neutron scattering	506-536	47.5
Vrijen,1975 [78]	Neutron scattering	613-623	65
Wagner, 1982 [80]	Neutron scattering	575	59
Ebel, 1971 [81]	X-ray diffraction on spinodal decomposition	523-573	10-90
Tsakalakos, 1981 [83]	X-ray diffraction with composition modulation	603	45
Lopez, 1992 [82]	AP-FIM	573	70
Iguchi, 2018 [17]	Secondary Neutral Mass Spectroscopy	780	50
Srikanth, 1989 [16]	Activity measurements	690	67
Aalders, 1982 [84]	Cluster variation	723	50
Dey, 1968 [85]	Internal friction	753	50
Asta, 1995 [14]	EAM effective-pair-interaction study	900	67
Schüle, 1961	Resistivity, Hall coefficient	923	
Turchanin, 2007 [74]	CALPHAD	605	60
This study, 2022 [26]	Atom probe tomography	608	45

4.3 Detector efficiency

In this work, the detector efficiency of the used APT instrument is determined by measuring samples containing features of known dimensions. For the preparation of such a sample, similar to the thickness calibration, a planar SiO_2-substrate was coated with a multilayer stack of Cu and Ni, corresponding to ten layers of $Cu_{10nm}Ni_{10nm}$, and a protecting Cr layer on both sides of the stack serving as buffer and protection. Using the FIB lift-out technique, a lamella was cut out, rotated to 90° and glued on a W-post. This way the layer stacking is aligned perpendicular to the tip axis. After shaping to a tip, the sample was measured via METAP.

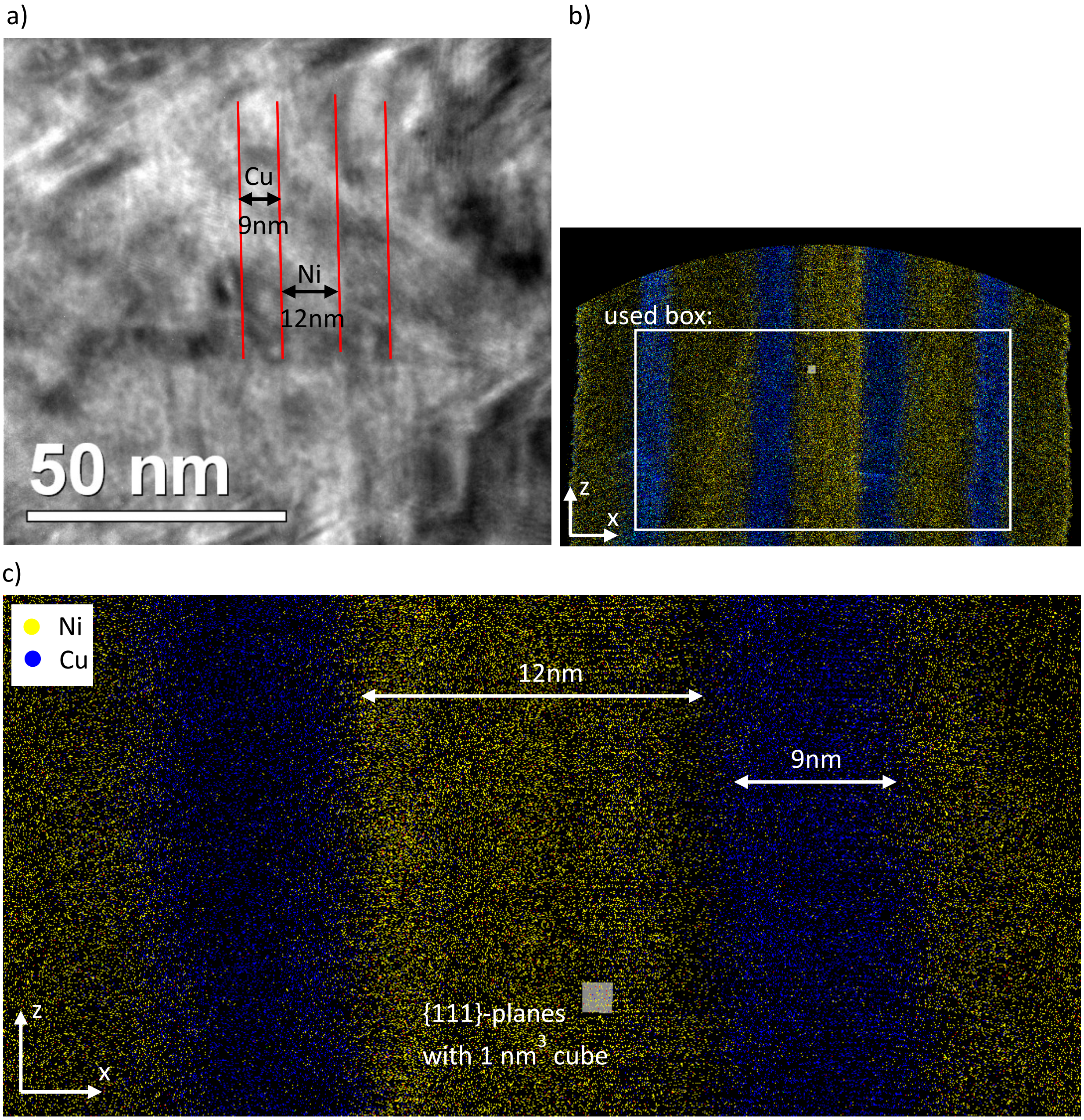

Figure 43: a) TEM lamella of the multilayer structure with marked layer interfaces (red). b) Cross section of the tip reconstruction with vertical lamellas. For the determination of p, the marked region is used (white box). c) Zoom in b) to show the lattice planes.

A second lamella, close to the first one was cut and thinned for investigations with TEM, to analyze the layer thicknesses. By that, the lateral scaling of the APT sample is determined. For the depth scaling, the distance between the resolved lattice planes was determined, which are known to be the {111}-planes as the closest-packed direction and will be preferred during deposition.

The results from TEM and APT reconstruction are shown in Figure 43. Assuming that the scaling in both lateral directions (x and y) is equivalent, a box containing all layers is placed in the rescaled reconstruction. Counting all atoms in this box, the atom number is determined and compared to the number of atoms that the box would theoretically contain.

The detector efficiency is received as:

$$p = \frac{N_{exp}}{N_{theo}} = 0.284 \pm 0.065$$

With $N_{exp} = N_{Cu} + N_{Ni} = 1352132 + 1377763 = 2729895$ and the corrected box dimensions $V = x \cdot y \cdot z = 72\text{ nm} \cdot 50.6\text{ nm} \cdot 30\text{ nm} = 109350\text{ nm}^3$.

The advantage of this procedure is, that lateral density fluctuations, caused by poles or zones axis, are also included. Especially, the density gradient being highest at the tip apex and getting radially lower, which is normal for APT tips, is considered. This is not the case for the SDM technique, which uses a small tip cross section (2x2 nm^2) where such gradient is not comprised.

4.4 Grain Boundary Segregation

For characterizing GB Segregation, homogeneous thin film alloys of four different CuNi concentrations were prepared. After an annealing treatment to be in thermodynamic equilibrium, Cu segregation into the grain boundaries was observed. In total, 20 tips with overall 70 segregated grain boundaries were evaluated.

To search for segregated grain boundaries in the samples volume, Cu isosurface maps were created from tip reconstructions to emphasize Cu-rich regions (Figure 44). Straight parts of the GB were than extracted by a box with dimensions of around 15x15x36 nm^3 (red). For an accurate evaluation, the fluctuations in atomic density caused by evaporation artefacts, have to be homogenized and the overall density needs to be corrected to the physical density first. Therefore, a density correction by short, simulated annealing was performed.

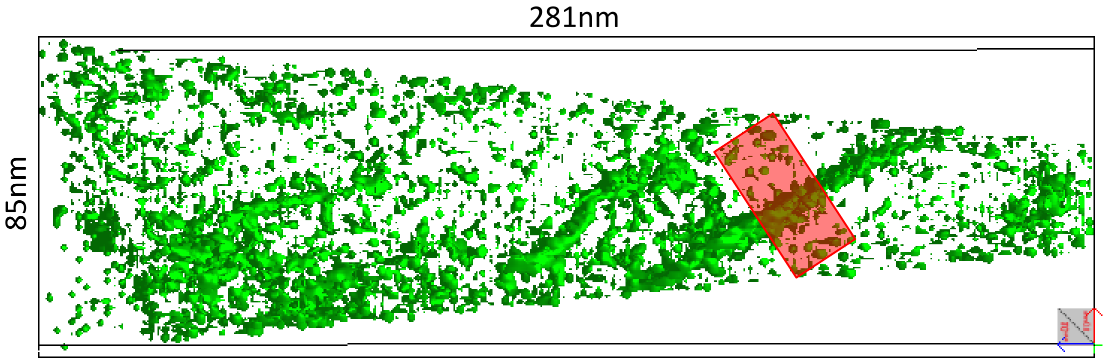

Figure 44: Cu-concentration isosurface of a reconstructed sample with c = 0.6 at an iso-value of 48%. The red rectangle represents the extraction box around the GB.

4.4.1 Density correction

The density correction was fulfilled via molecular dynamics (MD) by utilizing an interatomic embedded-atom potential from [8]. In a first step, the box volume was scaled down to fit with the theoretical density. Then, the interatomic distances were equilibrated by using a short MD run of of Δt = 100 fs at 300K. As a consequence of the density homogenization, the originally rectangular box will become deformed. Thus, the GB area is corrected and can be directly used for further evaluation of the solute excess. Although this procedure corrects the density deviations and equalizes it to the theoretical density, it doesn't reproduce the real sample density, since the measured density is reduced by the detector efficiency. This is considered by multiplying the result by p^{-1}. Note that the density correction has no influence on the possibly wrong positions of individual atoms caused by trajectory aberrations. These artefacts still can be found in the measurement. But with this correction, the calculation of the solute excess and the GB width of the segregation zone as statistical averages on many atoms are corrected.

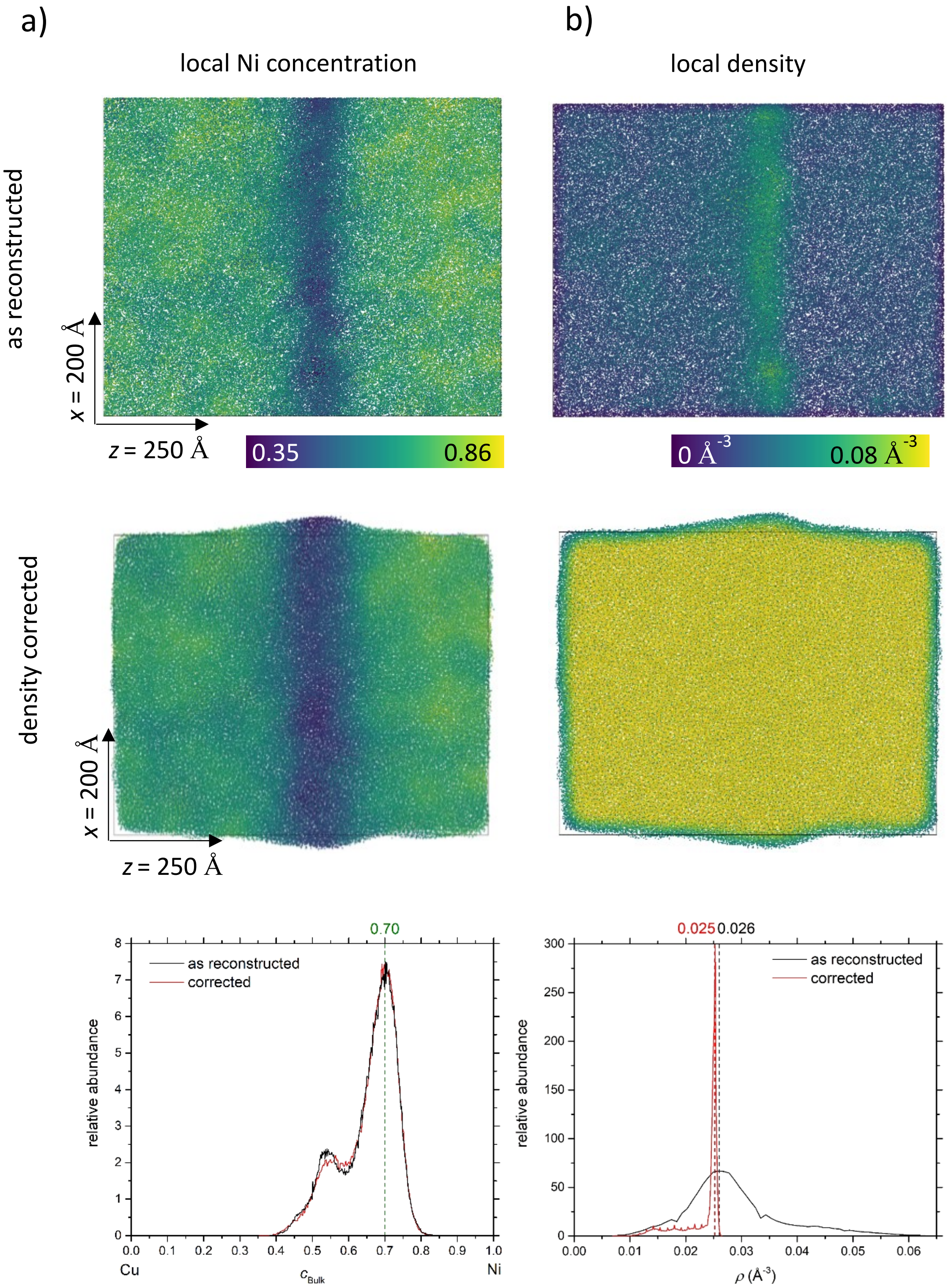

Figure 45: Influence of the density correction to a box containing a grain boundary shown as a local Ni concentration map (a) and a local density map (b). The top pictures show the as reconstructed box, the middle the box after correction and the bottom pictures the histograms.

The process of density correction is exemplified in Figure 45. For an as-reconstructed box (top images), huge inhomogeneities can be seen for concentration and density, which were maximal at the grain boundary. After density correction (center images), the perfect rectangular shape of the box is lost, and the GB region is laterally stretched. Now, the density is homogeneous and equal to the theoretical value (considering *p*), as can be seen from the local density histogram (bottom images). While the concentration histogram (Figure 45a, left bottom) shows nearly no change, the average (peak) density in the density histogram changes its shape drastically after correction and becomes very sharp. This is an indication for the reduction of density fluctuations and an overall homogeneity. However, a tiny plateau is observed for low densities from 0.01 to 0.024 Å^{-3}, corresponding to the density fluctuations at the box surface. A small difference to the theoretic density (calculated from the lattice constant parametrization according to [86]) is remaining, which can be attributed to the amorphous structure of the reconstructed samples, opposite to the crystalline one in the theoretic consideration.

4.4.2 Grain boundary evaluation

From the density corrected volumes, composition profiles across the GB (*z*-direction in Figure 46) were created with a binning size of Δz = 5 Å and fitted by Gaussians. Therefore, the volume was cropped to a rectangle with smooth surfaces. While the bulk concentration c_{bulk} and the segregation width *w* were directly received from the base line and the full-width-of-half-maximum (FWHM), the solute excess is received from Eq. (41), according to:

$$\Gamma = \frac{[N_{Ni}]}{A} = z\,\frac{N_{Ni,total} - N_{Ni,Bulk}}{V} = \int \Big(\big(c_{Ni} - c_{Ni,Bulk} \big) \rho \Big)\, dz, \qquad (41)$$

as the integral of the Gaussian amplitude and the base line, multiplied by the density. Where *V* is the volume, c_{Ni} the Ni atomic fraction and ρ the density. This procedure is shown in Figure 47 for the corrected GB from Figure 46. Note that the overall density (blue squares) is constant at the expected value of 0.85 Å^{-3} along the whole box length *z*.

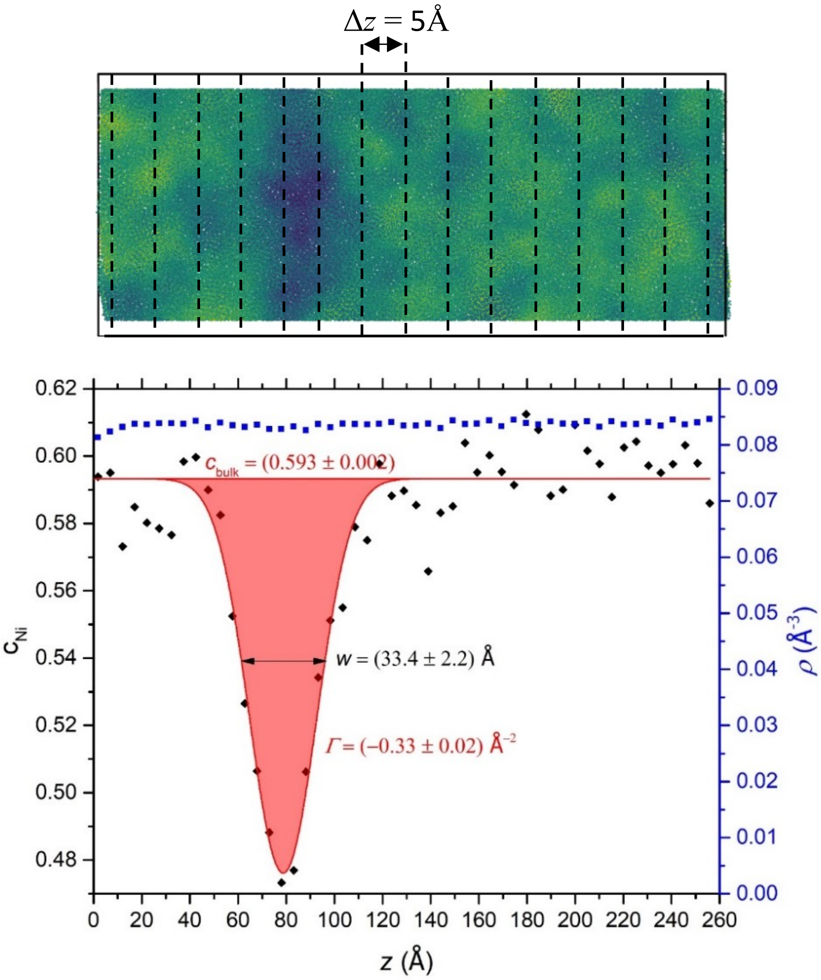

Figure 46: A density-corrected sample volume split into 5 Å slices (bins, top) for the determination of a composition profile (bottom, black diamonds) with the additional Gaussian fit (red line). The characteristic GB parameters are determined from the base line (c_{bulk}), the FWHM (w) and the amplitude area (shaded red). The corresponding density profile is shown by blue squares (right axis).

4.4.3 Grain boundary solute excess

GB segregation is expressed by the solute excess Γ, which is here defined as being negative, when Cu enrichment occurs. The calculated Γ for samples with nominal bulk concentrations of $c_{\mathrm{Ni}} = 0.25$, 0.6, 0.7 and 0.85 are shown in Figure 47 as black diamonds plotted versus the actually measured bulk concentrations. It can be seen that for low Ni concentrations up to $c_{\mathrm{bulk}} = 0.25$, the segregation is low, too, ranging from (0.046 ± 0.015) Å^{-2} to (0.27 ± 0.038) Å^{-2}, indicating a low segregation tendency. With increasing Ni content, *Γ* is increasing, showing values between (0.04 ± 0.015) Å^{-2} and (0.54 ± 0.022) Å^{-2} for $c_{\mathrm{bulk}} = 0.6$ at.% Ni. The highest segregation is reached at c_{bulk}

= 0.7 at.% Ni with excess values from (0.49 ± 0.046) Å^{-2} up to (1.28 ± 0.086) Å^{-2}. For even higher Ni concentrations with c_{bulk} = 0.85 at.% Ni, Γ is reduced again to values ranging from (0.018 ± 0.019) Å^{-2} to (0.86 ± 0.064) Å^{-2}, similar to c_{bulk} = 0.4 at.% Ni.

With this overall evaluation, a clear impression of the segregation trend as a function of the bulk concentration is obtained. However, only four different concentrations could be examined, and a knowledge of the continous concentration range is missing. Nevertheless, the trend of Γ over the whole c_{bulk} might be evaluated analytically, using the model function from Eq. (30). In this equation, w_{eff} was set to 14 Å, according to the findings in [9]. To define Q_{eff}, a polynomial approach was used according to:

$$Q_{eff}(c_{bulk}) = \sum_{i=0}^{N} \alpha_i c_{bulk}^{i}, \qquad (42)$$

with N as the polynomial order and α_i as free fitting parameters.

In order to apply the Langmuir-McLean isotherm ($Q_{eff} = \text{const}$), N is set to zero. The resulting plot is shown in Figure 47 as a blue line. Regarding the barycenter of the data points, reasonable agreement is received on the most Ni-rich side. Already at c_{bulk} = 0.6 at.% Ni, the fit becomes worse as only the two highest experimental points, are described by the fit. The same is true for the Cu-rich side, where the datapoint at c_{bulk} = 0.13 at.% Ni, doesn’t even fit at all. So, the McLean model is limited in the description of the excess through the whole range of concentration.

If, instead of being constant, Q_{eff} is described as a third-order polynomial ($N = 3$), the curve becomes in better agreement to the experimental data points for the whole concentration range, as shown by the red curve in Figure 47. The plot is similar to the Langmiir-McLean isotherm on the Ni-rich side. However, it has a stronger decrease at c_{bulk} = 0.6 at.% Ni, fitting better to the experimental values. Most important, this fit matches the very low excess at c_{bulk} = 0.13 at.% Ni, whereas the Langmuir-McLean isotherm does not.

Generally, the solute excesses of the fitted curves are low on the Cu-rich side and high on the Ni-rich side, with a peak values at c_{bulk} = 0.75, which is in accordance to the experimental values. However, the peak excesses are strictly decreased in comparison to the measurements.

With the better fit of the third-order polynomial, a concentration dependency of the segregation parameter Q_{eff} is demonstrated.

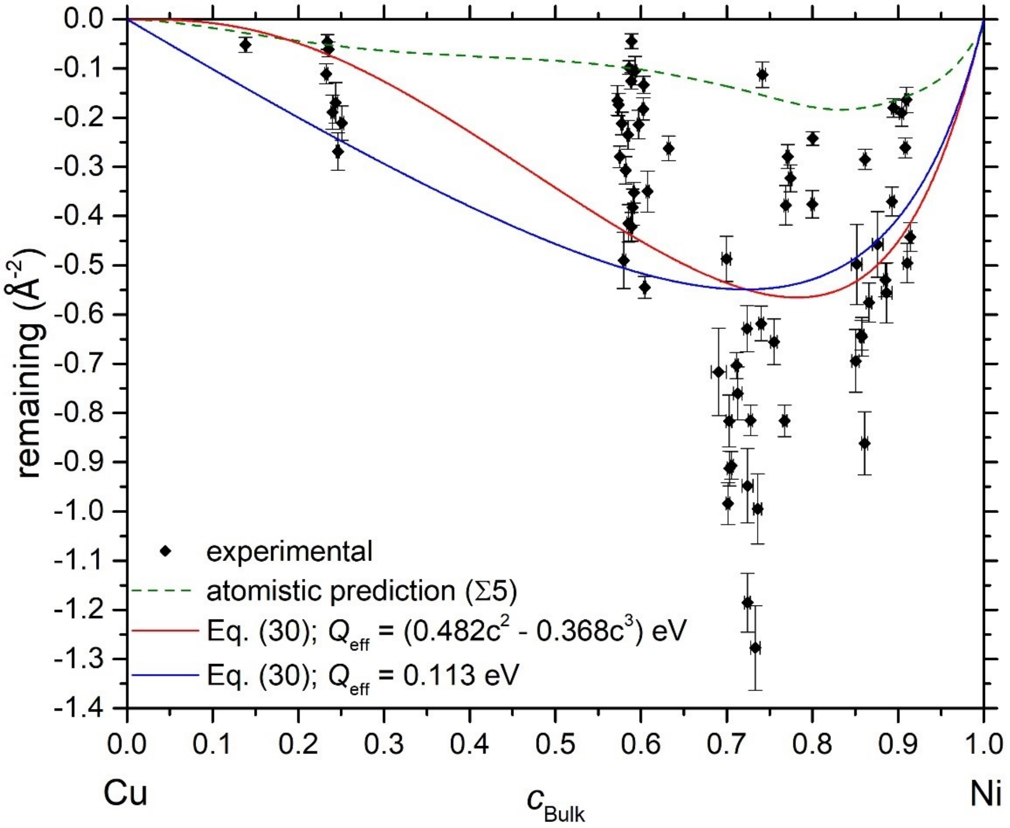

Figure 47: Experimental determined segregation excess Γ over the bulk concentration c_{bulk} (black diamonds) of 70 GBs. The blue and red line represent fits of Γ according to Eq. (30) with Q_{eff} being either constant (blue) or a polynomial of 3rd order (red). The green dashed line is a fit of Γ from a simulated Σ5 GB taken from [9].

In $Q_{eff} = \text{const}\ (N = 0)$, the constant line is optimized at $Q_{eff} = 0.113\ \text{eV}$, assuming equal segregation tendency over the whole concentration range. In contrast, for $N = 3$ the segregation enthalpy is zero for c_{bulk} = 0 and increases steeply to a maximum of 0.122 eV for c_{bulk} = 0.87 at.% Ni. Then, it reduces to 0.113 for c_{bulk} = 1. This shape shows that there is no segregation tendency on the Cu-rich side, whereas a strong segregation tendency is observed on the Ni-rich side, being highest at c_{bulk} = 0.85 at.% Ni. This is in accordance to Figure 47, where the solute excess behaves in the same manner with respect to the bulk concentration. Just the peak concentration slightly vary, lying at c_{bulk} = 0.75 at.% Ni.

Recently, a segregation study on a simulated, ideal Σ5 GB was made by Fischer et al. [9]. Their results are plotted in Figure 47 as green dashed line. In comparison to the experimental data, this atomistic prediction shows the same trend with varying bulk concentration, however, the absolute values are just half as big as the experimentally observed excesses. Also the peak excess is predicted at a slightly higher concentration of c_{bulk} = 0.85. This discrepancy might come from the specific GB structure used for the theoretical investigations. While the experimental GBs are naturally occurring, representing a statistical average related to the deposition texture, the simulated GB has been a selected, ideal CSL Σ5 GB. Natural GBs frequently show no ideal CSL configurations but random orientations, caused by the random grain structure evolving during the deposition process, meaning that they are generally higher in energy. By high solute segregation, even high-energetic configurations can be stabilized, preventing changes in the GB structure. Furthermore, defects like vacancies, impurities and dislocations tend to accumulate at the GBs, since they act as natural sinks. These defects are also increasing the system's total energy but can be reduced when localized at the GB region. Another important aspect of the natural GBs is that they typically don't consist of pure tilt or pure twist components but are of mixed character. By mixing these fundamental components, an energy saving GB constellation with less structural displacement can be likely achieved. All these deviations from the ideal configuration may explain an increase of the GB formation energy and thus, a higher solute segregation as in the experimental data demonstrated [87, 35].

Another experimental study about GB segregation in CuNi alloys was made by Pellicier et al. [88], intended analyze the thermal stability of nanocrystalline Ni. They found that the thermal stability increases by alloying with Cu, which is due to GB segregation. For their experiments they coated silicon substrates with thin films of CuNi of 3 μm thickness by electrodeposition and annealed them for 3 h at 625 K in a UHV furnace to induce segregation. From TEM analysis, they obtained an excess of approximately 1 Å^{-2} for a Ni content of 56 at.%, which is higher than found in our experiments but in the same range. The remaining discrepancy is probably due to the lower annealing temperature since the excess generally increases with decreasing annealing temperature.

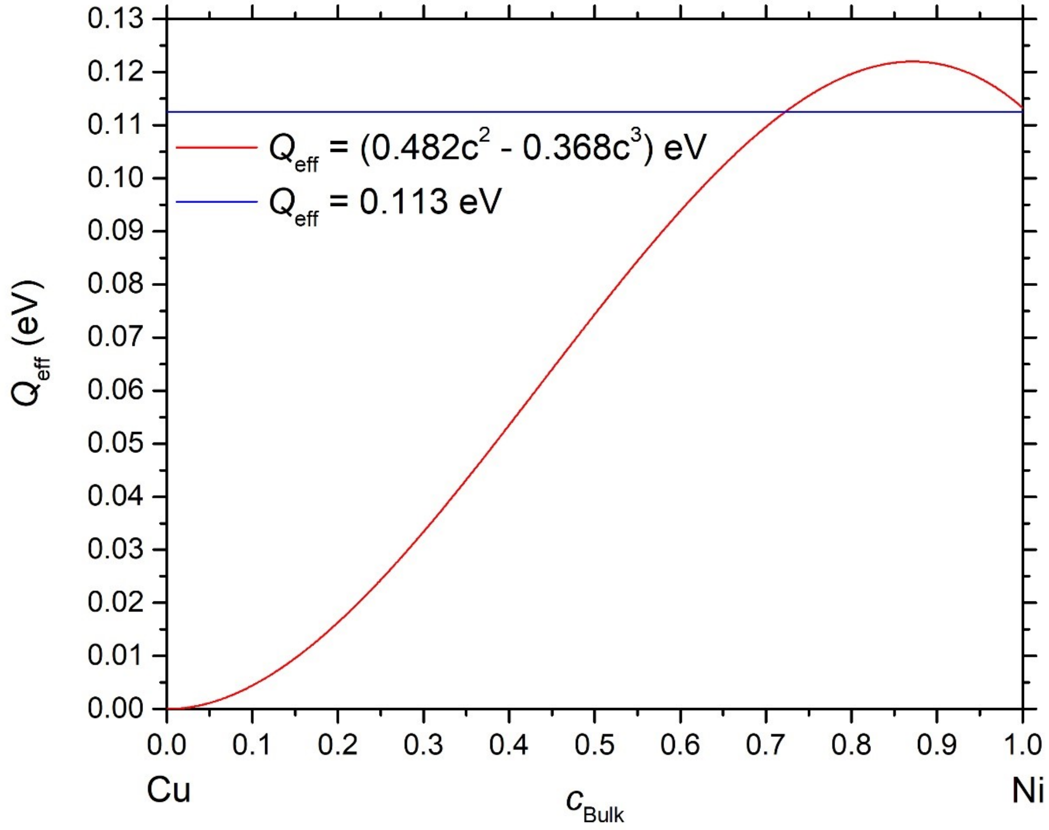

Figure 48: The effective segregation parameter Q_{eff} as a constant (blue) and polynomial (red) function of the bulk concentration.

4.4.4 GB formation energy

With the excess curves calculated in Figure 47, the change in the GB formation energy, $\Delta\gamma$, due to segregation can be determined, using the integral of Eq. (26). Therefore, $\Delta\gamma$ was plotted as a function of the Ni concentration. For the calculation, $\frac{\partial^2 \mathrm{g}}{\partial c^2}$ must be defined. The results of different Gibbs free energy parametrizations are presented in Figure 49. The latest CALPHAD parametrization from Turchanin et al. [74] is shown as a blue line. At low bulk concentrations until c_{bulk} = 70 at.% Ni, a relatively flat trend is observed with a small linear increase to energy values of nearly 0.1 J m^{-2}. Afterwards, the slope becomes steep and the curve intercepts with the y-axis for pure Ni at a maximum energy of $\Delta\gamma$ = 0.81 J m^{-2}. A new Gibbs free energy parametrization was proposed in this study based on APT measurements of the miscibility gap, using the Redlich-Kister polynomial, according to Eq. (13) [26]. Its $\Delta\gamma$-curve is shown as red line in Figure 49 and its trend is similar to the CALPHAD parametrization. However, it's even more pronounced with a higher maximum of $\Delta\gamma$ = 1.03 J m^{-2}. Both curves demonstrate a pronounced increase of GB energy on the Ni-rich side, which is in accordance with the higher excess for high Ni concentrations shown in Figure 49.

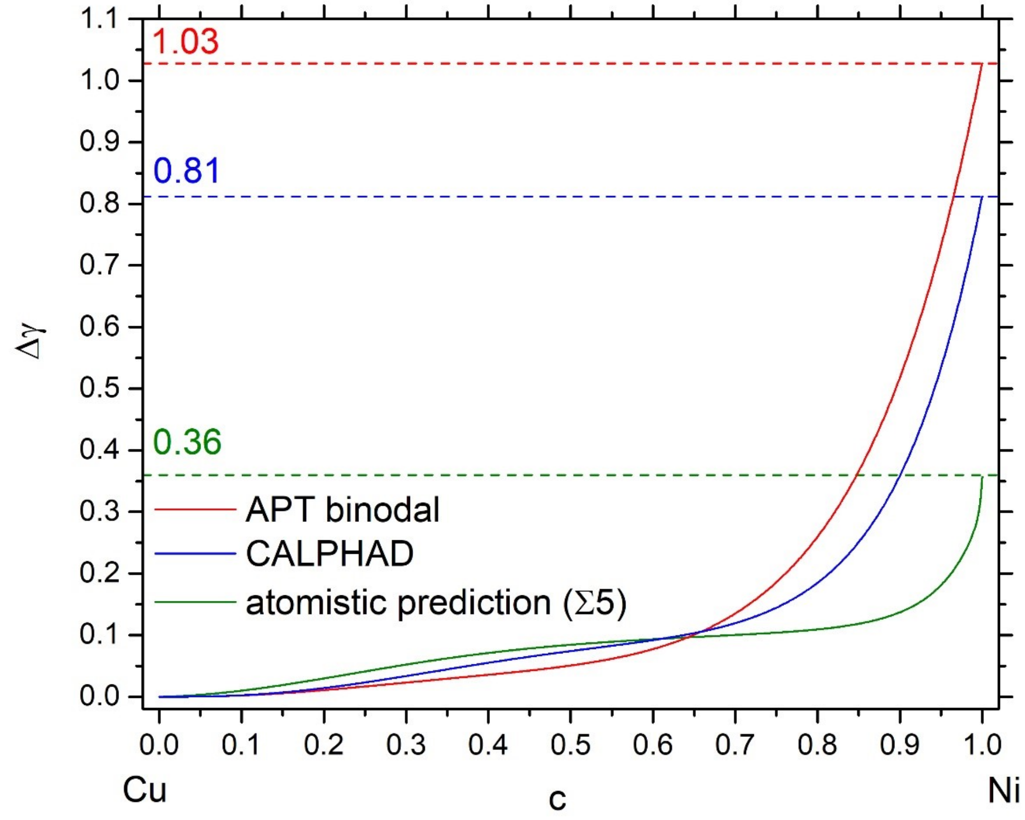

Figure 49: Change in the GB formation energy $\Delta\gamma$ for T = 700 K, calculated with Eq. (). For the Gibbs free energy g(c) the latest CALPHAD parametrization [74](blue) and a parametrization from an APT study of the binodal [26](red) was used. The green line represents $\Delta\gamma$ of a simulated $\Sigma 5$ GB (atomistic prediction) [9]

The Δ*γ*-curve of the atomistic prediction is shown as a green line in Figure 49. In comparison to the experimental parametrizations, this curve shows slightly higher energies in the low concentration regime, which stays constant for a concentration up to c_{bulk} = 0.9 with a sharp increase to a lower maximum of 0.36 J m^{-2} observed at c_{bulk} = 1.

The change in the GB formation energy is a measure of the excess multiplied by the second derivative of the Gibbs free energy. A pronounced difference between the excess curve of the atomistic prediction and the fitted experimental curves in Figure 50 shows, that there is a huge difference in the absolute excesses. This huge difference is not visible in the Δ*γ*-curves. Instead, the curves are very similar, just a small deviation can be seen.

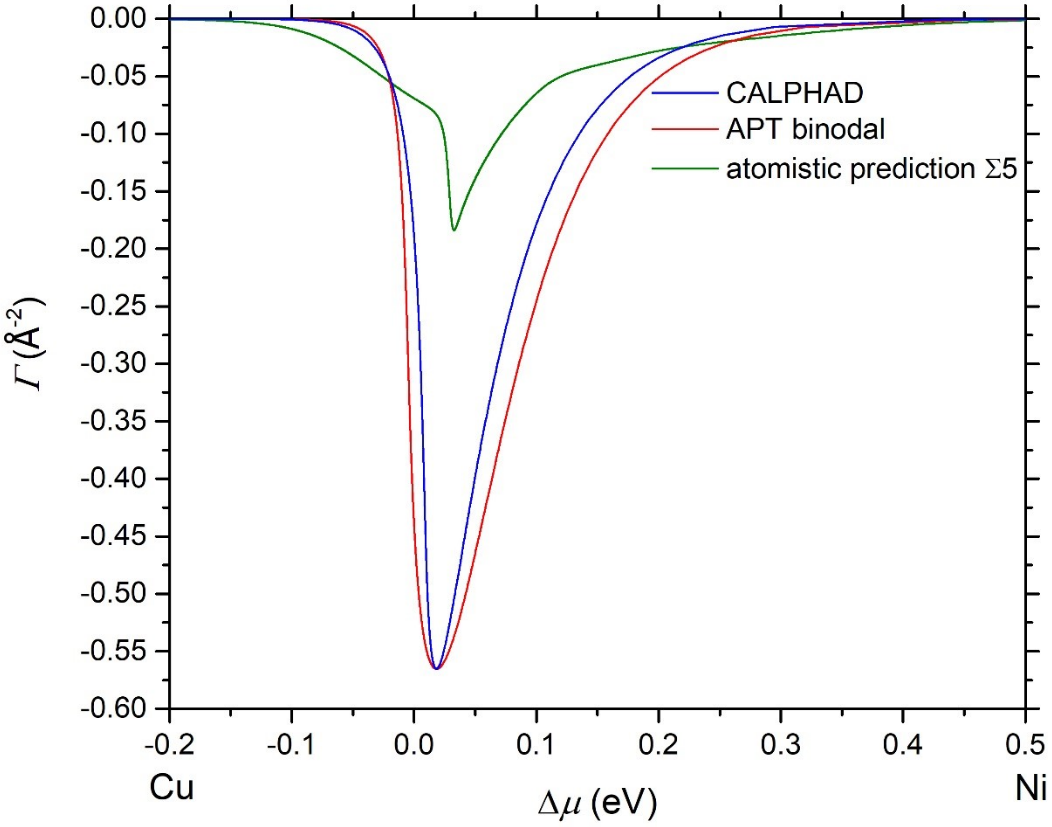

Figure 50: Plot of the Γ-values received from the polynomial fit in Fig.32 against the chemical potential difference Δμ. Δμ is received from the second derivative of the Gibbs energy parametrization according to Redlich-Kister [73] from Turchanin et al. (purple) and from the recent experimental data for the miscibility gap measured in this project. In comparison, the Γ versus Δμ plot from Fischer et al. is shown (green).

The atomistic prediction in [8] was tested for experimental and ab initio data of surface energies ($\Delta\gamma(c = 1)$), where $\Delta\gamma$ was reproduced well to theoretical values. This means for pure Ni, so for c = 1, $\Delta\gamma$ is quite accurate. Therefore, the deviation at $\Delta\gamma(c = 1)$ might come from the experimental excess values, which are high due to the non-ideal GB orientations, as discussed in the previous section. Additionally, the CALPHAD parametrization, necessary for evaluating the curvature of the Gibbs free energy, can contain uncertainties, leading to higher energies. Although care is taken to use only reliable experimental and theoretical parameters, some parameters are not easily accessible and therefore still inaccurate. Especially the solid mixing properties arise from theoretical or indirect experiments and might lead to errors.

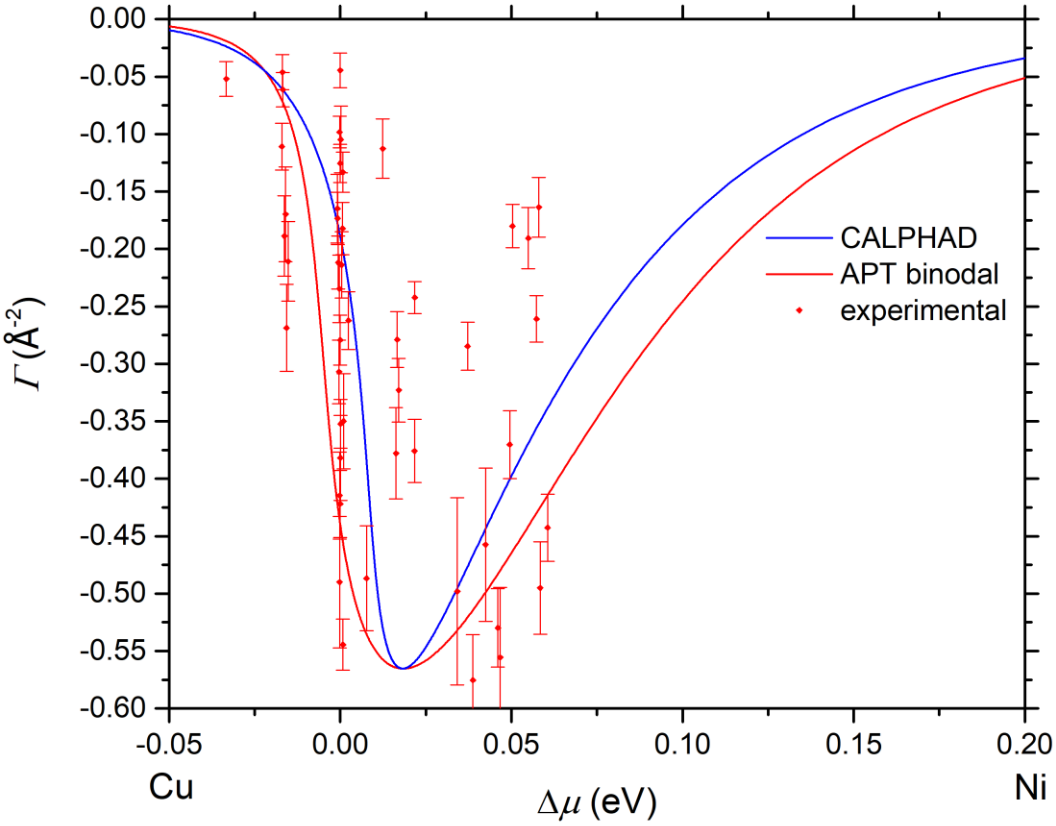

Figure 51: An extract from the plot of Γ against $\Delta\mu$ (Figure 50) with the experimental measured data points included.

For further analysis of the discrepancies between experimental data and simulated prediction, the excess is directly plotted against the chemical potential difference $\Delta\mu$, as shown in Figure 50 for all three curves in Figure 49 using identical colors. Similar trends are observed for both experimental Γ-curves with parametrizations according to CALPHAD and the present APT studies of the binodal, showing huge solid segregation around $\Delta\mu$ = 0.02 eV while the excess in the simulated GB is way lower. Figure 51 shows an extract of this plot, with the experimental data included. Herein, the chemical potential is calculated from the new Gibbs energy parametrization derived in this work. While the data points are fitting accurately with the fit curves on the left side of the functions peak value, the values on the right side have a sharper increase of excess values than in the fits, meaning the curve integral of the experimental values is actually smaller. This shows that the fit curves are just barely describing the experimental data for $\Delta\mu$ > 0.05 eV and the experimental trend of the $\Gamma/\Delta\mu$-curve is narrower. The erroneous larger area in Figure 51 is also the reason for the larger GB formation energy in Figure 49, since the fit curves were used for its calculation.

In the plots above, the recent experimental findings were compared to the atomistic prediction, which are barely fitting. Considering, that the interatomic potential, which is necessary for the simulation of the GB, was only adapted for properties of the pure material, the accuracy of the atomistic prediction for concentration resolved GB formation energy changes is less, as it is obvious from Figure 50. Additionally, the dependence of the chemical potential difference $\Delta\mu(c)$ on bulk composition might be erroneous, since here a parametrization is involved, which is directly contributing to Figure 49. Despite these complications, the experimental results still can be compared to the atomistic predictions both showing convincing agreement in the overall trend. The theoretical model may be further improved, when the recent experimental findings of GB segregation would be introduced into the determination of the embedded atom potentials used for the atomistic simulation.

4.4.5 Segregation width

From the GB composition profiles shown in Figure 46, the segregation widths were determined as the FWHM. The widths range from 12 to 85 $\mathrm{\AA}$ with a scatter range between 1.5 and 14 $\mathrm{\AA}$, as plotted in Figure 52 for all measured GBs. In comparison to the structural GB widths, which lie between 5 and 10 Å [89, 90], the segregation widths measured in this project are several times larger. Nevertheless, the results are in accordance with similar APT analysis of GBs [91, 92, 93, 94].

An explanation of this huge discrepancy might be the trajectory overlap of the evaporating atoms during APT analysis, which is also mentioned in section 3.6.3. Caused by compositional differences at the GB, stemming from Cu segregation, a faster evaporation of GB atoms leads to a grooving at the GB surface. Based on the chemical composition, this grooving has different dimensions, deflecting the trajectories of the evaporated ions to hit the detector either at the GB center or at the facing sites of the GB. The latter causes a mixing of the GB atoms with the matrix atoms and leads to a significant GB broadening. This procedure was also predicted by Oberdorfer et al. [95] in simulated evaporation of GBs with low evaporation fields (which is the case for Cu segregated GBs in the Cu-Ni-system). The artificial mixing of GB and matrix atoms reduces the maximum concentration at the GB center and increases the FWHM.

In Figure 52, the segregation widths, *w,* were plotted against their respective solute excesses, *Γ*, and were color-coded with respect to their bulk concentrations. In this way a remarkable correlation becomes obvious which may even be understood as linear relation. For each concentration, an increase of the width with increasing (absolute) excess is observed, as indicated by their linear regression lines (solid lines of the same color). The slopes of these lines vary with the concentration and are highest for the lowest Ni concentration of 25 at.% (magenta). With increasing Ni content to 60 at.% (blue), the slope of the regression line decreases and becomes minimal for a content of 70 at.% Ni (cyan). However, this trend doesn't fit for a bulk concentration of 85 at.%, where the slope increases again.

Although the structural GB width does not change, the segregation width is tendentially increasing with increasing Excess. This is clearly visible from the plot in Figure 52. A GB width of up to 85 Å is theoretically hardly understood and must be a result of the described trajectory overlaps, which artificially broaden the GB by mixing bulk and GB atoms. However, an increase of the chemical width to this value could not be proven by simulations. According to Figure 52, it seems to be affected by the bulk concentration and is stronger for higher Cu contents, which is obvious from the large slope for c_{Ni} = 25 at.%.

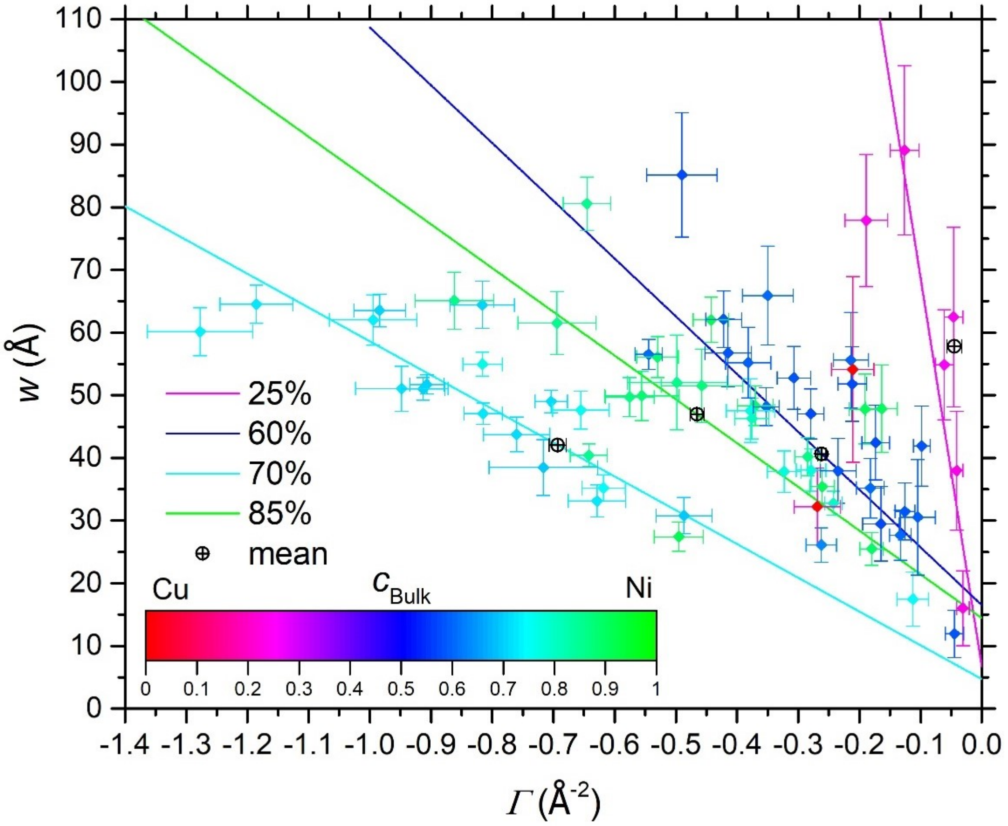

Figure 52: Experimentally determined GB widths w as a function of the solute excess Γ. The data points are color-coded according to the bulk concentration. The colored lines are the linear fits from each concentration range with the equivalent color.

Although the slopes in Figure 52 vary in dependence of the bulk concentration, their intercept with the y-axis at zero excess is similar for all of them. This value is averaged to w_0 = (10.1 ± 1.5) Å. If the GB widths were artificially broadened by trajectory crossovers, this measurement artefact will be more pronounced, the higher the amount of segregated atoms, so, the higher the solute excess. Consequently, trajectory aberrations can be neglected if the segregation is zero, which is the case for the y-interception point. This means, w_0 defines the structural width of the GB which is in convincing agreement to the literature data [89, 90, 96].

Calculating the mean excess value for each concentration and comparing their GB widths (black circles in Figure 52), it is seen that they are very similar, having an average of around 47 Å. The GB widths at c=25 at.% have the highest deviation, being w = 57.8 Å on average. However, for this bulk concentration the errors are also the highest and the measurement points the fewest.

4.5 Grain Boundary Orientation

With the APT measurements, the solute segregation of each GB could be characterized. To investigate its dependency on the GB orientation, tEBSD measurements were performed previously to the APT analysis of the c_{bulk} = 0.6 at.% Ni tips, to create orientation maps (OIM) of the grain structure of the tips, similar to the approach from Babinsky et al. [13]. In [13], the EBSD–assisted FIB milling of APT tips was introduced to increase the probability of finding GBs in the measurement. However, combining the grain orientation received from the tEBSD and the GB plane normal orientation, which is determined from the APT reconstruction, all five degrees of freedom are given to define the complete GB orientation. In both analysis techniques, the orientation is defined with respect to the sample alignment towards the detector, acting as a reference system. For correct correlation, both reference systems must be brought into accordance with each other. Therefore, the reconstruction of the APT-measured tip is rotated around the length axis (x-axis) to fit with the orientation map of the tip, received from the EBSD analysis. By applying a coordinate transformation to the reference system of the reconstruction, and by considering the rotation angle to correlate both tip images, the coordinate system of the reconstruction is transferred to the one from the EBSD analysis. By that, the GB plane normal, stemming from the reconstruction, can be expressed over the orientation of the adjacent grains. The exact procedure is explained in the following section.

4.5.1 Determination of the GB plane normal

For the determination of the GB plane normal, first, the reference coordinate system of the reconstruction space is defined. According to the yaw, pitch and roll rotations, which stand for the rotation angles around the z, y and x axis, the coordinate axes were determined as shown in

Figure 53, with the x-axis as the blue, the y-axis as the red and the z-axis as the green direction, resulting in a left-handed coordinate system. To calculate the GB plane normal, a rectangular box with a direction vector of $\vec{e}_x = \begin{pmatrix} 1 \\ 0 \\ 0 \end{pmatrix}$ was placed normal to the GB plane (see Figure 44). This box is orthogonal to the GB plane, representing the normal vector. Its orientation is given by rotation matrices around each coordinate axis by the rotation angles yaw (Ψ), pitch (θ) and roll (ρ). Note that the rotation in the reconstruction software is described by intrinsic Cardan angles and the order of rotation is not commutable. The resulting transformation matrix is a product of all three rotation matrices in the following order:

$$
\begin{aligned}
R &= R_z(\psi)R_y(\theta)\big(R_x(\rho)\big) \\
&= \begin{pmatrix} cos\psi & -sin\psi & 0 \\ sin\psi & cos\psi & 0 \\ 0 & 0 & 1 \end{pmatrix} \begin{pmatrix} cos\theta & 0 & sin\theta \\ 0 & 1 & 0 \\ -sin\theta & 0 & cos\theta \end{pmatrix} \begin{pmatrix} 1 & 0 & 0 \\ 0 & cos\rho & -sin\rho \\ 0 & sin\rho & cos\rho \end{pmatrix} \qquad (43)
\end{aligned}
$$

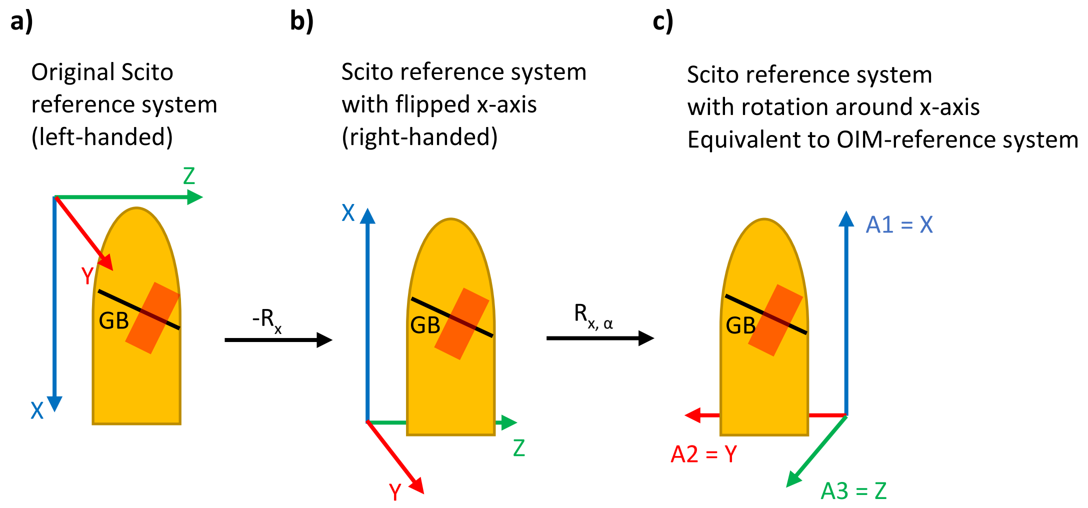

Figure 53: Schematic illustration of the coordinate transformation of the reconstructed reference system. a) shows the original reference coordinate system used by the reconstruction software Scito. In b), the x-axis is flipped to receive a right-handed coordinate system. Finally, the Scito coordinate system was brought into accordance with the one of the OIM-analysis software used for the tEBSD measurements by rotation around the x-axis with an angle α that brings the views in both techniques into equivalence.

By multiplying this transformation matrix with $\vec{e}_x$, the GB plane normal is calculated. However, Eq. (43) holds for right-handed coordinate systems. To transfer the left-handed coordinate system from Figure 53 into a right-handed, the term $R_x(\rho)$ was multiplied by -1, to switch the direction of the x-axis to the opposite. With that, the GB normal plane $\vec{n}_{Scito}$ is calculated as:

$$\vec{n}_{Scito} = R \cdot \vec{e}_x = R_z(\psi)R_y(\theta)\big(-R_x(\rho)\big) \cdot \vec{e}_x$$

$$= \begin{pmatrix} cos\psi & -sin\psi & 0 \\ sin\psi & cos\psi & 0 \\ 0 & 0 & 1 \end{pmatrix} \begin{pmatrix} cos\theta & 0 & sin\theta \\ 0 & 1 & 0 \\ -sin\theta & 0 & cos\theta \end{pmatrix} \begin{pmatrix} -1 & 0 & 0 \\ 0 & -cos\rho & sin\rho \\ 0 & -sin\rho & -cos\rho \end{pmatrix} \begin{pmatrix} 1 \\ 0 \\ 0 \end{pmatrix}$$

$$= -\begin{pmatrix} cos\psi cos\theta \\ sin\psi cos\theta \\ -sin\theta \end{pmatrix}. \tag{44}$$

4.5.2 Correlation between atom probe and tEBSD

$\vec{n}_{Scito}$ defines the GB plane normal in the reconstruction coordinate system. The next step is to express the GB plane normal in the tEBSD reference system. Therefore, the coordinate system in the reconstruction is rotated around the x-axis with an angle α, until the tip image seen in the reconstruction matches with the two-dimensional view seen in the OIM-analysis. With this, the coordinate transformation of the reconstruction reference system to the one from the EBSD-software is fulfilled (see Figure 54).

The coordinate system of the OIM-software is defined over the sample geometry with an Axis 1 (A1), showing downwards the sample, an Axis 2 (A2) pointing to the right, as viewed from the EBSD detector and an Axis 3 (A3), normal to the sample surface, as demonstrated in Figure 55a) for a general rectangular sample when analyzed by standard EBSD. For tEBSD, however, not just the sample is rotated oppositely, but also the surface, emitting the detected electrons is different. Using the same coordinate system would mean, that the sample surface normal is directed towards the electron gun and not the EBSD detector anymore (A3 in Figure 55b). At this surface, the electron beam enters the sample indeed, but the detected electrons were radiated from the opposite surface. Therefore, the analysis software automatically flips the sample coordinates system as shown in Figure 55b for calculating the orientation correctly.

Note that the microscopy image created by the SEM is not affected by this coordinate transformation since it has its own reference system with the y-axis directed upwards and hence, the x-axis showing opposite to A2 (see Figure 55a). However, this is considered in the analysis software automatically by a 180°-rotation around the A3 axis. Additionally, the sample tilt of 52° to the electron gun is corrected, so that if a tip sample is measured, the tip length axis is A1 and the lateral direction is A2.

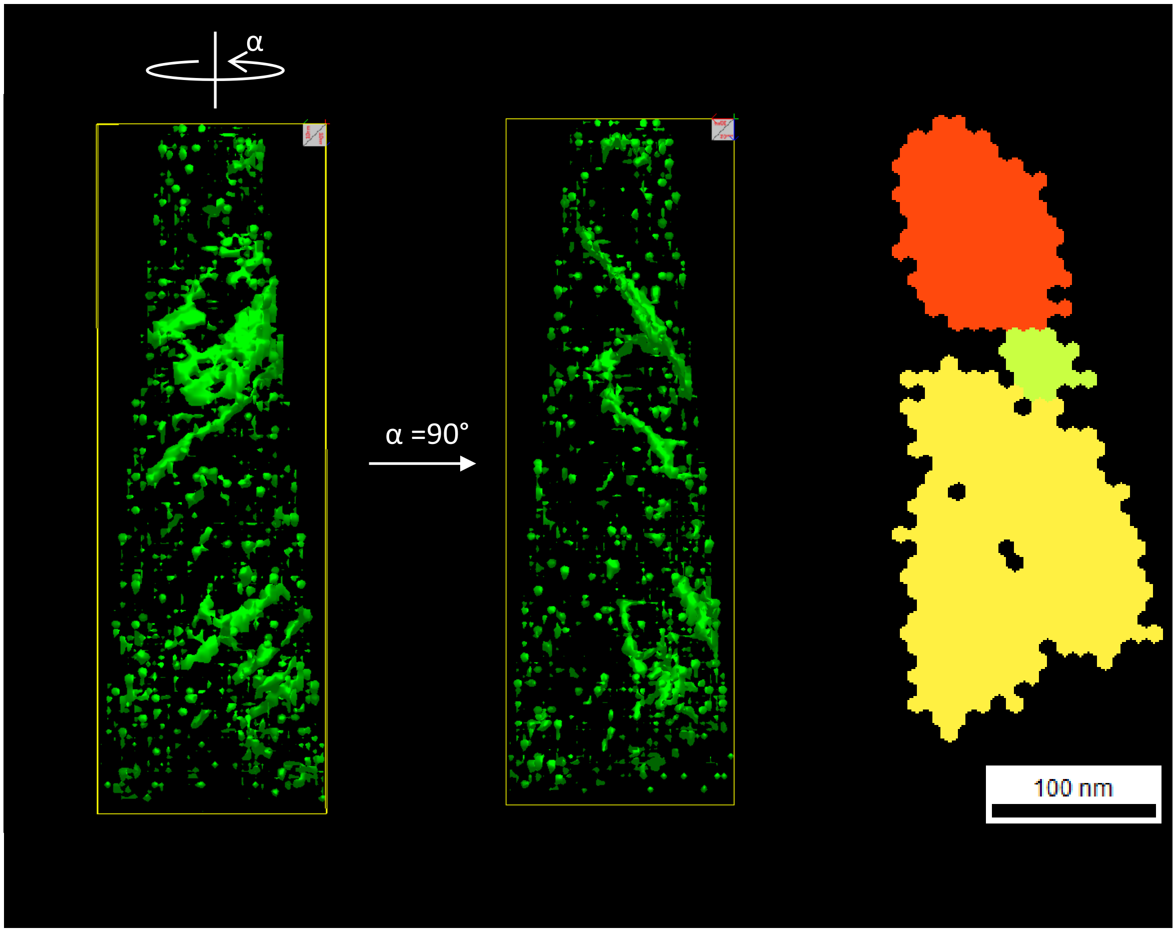

Figure 54: Correlation between reconstruction and orientation maps by rotation around the tip axis

With the information about the grain orientation from the tEBSD and the correlated coordinate systems of EBSD and reconstruction, the GB plane normal can be expressed in terms of the adjacent grain orientations by:

$$\vec{n}_G = G_{1,2} * \vec{n}_{Scito} \tag{45}$$

With $G_{1,2}$ as the orientation matrices of the both adjacent grains and $\vec{n}_G$ as the GB plane normal expressed by grain coordinates.

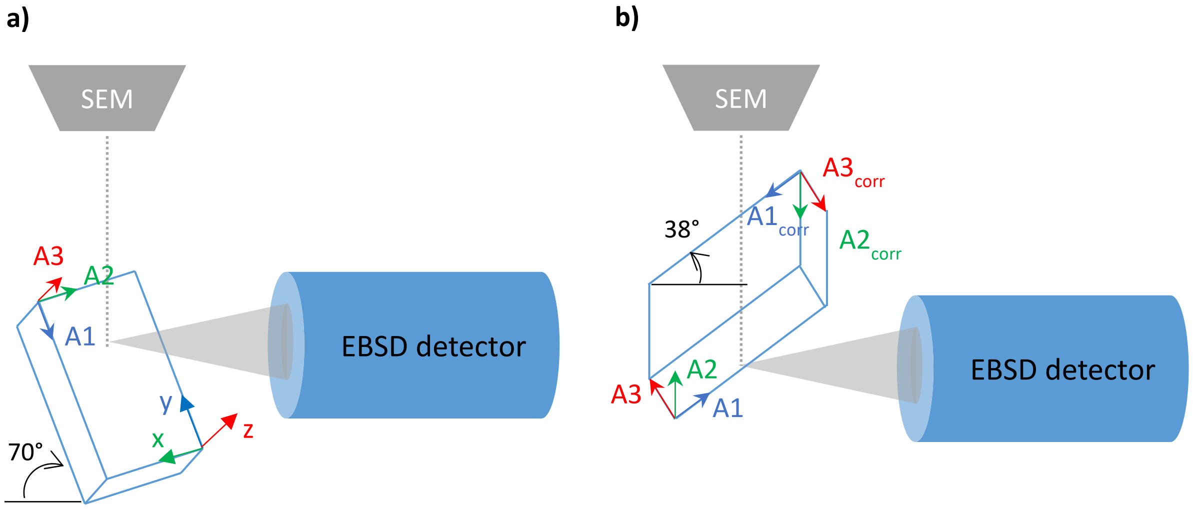

Figure 55: Definition of the coordinate system (A1, A2, A3) in the OIM software over the sample geometry in relation to the EBSD detector for classical EBSD analysis (a) and for tEBSD (b). For tEBSD, the coordinate axis is automatically flipped by the software, so that A3 is directed towards the detector.

4.5.3 Calculation of tilt and twist boundary contribution

From tEBSD measurements, a misorientation angle, θ, is determined, representing the smallest rotation around a misorientation axis, *m*, that brings both grains into coincidence (also called disorientation). This misorientation angle consists of a tilt and a twist GB contribution. With the knowledge of the misorientation (axis and angle) and the GB plane normal, their relative amount can be calculated. For the tilt contribution, the GB plane normal is determined for both adjacent grains coordinates, $\vec{n}_{G1}$and $\vec{n}_{G2}$, but expressed in just one system (either from the grain1 or grain2), by using a misorientation matrix R_m (Eq.(47)) and multiplying it with the GB plane normal

$\vec{n}_G$ according to Eq.(48). Since the rotation axis of a tilt GB is orthogonal to both GB plane normals, the tilt axis, $\vec{n}_t$, can be calculated over a vector product and the tilt angle, ψ, over a scalar product, according to Eq.(49) and Eq.(50).

$$R_m(\theta) = \tag{47}$$

$$\begin{pmatrix} {m_x}^2(1-cos\theta)+cos\theta & m_x m_y(1-cos\theta)-m_z sin\theta & m_x m_z(1-cos\theta)+m_y sin\theta \\ m_y m_x(1-cos\theta)+m_z sin\theta & {m_y}^2(1-cos\theta)+cos\theta & m_y m_z(1-cos\theta)-m_1 sin\theta \\ m_z m_x(1-cos\theta)-m_y sin\theta & m_z m_y(1-cos\theta)-m_x sin\theta & {m_z}^2(1-cos\theta)+cos\theta \end{pmatrix}$$

$$\vec{n}_{G2} = R_m(\theta)\cdot\vec{n}_{G1} \tag{48}$$

$$\vec{n}_{ti} = \frac{\vec{n}_{G1}\times\vec{n}_{G2}}{|\vec{n}_{G1}||\vec{n}_{G2}|} \tag{49}$$

$$\psi = arccos\left(\frac{\vec{n}_{G1}\cdot\vec{n}_{G2}}{|\vec{n}_{G1}||\vec{n}_{G2}|}\right). \tag{50}$$

Knowing, the misorientation consist of a tilt and a twist component, the twist contribution can be determined by matrix division of the misorientation matrix by the tilt rotation matrix (or by multiplying with the inverse matrix) according to Eq. (51):

$$R_m(\theta) = R_{\vec{n}_{ti}}(\psi)\cdot R_{\vec{n}_{tw}}(\phi) \tag{51.1}$$

$$R_{\vec{n}_{tw}}(\phi) = R_m(\theta)\cdot R_{\vec{n}_{ti}}(\psi)^{-1}. \tag{51.2}$$

From the received twist rotation matrix, the twist angle is received by:

$$\phi = \arccos\left(\frac{tr\left(R_{\vec{n}_{tw}}(\phi)\right)-1}{2}\right), \tag{52}$$

where $tr\left(R_{\vec{n}_{tw}}(\phi)\right)$ describes the trace of the matrix. Since the twist axis is parallel to the GB plane normal, its $\vec{n}_{tw} = \vec{n}_G$.

4.5.4 GB segregation: Dependency on the misorientation angle

Considering that the number of possible GB structures is practically infinite, and the measured GBs are all naturally formed, all of them should have different misorientation angle and axis, tilt and twist contribution, CSL and GB plane normal. To investigate the GB segregation dependency on the orientation, these properties were compared for each GB.

Also, the relationship between the GB energy and misorientation angle was indirectly investigated in this project, as shown in Figure 56. Since the change of GB energy is proportional to the GB segregation, the solute excess was plotted against the misorientation angle for all measurements, as received from the OIM analysis software. Another piece of information, which can be directly extracted from the software, is the CSL structure of the GB. Herein, the measured misorientation angles and axis are compared to a data table containing this information for all special GBs. However, care must be taken with this data since the rotation angle in the table and the misorientation angle are not always describing the same. For example, a twin GB has a CSL of $\Sigma 3$ and can be created either by a pure twist rotation of 60° around the {111} axis, or by a pure tilt rotation of 70.4° around the {110} axis. Since the OIM software is not able to calculate the tilt and twist contribution, it will only compare the value of the misorientation angle. However, if the misorientation angle of the GB matches with one of these values, but has a mixed character, the requirement for a $\Sigma 3$ GB is not fulfilled and the GB is wrongly declared to be $\Sigma 3$.

The GBs found in our experiments are mainly random and marked as black squares in Figure 56. Additionally, some $\Sigma 3$ GBs were found as special GBs, which are marked as blue squares. The LAGBs, also known as $\Sigma 1$ GBs due to low misorientation (single grains containing dislocations) are shown as red squares.

Comparing the results in Figure 56, it is seen that the solute excesses of the $\Sigma 1$ GBs range between -0.18 ± 0.02 and -0.38 ± 0.04 Å^{-2} which is in the same order of magnitude as the Γ of the remaining GBs. So, a reduced segregation for LAGB is not observed. The highest spreading is received for the $\Sigma 3$ GBs with Γ-values ranging from -0.10 ± 0.01 and -0.54 ± 0.02 Å^{-2}. The values for the random GBs are in-between.

Although it was expected that the GB solute excess of $\Sigma 1$ GBs is reduced in comparison to HAGBs, this could not be confirmed by the recent measurements. However, the found LAGBs have angles ranging from 9 to 15° and are therefore close to the limit for being HAGBs. GBs with lower misorientation angles were not found, probably due to the low segregation which made an identification with the atom probe difficult. Except of one GB, all GBs with a misorientation close to 60° are Σ3-GBs (having a ⟨ 111 ⟩-misorientation axis). Although the solute excess of these GBs have a huge spreading with excesses, even higher than for HAGBs, a gap between high and low Γ-values demonstrates that the Σ3-GBs can be either high- or low-energetic. Since they all have the same misorientation angle and axis, other properties must be responsible for the increased GB energy. Therefore, a detailed analysis of the GB planes and the GB types was made.

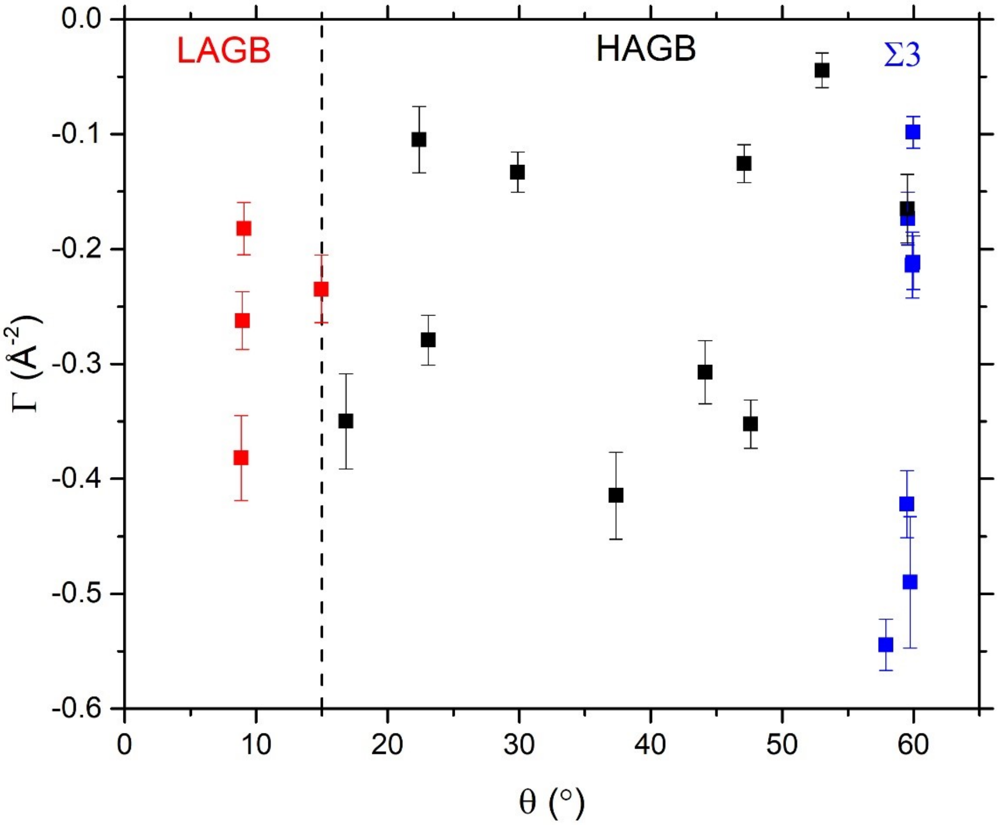

Figure 56: Solute excess Γ as a function of the misorientation angle ϑ for all GBs. The red squares represent the LAGBs whereas the HAGBs are marked black. A special type of HAGBs are the Σ3 GBs, which are the blue squares.

4.5.5 GB segregation: Dependency on the GB planes

The GB plane and the tilt and twist contribution of the GB were calculated as described in the previous chapters. The resulting GB plane normal as expressed for both grains, the misorientation axis and angle, the tilt axis and the tilt and twist angles are shown in Table 5. Note that all vectors are expressed as Miller indices with integer and their deviation from the absolute values are given in the table as an error. The Σ1- and Σ3-GBs were marked by red and blue shading.

First, the Σ1 were compared to each other. It can be seen that none of these GB has energy efficient planes or rotation axis. Except for Σ1 8.9° $[\bar{1}\ 0\ \bar{1}](\bar{2}\ \bar{6}\ 3)/(\bar{6}\ 3\ \bar{2})$, the GB plane normal are random and not symmetrical. The misorientation axis and the tilt axis are not identical, meaning the misorientation is not a pure tilt rotation. Σ1 8.9° $[\bar{1}\ 0\ \bar{1}](\bar{2}\ \bar{6}\ 3)/(\bar{6}\ 3\ \bar{2})$ has also random GB plane normals, however, they are symmetrical. Additionally, the misorientation axis is nearly a pure tilt axis. Nevertheless, the solute excess is highest. For an energy-efficient coherent GB, the relationship between rotation axis and GB plane plays an important role. Just, if the rotation leads to mirror symmetry with a smooth transition between the atoms of the adjacent grains, the energy is lowered. However, already small deviations from the mirror structure can lead to huge increases of the energy, which is probably the reason for this high segregation. This is observed for example for the incoherent Σ3 twin boundary in Cu [97].

Also in this study, we measured Σ3 GBs, which were, however, not twin boundaries since they were not coherent. Three Σ3 GBs were asymmetric with higher twist contribution, having low solute excesses ranging from -0.173 to -0.214 $Å^{-2}$. The lowest Γ is received for a symmetrical GB with nearly pure twist rotation. Whereas a symmetrical Σ3 GB with high tilt contribution has a high solute excess of -0.49 $Å^{-2}$, and with mixed rotation character, even the highest Γ of -0.545 $Å^{-2}$. For an asymmetric GB of pure tilt contribution, a high excess is also measured. Generally, it can be said, that the higher the twist compound, the lower the excess. Considering that a coherent twin GB can be created by pure twist rotation of 60° around the [111]-axis, this result shows that with increasing twist contribution, the energy-efficient coherent twin GB is reached.

Table 5: The resulting GB plane normal $\vec{n}_{G1}$ and $\vec{n}_{G2}$, misorientation axis $\vec{m}$ and tilt axis $\vec{n}_{ti}$ as Miller indices in integers with the deviations from their absolute orientation, together with the misorientation angle ϑ, the tilt angle Ψ and the twist angle Φ. The $\Sigma1$ GBs are shaded red, whereas the $\Sigma3$ GBs are marked in blue.

$\vec{n}_{G1}$	$\Delta\vec{n}_{G1}$	$\vec{n}_{G2}$	$\Delta\vec{n}_{G2}$	$\vec{m}$	$\Delta\vec{m}$	$\vec{n}_{ti}$	$\Delta\vec{n}_{ti}$	ϑ	ψ	Φ	Γ/Å^{-2}
$(\mathbf{3\ 6\ 4})$	1.88	$(\bar{1}\ 2\ \bar{3})$	1.95	$(6\ \bar{2}\ 1)$	1.61	$(2\ \bar{1}\ 0)$	2.15	9.1	8.9	1.9	-0.182
$(\mathbf{1\ \bar{3}\ 1})$	2.27	$(1\ \bar{1}\ 3)$	1.52	$(1\ \bar{1}\ \bar{1})$	0.84	$(1\ 0\ \bar{1})$	1.33	57.9	47.6	34.0	-0.545
$(\mathbf{5\ \bar{3}\ 1})$	2.33	$(1\ 5\ 0)$	3.43	$(\bar{1}\ 0\ 3)$	4.33	$(\bar{1}\ 0\ 5)$	0.61	29.9	29.4	5.3	-0.133
$(\mathbf{\bar{2}\ 1\ 4})$	0.70	$(\bar{5}\ 1\ 1)$	4.59	$(\bar{1}\ 6\ 1)$	2.44	$(\bar{1}\ 10\ \bar{3})$	1.29	16.8	15.2	7.3	-0.350
$(\mathbf{3\ 0\ 1})$	3.41	$(1\ \bar{1}\ \bar{1})$	1.76	$(1\ \bar{2}\ 6)$	3.61	$(\bar{1}\ \bar{3}\ 4)$	1.65	47.1	41.4	23.0	-0.126
$(\mathbf{\bar{1}\ \bar{3}\ \bar{3}})$	3.54	$(\bar{4}\ 6\ 1)$	0.54	$(\bar{1}\ 1\ \bar{1})$	1.56	$(\bar{1}\ 1\ \bar{1})$	5.87	59.5	59.3	5.4	-0.422
$(\mathbf{4\ 3\ \bar{1}})$	0.44	$(4\ \bar{2}\ 3)$	2.50	$(\bar{1}\ 2\ \bar{1})$	4.03	$(\bar{2}\ 2\ \bar{1})$	4.22	23.1	22.0	6.9	-0.279
$(\mathbf{1\ \bar{1}\ 0})$	4.34	$(4\ \bar{4}\ \bar{1})$	1.40	$(1\ 4\ 2)$	0.79	$(3\ 3\ 2)$	3.77	9.0	7.6	4.7	-0.262
$(\mathbf{\bar{2}\ \bar{9}\ \bar{5}})$	0.73	$(1\ 8\ \bar{3})$	2.05	$(\bar{7}\ \bar{6}\ 0)$	1.53	$(\bar{2}\ 0\ 1)$	2.02	15.0	10.8	10.4	-0.235
$(\mathbf{\bar{5}\ 8\ 1})$	1.23	$(3\ 1\ \bar{6})$	1.25	$(1\ \bar{1}\ \bar{1})$	1.18	$(2\ 2\ \bar{3})$	3.90	59.6	30.4	51.8	-0.173
$(\mathbf{1\ \bar{4}\ 1})$	1.95	$(0\ 5\ \bar{4})$	2.47	$(\bar{1}\ 1\ \bar{1})$	2.76	$(\bar{4}\ \bar{1}\ \bar{1})$	2.20	60.0	35.3	49.3	-0.212
$(\mathbf{3\ \bar{1}\ \bar{9}})$	0.80	$(7\ 1\ 5)$	0.55	$(2\ \bar{1}\ \bar{2})$	3.20	$(2\ \bar{3}\ 1)$	1.77	53.0	22.0	48.5	-0.045
$(\mathbf{\bar{1}\ \bar{1}\ 8})$	1.25	$(\bar{6}\ 0\ 7)$	2.28	$(6\ 4\ \bar{7})$	0.52	$(10\ 1\ 1)$	1.55	59.5	34.1	49.6	-0.165
$(\mathbf{\bar{3}\ \bar{2}\ \bar{1}})$	2.90	$(\bar{1}\ \bar{2}\ \bar{3})$	1.39	$(\bar{1}\ \bar{1}\ \bar{1})$	1.50	$(1\ \bar{1}\ \bar{1})$	2.84	60.0	19.9	56.9	-0.098
$(\mathbf{\bar{2}\ 1\ \bar{5}})$	1.80	$(2\ \bar{3}\ \bar{2})$	2.52	$(1\ 5\ \bar{3})$	1.89	$(5\ 6\ \bar{1})$	0.47	47.6	39.3	27.4	-0.352
$(\mathbf{\bar{2}\ \bar{6}\ 3})$	4.50	$(\bar{6}\ 3\ \bar{2})$	4.67	$(\bar{1}\ 0\ \bar{1})$	1.88	$(\bar{1}\ 0\ \bar{1})$	4.97	8.9	8.8	0.6	-0.382
$(\mathbf{\bar{5}\ 5\ \bar{1}})$	1.63	$(\bar{1}\ \bar{1}\ \bar{7})$	2.83	$(2\ \bar{1}\ 4)$	1.05	$(\bar{1}\ 1\ 10)$	0.95	44.2	35.1	27.2	-0.307
$(\mathbf{\bar{1}\ \bar{4}\ 5})$	2.02	$(\bar{8}\ 0\ 1)$	3.00	$(\bar{7}\ 1\ \bar{1})$	2.63	$(\bar{7}\ 1\ \bar{1})$	2.81	37.4	37.3	2.2	-0.415
$(\mathbf{\bar{3}\ 1\ \bar{1}})$	1.99	$(\bar{1}\ 1\ \bar{3})$	1.41	$(\bar{1}\ 1\ 1)$	1.34	$(0\ 1\ 1)$	1.81	59.7	51.8	30.9	-0.490
$(\mathbf{4\ \bar{1}\ 6})$	0.55	$(3\ 1\ 0)$	1.16	$(\bar{1}\ \bar{1}\ \bar{1})$	1.66	$(\bar{2}\ \bar{3}\ 1)$	1.65	59.9	41.4	44.3	-0.214
$(\mathbf{\bar{2}\ \bar{1}\ 0})$	2.73	$(\bar{1}\ 1\ \bar{2})$	4.26	$(\bar{1}\ 3\ 0)$	2.18	$(\bar{1}\ 2\ 0)$	3.02	22.4	22.2	3.3	-0.105

The random HAGBs have excesses between -0.045 and -0.415 Å^{-2}. None of these GBs are symmetric, however, one GB has a {111} GB plane, which is assumed to be an energy-efficient GB plane. This explains the lower solute segregation of -0.126 Å^{-2} of the GB 47.1° $[1\ \bar{2}\ 6](3\ 0\ 1)/$

$(1\,\bar{1}\,\bar{1})$. Some GBs have a nearly pure tilt rotation, but this seems to have no influence on the segregation behavior.

4.5.6 GB segregation: Dependency on tilt and twist contribution

As seen in the last chapter, misorientation consists of different amounts of tilt and twist contributions. To analyze the influence of the tilt and twist angles on the segregation behavior, the ratio between the twist angle and misorientation angle was calculated and plotted for the solute excess Γ in Figure 57. The absolute excess increases nearly linear to a twist contribution of 0.5. Here, the excess varies significantly from -0.126 to -0.49 $Å^{-2}$. Then, the excess reduces again linearly. Herein the LAGB and Σ3 GB, which were marked in red and blue, have the same behavior as the random HAGBs. It can be seen that the segregation for pure tilt and twist rotation is low and increase linearly with the contribution of the other component. So, at maximal mixing of both compounds, also the segregation is maximal.

A deviation of this general behavior is only observed for a twist ratio lower than 0.1. Here, for three GBs, excesses of around -0.4 $Å^{-2}$ were found, which are not fitting to the general trend, but are obviously higher. It seems like having a tilt contribution of more than 90%, with nearly no twist contribution lead to an increased segregation. Adding already a slightly more twist rotation to the nearly pure tilt rotation reduces the excess to just a quarter of the value, to -0.1 $Å^{-2}$ at a ratio of 0.15. The high segregation for nearly pure tilt GBs may be also the reason why none of them were observed in this project, having similar solid segregations as the highly mixed GBs. However, a similar behavior for large twist contributions was not observed. Here, a twist contribution of nearly 95% still shows a reduced excess of around -0.1 $Å^{-2}$. This might come from the energetic difference of tilt and twist GBs. Theoretically, the twist rotation consists of two sets of screw dislocations, whereas an asymmetric tilt GB is made up by two sets of edge dislocations. In terms of energy, screw dislocations require slightly less effort as:

$$E_{screw} = \frac{G \cdot b^2}{4\pi} \cdot ln\frac{R}{r_0} \tag{48.1}$$

$$E_{edge} = \frac{G \cdot b^2}{4\pi(1-\nu)} \cdot ln\frac{R}{r_0}. \tag{48.2}$$

With G as the shear modulus, b as the Burgers vector, r_0 as the dislocation core radius, R as the crystal radius and ν as the Poisson ratio, which is $\nu = \frac{1}{3} = 0.3 \ldots 0.4$ [98]. This might be the reason why pure tilt GBs have larger segregation than mixed, but pure twist boundaries do not.

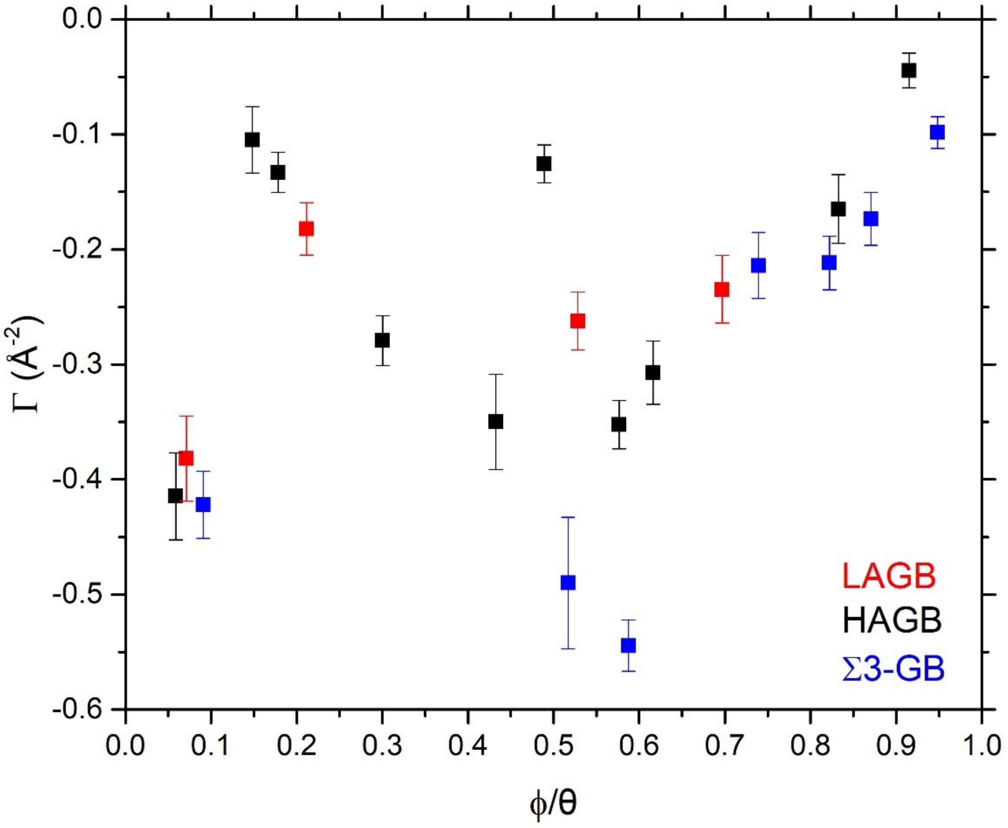

Figure 57: Solute excess as a function of the ratio between twist and misorientation angle. The red squares are the LAGBs, whereas the Σ3 GB are marked blue.

The dependency of a symmetrical [110]-tilt GB from the tilt angle was given in a review article from Rohrer [99] in Figure 58. He compared Cu GBs from [100] and an Al GBs from [101], coming to the result, that the behavior is the same for both. Herein, the relative GB energy shows a significant decrease at 70° for the coherent twin, whereas the other angles have energies between 0.6 and 1. Some symmetrical [110]-tilt GB were also measured in this work (No. 2, 16 and 19 in Table 5). Their tilt angle corresponds to the high-energetic GBs, which is also confirmed by their huge solute segregation.

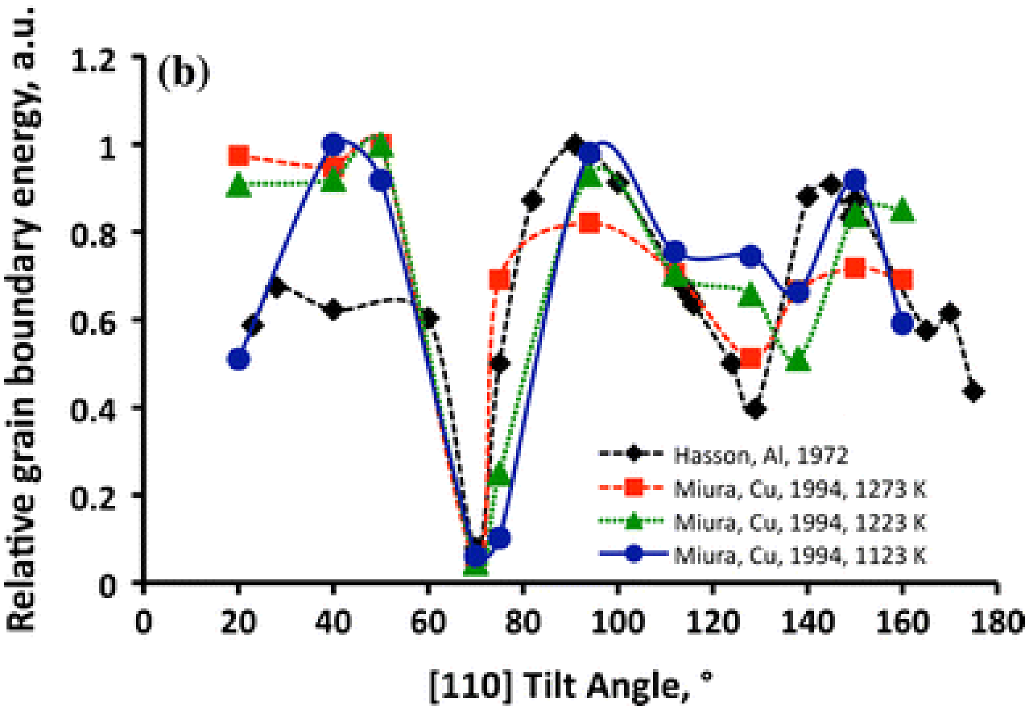

Figure 58: GB energy data as a function of the tilt angle for a symmetric [110]-tilt GB in Al and Cu from Ref. [99]

For twist GBs, an energetic minimum at 60° is observed for a [111]-twist GB [99]. In our work, this combination was found quite often for the misorientation axis and angle (see Table 5). However, by neglecting the GBs with huge mixed contributions and by considering just the twist rotation to be around 60°, only GB no. 14 is left. This GB is symmetrical and has a low solute segregation, indicating a symmetrical Σ3 twist GB.

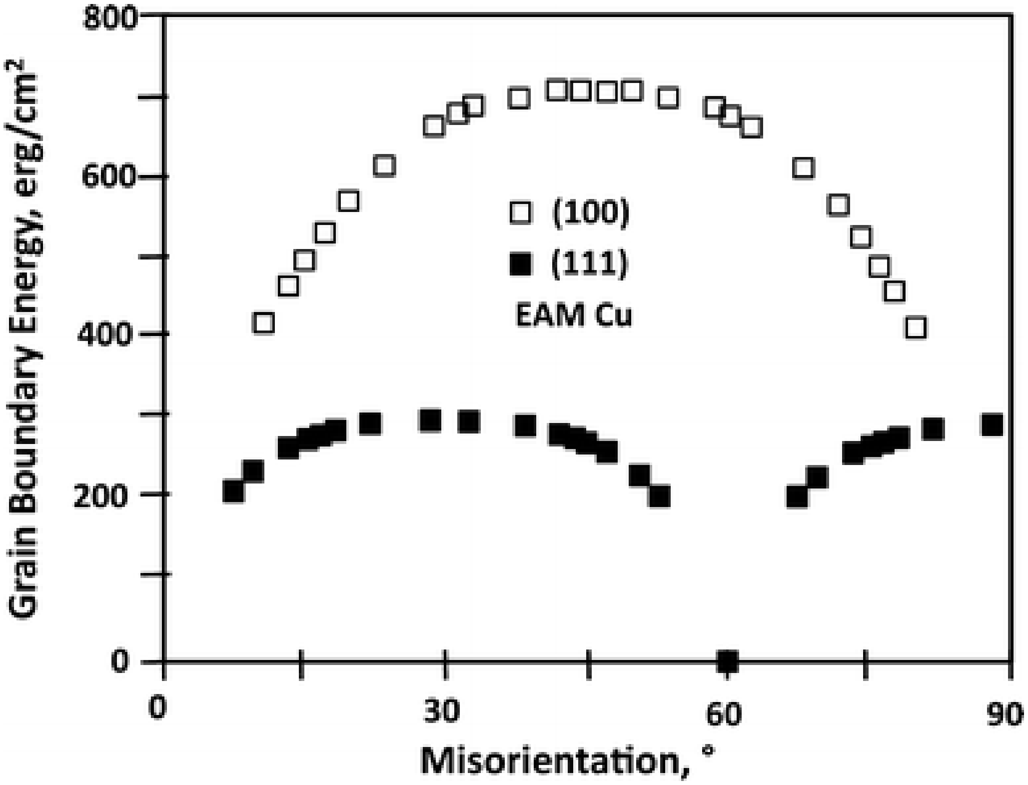

Figure 59: GB energy data for [100] and [111] twist boundaries as a function of the twist angle from Ref. [99]

5 Summary and conclusion

In this work, atom probe tomography was used to investigate thermodynamics and GB segregation in nanocrystalline CuNi thin films.

In the first part of the work, an approach for direct measurement of the miscibility gap phase boundaries was introduced. The extremely slow kinetics of this alloy were circumvented by using samples with a nanometer-sized multilayer stack of pure Cu and pre-alloyed CuNi layers containing 30 at.% Cu. Using three different annealing temperatures, isothermal treatments of different durations, the critical temperature T_C of the miscibility gap was localized. For this, concentration profiles of the layer structure were fitted according to phenomenological models, representing the diffusion-controlled intermixing or the stabilization of phase boundaries according to Cahn-Hilliard. At 573K, a clear deviation from diffusional mixing was established, giving clear evidence for the existence of phase separation. At this temperature, the phase boundaries are localized at c_{Ni}=26 at.% and c_{Ni}= 65.7 at.%. Using this information, the whole miscibility gap phase boundary could be calculated by a Redlich-Kister polynomial for the Gibbs free energy parametrization as shown in Figure 42. With this, the T_C was found to be 608 K which confirms earlier findings from Ref. [76, 83, 74]. But even newer most recent experimental data [17], show huge disagreement, which was shown in the present work to be due to the use of insufficient annealing time in this alternative work.

At the same time, an effective diffusion coefficient D_{eff} was determined, to ensure that the samples reached thermodynamic equilibrium and the mixing procedure was completed. This was found to be $D_{eff}=1.86 \cdot 10^{-10}\ m^2s^{-1} \cdot \exp(-164kJ/molRT)$, which is very close to measurements of diffusion of Cu in nanocrystalline Ni [18]. This clearly demonstrates that mixing is controlled by diffusion in Ni. The reason for this is that the diffusion of Cu into Ni is way slower, and therefore the rate-determining process.

During the diffusional mixing, the change in the microstructure of the samples could be observed. The fast diffusion along grain boundaries is clearly seen (see Figure 37). These defects are also involved in the nucleation growth, known as the DIGM mechanism.

In the second part of the work, GB segregation was characterized by atomic resolution analysis. Therefore, alloy layers with four different concentrations, c_{Ni} = 0.25, 0.60, 0.70 and 0.85, were prepared and annealed for 24 h at 700 K. In total, 70 GBs could be successfully evaluated. The density fluctuations being usual for APT measurements could be homogenized by using an original MD approach for density correction. The solute segregation was defined over the solute excess Γ, according to Cahn which represents a robust characteristic parameter, being suitable for thermodynamic considerations. The solute excesses, found in this work range from of 0.044 to 1.28 $\mathrm{Å}^{-2}$, in dependency on the bulk concentration and are way larger than atomistic predictions made for a $\Sigma 5$ GB in [9]. The highest segregation is received for a concentration of c_{Ni} = 0.75.

With the experimental data, the effective segregation parameter was fitted and the solute excess was calculated over the whole composition range, according to an extension of the Langmuir-McLean segregation model made in [9]. Comparing the resulting Γ-curve to the atomistic data of a simulated $\Sigma 5$ GB, the dependency is similar, but with generally higher excesses for the experiment.

This was further analysed by calculating the difference in the GB formation energy $\Delta\gamma$(c = 1), using different parametrizations for the Gibbs free energy. The value found for the experimental GBs is $\Delta\gamma$(c = 1) = 0.81 Jm^{-2} and exceeds the one for the atomistic prediction, being $\Delta\gamma$(c = 1) = 0.36 Jm^{-2}. The discrepancy comes probably from the fact, that the GB used for the atomistic prediction is a low-energetic GB, whereas the GBs in the experiment are high-energetic natural GBs, having deviations from ideal GB orientations.

Further, the segregation widths for all measured GBs were analysed. The values range from 12 to 85 Å. For each alloy concentration, a linear relationship between the GB widths and the solute excess was found. Interestingly, the slope of this linearity depends on the bulk concentration, where concentrations with higher solute segregation show lower slopes. This behaviour might be explained by the evaporation field differences between bulk and GB, and is therefore probably a measurement artefact, caused by trajectory overlaps of GB atoms with bulk atoms. The artefact will diminish with decreasing segregation amplitude. Thus for GBs with no segregation, trajectory aberrations can be neglected. By extrapolation, the structural GB width is so found to be w_0 = (10.1 ± 1.5) Å.

With an additional tEBSD measurement step during APT sample preparation, the grain orientations were determined. Using this information, and by correlating GB plane orientation calculations from APT measurements, the GB orientation was determined for 21 GBs with a bulk concentration of $c_{\mathrm{Ni}} = 0.6$. By plotting the solute excess as a function of the misorientation angle, and by splitting the GBs into groups of LAGBs, $\Sigma3$-GBs and random GBs, a dependency of the segregation strength from GB orientation was evaluated. However, a direct correlation between the segregation and the misorientation was not observed. Further information about the GB plane orientation is received by distinguishing the tilt and twist contribution to the GB. Most investigated GBs have a mixed contribution of tilt and twist rotation. Remarkably, the solid segregation increases, the higher the mixing of the tilt/twist rotation is, with the highest segregation amplitudes for the equal ratio.

6 Bibliography

[1] H. Gleiter, "Nanostructured materials: basic concepts and microstructure," *Acta Materialia,* vol. 48, p. 1–29, January 2000.

[2] P. Lejcek, Grain Boundary Segregation in Metals, Springer Berlin Heidelberg, 2010.

[3] H. L. Skriver and N. M. Rosengaard, "Surface energy and work function of elemental metals," *Physical Review B,* vol. 46, p. 7157–7168, 9 1992.

[4] C. L. Briant, Impurities in Engineering Materials, C. Briant, Ed., Routledge, 2017.

[5] J. C. Walmsley, G. Jones, B. J. Lee and R. K. Wild, "High resolution imaging and analysis of grain boundaries in steel using a field emission auger microprobe," *Applied Surface Science,* vol. 108, p. 289–295, 2 1997.

[6] J. Cho, C. M. Wang, H. M. Chan, J. M. Rickman and M. P. Harmer, "Role of segregating dopants on the improved creep resistance of aluminum oxide," *Acta Materialia,* vol. 47, p. 4197–4207, 11 1999.

[7] P. Williams, C. A. Evans, M. L. Grossbeck and H. K. Birnbaum, "Ion microprobe analysis for niobium hydride in hydrogen-embrittled niobium," *Analytical Chemistry,* vol. 48, p. 964–968, 6 1976.

[8] F. Fischer, G. Schmitz and S. M. Eich, "A systematic study of grain boundary segregation and grain boundary formation energy using a new copper–nickel embedded-atom potential," *Acta Mater.,* vol. 176, p. 220–231, September 2019.

[9] F. Fischer and S. M. Eich, "Analytic description of grain boundary segregation, tension, and formation energy in the copper–nickel system," *Acta Materialia,* vol. 201, p. 364–372, December 2020.

[10] M. A. Tschopp and D. L. Mcdowell, "Asymmetric tilt grain boundary structure and energy in copper and aluminium," *Philosophical Magazine,* vol. 87, p. 3871–3892, 9 2007.

[11] M. Herbig, D. Raabe, Y. Li, P. Choi, S. Zaefferer and S. Goto, "Atomic-Scale Quantification of Grain Boundary Segregation in Nanocrystalline Material," *Physical Review Letters,* vol. 112, 3 2014.

[12] D. Palanisamy, D. Raabe and B. Gault, "Elemental segregation to twin boundaries in a MnAl ferromagnetic Heusler alloy," *Scripta Materialia,* vol. 155, p. 144–148, 10 2018.

[13] K. Babinsky, R. De Kloe, H. Clemens and S. Primig, "A novel approach for site-specific atom probe specimen preparation by focused ion beam and transmission electron backscatter diffraction," *Ultramicroscopy,* vol. 144, p. 9–18, 2014.

[14] M. Asta and S. M. Foiles, "Embedded-atom-method effective-pair-interaction study of the structural and thermodynamic properties of Cu-Ni, Cu-Ag, and Au-Ni solid solutions," *Physical Review B,* vol. 53, p. 2389–2404, 2 1996.

[15] L. Elford, F. Müller and O. Kubaschewski, "The thermodynamic properties of copper-nickel alloys," *Berichte der Bunsengesellschaft für physikalische Chemie,* vol. 73, pp. 601-605, 1969.

[16] S. Srikanth and K. T. Jacob, "Thermodynamic properties of Cu–Ni alloys: measurements and assessment," *Materials Science and Technology,* vol. 5, p. 427–434, 5 1989.

[17] Y. Iguchi, G. L. Katona, C. Cserháti, G. A. Langer and Z. Erdélyi, "On the miscibility gap of Cu-Ni system," *Acta Materialia,* vol. 148, p. 49–54, April 2018.

[18] B. C. Johnson, C. L. Bauer and A. G. Jordan, "Mechanisms of interdiffusion in copper/nickel thin-film couples," vol. 59, p. 1147–1155, February 1986.

[19] H. Böhm, Einführung in die Metallkunde, vol. 196, Mannheim: B.I.-Wissenschaftsverlag, 1968, p. 235.

[20] E. Hornbogen and H. Warlimont, Metallkunde, Springer Berlin Heidelberg, 2001.

[21] D. A. Porter, K. E. Easterling and K. E. Easterling, Phase Transformations in Metals and Alloys (Revised Reprint), CRC Press, 2009.

[22] U. R. Kattner, "THE CALPHAD METHOD AND ITS ROLE IN MATERIAL AND PROCESS DEVELOPMENT," *Tecnologia em Metalurgia Materiais e Mineração,* vol. 13, p. 3–15, 2016.

[23] H. L. Lukas, J. Weiss and E.-T. Henig, "Straegies for the calculation of phase diagrams," *Calphad,* vol. 6, p. 229–251, July 1982.

[24] O. Kubaschewski, H. Villa and W. A. Dench, "The reaction of titanium tetrachloride with hydrogen in contact with various refractories," *Transactions of the Faraday Society,* vol. 52, p. 214, 1956.

[25] O. Redlich and A. T. Kister, "Algebraic Representation of Thermodynamic Properties and the Classification of Solutions," *Industrial and Engineering Chemistry,* vol. 40, p. 345–348, February 1948.

[26] R. Duran, P. Stender, S. M. Eich and G. Schmitz, "Atom Probe Study of the Miscibility Gap in CuNi Thin Films and Microstructure Development," *Microscopy and Microanalysis,* p. 1–11, November 2021.

[27] J. W. Cahn and J. E. Hilliard, "Free Energy of a Nonuniform System. I. Interfacial Free Energy," *The Journal of Chemical Physics,* vol. 28, p. 258–267, February 1958.

[28] H. Mehrer, Diffusion in Solids, Springer Berlin Heidelberg, 2007.

[29] A. H. King, "Diffusion induced grain boundary migration," *International Materials Reviews,* vol. 32, p. 173–189, January 1987.

[30] G. Gottstein and L. S. Shvindlerman, Grain Boundary Migration in Metals, CRC Press, 2009.

[31] H. Briehl, Chemie der Werkstoffe, Springer Fachmedien Wiesbaden, 2014.

[32] O. Engler and V. Randle, Introduction to Texture Analysis, CRC Press, 2009.

[33] M. Furtkamp, P. Lejček and S. Tsurekawa, *Interface Science,* vol. 6, p. 59–66, 1998.

[34] T. Gorkaya, D. A. Molodov and G. Gottstein, "Stress-driven migration of symmetrical 〈100〉 tilt grain boundaries in Al bicrystals," *Acta Materialia,* vol. 57, p. 5396–5405, October 2009.

[35] R. Valerie, Measurement of Grain Boundary Geometry, S.l: CRC PRESS, 2019.

[36] A. V. Andrejeva, G. I. Salnikov and L. K. Fionova, "Grain boundary faceting in niobium of high purity," *Acta Metallurgica,* vol. 26, p. 1331–1336, September 1978.

[37] S. Mandal, K. G. Pradeep, S. Zaefferer and D. Raabe, "A novel approach to measure grain boundary segregation in bulk polycrystalline materials in dependence of the boundaries' five rotational degrees of freedom," *Scripta Materialia,* vol. 81, p. 16–19, June 2014.

[38] J. W. Gibbs, "On the Equilibrium of Heterogeneous Substances," 2012.

[39] J. W. Gibbs, "On the equilibrium of heterogeneous substances," *Trans. Conn. Acad. Arts Sci.,* vol. 3, p. 108–248, 1874.

[40] T. Frolov and Y. Mishin, "Thermodynamics of coherent interfaces under mechanical stresses. I. Theory," *Phys. Rev. B,* vol. 85, p. 224106, 2012.

[41] T. Frolov and Y. Mishin, "Thermodynamics of coherent interfaces under mechanical stresses. II. Application to atomistic simulation of grain boundaries," *Phys. Rev. B,* vol. 85, p. 224107, 2012.

[42] J. W. Cahn, "Thermodynamics of solid and fluid surfaces," in *The selected works of John Cahn*, W. C. Carter and W. C. Johnson, Eds., John Wiley & Sons, Inc., 1978, p. 379–399.

[43] D. McLean, Grain boundaries in metals, Clarendon Press, 1957.

[44] T. Krauß and S. M. Eich, "Development of a segregation model beyond McLean based on atomistic simulations," *Acta Materialia,* vol. 187, p. 73–83, April 2020.

[45] E. D. Hondros and M. P. Seah, "The theory of grain boundary segregation in terms of surface adsorption analogues," *Metallurgical Transactions A,* vol. 8, p. 1363–1371, 9 1977.

[46] G. Kaptay, "Modelling equilibrium grain boundary segregation, grain boundary energy and grain boundary segregation transition by the extended Butler equation," *Journal of Materials Science,* vol. 51, p. 1738–1755, 11 2015.

[47] D. McLean, "Grain boundaries in metals".

[48] M. P. Seah, "Grain boundary segregation," *Journal of Physics F: Metal Physics,* vol. 10, p. 1043–1064, 6 1980.

[49] G. Rowlands and D. P. Woodruff, "The kinetics of surface and grain boundary segregation in binary and ternary systems," *Philosophical Magazine A,* vol. 40, p. 459–476, 10 1979.

[50] M. Binnewies, M. Finze, M. Jäckel, P. Schmidt, H. Willner, G. Rayner-Canham and G. Rayner-Canham, "Die Nebengruppenelemente," in *Allgemeine und Anorganische Chemie*, Springer Berlin Heidelberg, 2016, p. 753–846.

[51] E. Riedel and C. Janiak, Anorganische Chemie, DE GRUYTER, 2015.

[52] F. Fischer, "Correlative study of grain boundary segregation in nanocrystalline copper-nickel alloys," University of Stuttgart, Stuttgart, 2020.

[53] „institut-seltene-erden.de,“ [Online]. Available: https://institut-seltene-erden.de/seltene-erden-und-metalle/basismetalle/nickel/. [Zugriff am 2 December 2022].

[54] C. Huang, "Metallurgical knowledge transfer from Asia to Europe," *Artefact,* p. 89–110, 12 2018.

[55] L. Yang, Y. Zhao, C. Feng and H. Zhou, "The Influence of Size Effect on Sensitivity of Cu/CuNi Thin-film Thermocouple," *Physics Procedia,* vol. 22, p. 95–100, 2011.

[56] S.-G. Hur, D.-J. Kim, B.-D. Kang and S.-G. Yoon, "Effect of the deposition temperature on temperature coefficient of resistance in CuNi thin film resistors," *Journal of Vacuum Science & Technology B: Microelectronics and Nanometer Structures,* vol. 22, p. 2698, 2004.

[57] A.-S. Lucier, "Preparation and Characterization of Tungsten Tips Suitable for Molecular Electronics Studies," 2004.

[58] M. Nave, "Materials Science of Electrochemical Formation of Tungsten Nanosharp Probes," 2014.

[59] P. Stender, "Thermal stability investigation of a nanocrystalline Iron – Chromium multilayer system," 2010.

[60] D. McKie and C. McKie, "Essentials of Crystallography. Blackwell Scientific Publications, Oxford 1992. 437 p., pbk. L 19.50. ISBN 0-632-01574-8.," *Crystal Research and Technology,* vol. 28, no. 6, 1993.

[61] A. D. Herron, S. P. Coleman, K. Q. Dang, D. E. Spearot and E. R. Homer, "Simulation of kinematic Kikuchi diffraction patterns from atomistic structures," *MethodsX,* vol. 5, 2018.

[62] G. C. Sneddon, P. W. Trimby and J. M. Cairney, "Transmission Kikuchi diffraction in a scanning electron microscope: A review," vol. 110, p. 1–12, December 2016.

[63] R. Schlesiger, C. Oberdorfer, R. Würz, G. Greiwe, P. Stender, M. Artmeier, P. Pelka, F. Spaleck and G. Schmitz, "Design of a laser-assisted tomographic atom probe at Münster University," vol. 81, p. 043703, April 2010.

[64] B. Gault, M. P. Moody, J. M. Cairney and S. P. Ringer, Atom Probe Microscopy, Springer-Verlag GmbH, 2012.

[65] M. K. Miller, A. Cerezo and M. G. Hetherington, Atom Probe Field Ion Microscopy, OXFORD UNIV PR, 1996.

[66] P. Bas, A. Bostel, B. Deconihout and D. Blavette, "A general protocol for the reconstruction of 3D atom probe data," *Applied Surface Science,* Vols. 87-88, p. 298–304, March 1995.

[67] B. P. Geiser, T. F. Kelly, D. J. Larson, J. Schneir and J. P. Roberts, "Spatial Distribution Maps for Atom Probe Tomography," vol. 13, p. 437–447, November 2007.

[68] T. J. Prosa, B. P. Geiser, D. Lawrence, D. Olson and D. J. Larson, "Developing detection efficiency standards for atom probe tomography," 2014.

[69] D. R. Kingham, "The post-ionization of field evaporated ions: A theoretical explanation of multiple charge states," *Surface Science,* vol. 116, p. 273–301, 4 1982.

[70] C. Matano, "X-Ray Studies on the Diffusion of Copper into Nickel," *Memoirs of the College of Science, Kyoto Imperial University. Series A, 15 (6),* pp. 351-353, 1932.

[71] M. S. Anand, S. P. Murarka and R. P. Agarwala, "Diffusion of Copper in Nickel and Aluminum," *Journal of Applied Physics,* vol. 36, p. 3860–3862, December 1965.

[72] H. Helfmeier and M. Feller-Kniepmeier, "Diffusion of Copper in Nickel Single Crystals," *Journal of Applied Physics,* vol. 41, p. 3202–3205, July 1970.

[73] O. Redlich and A. Kister, "Algebraic representation of thermodynamic properties and the classification of solutions," *Industrial and Engineering Chemistry,* vol. 40, pp. 345-348, 1948.

[74] M. A. Turchanin, P. G. Agraval and A. R. Abdulov, "Phase equilibria and thermodynamics of binary copper systems with 3d-metals. VI. Copper–nickel system," *Powder Metall. Met. Ceram.,* vol. 46, p. 467–477, 2007.

[75] J. L. Meijering, "Calculation of the nickel-chromium-copper phase diagram from binary data," *Acta Metallurgica,* vol. 5, p. 257–264, May 1957.

[76] R. E. Pawel and E. E. Stansbury, "The specific heat of copper, nickel and copper-nickel alloys," *Journal of Physics and Chemistry of Solids,* vol. 26, p. 607–613, March 1965.

[77] B. Mozer, D. T. Keating and S. C. Moss, "Neutron Measurement of Clustering in the Alloy CuNi," *Physical Review,* vol. 175, p. 868–876, November 1968.

[78] J. Vrijen and C. Dijk, "Clustering and Spinodal Decomposition in Cu-Ni Alloys," in *Fluctuations, Instabilities, and Phase Transitions*, Springer US, 1975, p. 43–52.

[79] P. C. Clapp and S. C. Moss, "Correlation Functions of Disordered Binary Alloys. I," *Physical Review,* vol. 142, p. 418–427, February 1966.

[80] W. Wagner, R. Poerschke and H. Wollenberger, "Short-range clustering and long-range periodic decomposition of an electron irradiated Ni-Cu alloy," *Journal of Physics F: Metal Physics,* vol. 12, p. 405–424, March 1982.

[81] M. F. Ebel, "X-ray measurements on spinodal decomposition in Cu⍰Ni alloys," *Physica Status Solidi (a),* vol. 5, p. 91–94, April 1971.

[82] V. M. Lopez, T. Sakurai and K. Hirano, "A study of phase separation in Cu-Ni alloys by AP-FIM," *Scripta Metallurgica et Materialia,* vol. 26, p. 99–103, January 1992.

[83] T. Tsakalakos, "Spinodal decomposition in Cu⍰Ni alloys by artificial composition modulation technique," *Scripta Metallurgica,* vol. 15, p. 255–258, March 1981.

[84] T. J. A. Aalders, Short-range clustering and decomposition in copper-nickel-and c....

[85] B. N. Dey, "Interpretation of the damping behavior of copper-nickel alloys: Existence of a miscibility gap," *Scripta Metallurgica,* vol. 2, p. 501–506, 9 1968.

[86] B. Coles, "The lattice spacings of Nickel-Copper and Palladium-Silver alloys," *Journal of the institue of metals,* vol. 84, p. 346, 1955.

[87] L. Priester, Grain Boundaries, Springer Netherlands, 2013.

[88] E. Pellicer, A. Varea, K. M. Sivaraman, S. Pané, S. Surinach, M. D. Baró, J. Nogués, B. J. Nelson and J. Sort, "Grain boundary segregation and interdiffusion effects in nickel–copper alloys: an effective means to improve the thermal stability of nanocrystalline nickel," *ACS applied materials & interfaces,* vol. 3, p. 2265–2274, 2011.

[89] Y. Champion and M. J. Hÿtch, "Evidence for crystallographically abrupt grain boundaries in nanocrystalline copper," *The European Physical Journal Applied Physics,* vol. 4, p. 161–164, 1998.

[90] J. Fiebig, S. Divinski, H. Rösner, Y. Estrin and G. Wilde, "Diffusion of Ag and Co in ultrafine-grained α-Ti deformed by equal channel angular pressing," *Journal of Applied Physics,* vol. 110, p. 083514, 2011.

[91] M. R. Chellali, Z. Balogh, H. Bouchikhaoui, R. Schlesiger, P. Stender, L. Zheng and G. Schmitz, "Triple Junction Transport and the Impact of Grain Boundary Width in Nanocrystalline Cu," *Nano Letters,* vol. 12, p. 3448–3454, June 2012.

[92] R. Hu, G. D. W. Smith and E. A. Marquis, "Atom probe study of radiation induced grain boundary segregation/depletion in a Fe-12%Cr alloy," *Progress in Nuclear Energy,* vol. 57, p. 14–19, May 2012.

[93] T. Toyama, Y. Nozawa, W. V. Renterghem, Y. Matsukawa, M. Hatakeyama, Y. Nagai, A. A. Mazouzi and S. V. Dyck, "Grain boundary segregation in neutron-irradiated 304 stainless steel studied by atom probe tomography," *Journal of Nuclear Materials,* vol. 425, p. 71–75, June 2012.

[94] X. Xu, Y. Liu, J. Wang, D. Isheim, V. P. Dravid, C. Phatak and S. M. Haile, "Variability and origins of grain boundary electric potential detected by electron holography and atom-probe tomography," *Nature Materials,* vol. 19, p. 887–893, April 2020.

[95] C. Oberdorfer, S. M. Eich and G. Schmitz, "A full-scale simulation approach for atom probe tomography," *Ultramicroscopy,* vol. 128, p. 55–67, May 2013.

[96] D. Prokoshkina, V. A. Esin, G. Wilde and S. V. Divinski, "Grain boundary width, energy and self-diffusion in nickel: effect of material purity," *Acta Materialia,* vol. 61, p. 5188–5197, 2013.

[97] U. Wolf, F. Ernst, T. Muschik, M. W. Finnis and H. F. Fischmeister, "The Influence of Grain Boundary Inclination on the Structure and Energy of Σ3 Twin Boundaries in Copper," vol. 238, 1991.

[98] D. Hull and D. J. Bacon, Introduction to Dislocations, Elsevier, 2011.

[99] G. S. Rohrer, "Grain boundary energy anisotropy: a review," *Journal of Materials Science,* vol. 46, p. 5881–5895, September 2011.

[100] H. Miura, M. Kato and T. Mori, "Temperature dependence of the energy of Cu [110] symmetrical tilt grain boundaries," *Journal of Materials Science Letters,* vol. 13, p. 46–48, January 1994.

[101] G. C. Hasson and C. Goux, "Interfacial energies of tilt boundaries in aluminium. Experimental and theoretical determination," *Scripta Metallurgica,* vol. 5, p. 889–894, October 1971.

[102] P. Stender, Z. Balogh and G. Schmitz, "Triple line diffusion in nanocrystalline Fe/Cr and its impact on thermal stability," *Ultramicroscopy,* vol. 111, p. 524–529, May 2011.

[103] T. J. Prosa and D. J. Larson, "Modern Focused-Ion-Beam-Based Site-Specific Specimen Preparation for Atom Probe Tomography," *Microscopy and Microanalysis,* vol. 23, p. 194–209, February 2017.

[104] K. P. Gupta, C. H. Cheng and P. A. Beck, "Low-Temperature Specific Heat of Ni-Base fcc Solid Solutions with Cu, Zn, Al, Si, and Sb," *Physical Review,* vol. 133, p. A203–A206, January 1964.

[105] W. T. Read and W. Shockley, "Dislocation Models of Crystal Grain Boundaries," *Physical Review,* vol. 78, p. 275–289, May 1950.

[106] F. Fischer, G. Schmitz and S. M. Eich, "A systematic study of grain boundary segregation and grain boundary formation energy using a new copper–nickel embedded-atom potential," *Acta Materialia,* vol. 176, p. 220–231, 9 2019.

[107] A. A. Hameda, "Miscibility gap in the copper-nickel system," Electrical and Computer Engineering, University of Windsor, Windsor, 1986.

[108] S. N. Zhevnenko, I. S. Petrov, D. Scheiber and V. I. Razumovskiy, "Surface and segregation energies of Ag based alloys with Ni, Co and Fe: Direct experimental measurement and DFT study," *Acta Materialia,* vol. 205, p. 116565, 2 2021.

[109] P. Stender, Z. Balogh and G. Schmitz, "Triple junction segregation in nanocrystalline multilayers," *Physical Review B,* vol. 83, p. 121407, 3 2011.

[110] R. Shuttleworth, "The Surface Tension of Solids," *Proceedings of the Physical Society. Section A,* vol. 63, p. 444–457, 5 1950.

[111] N. J. Peter, M. J. Duarte, C. Kirchlechner, C. H. Liebscher and G. Dehm, *Faceting diagram for Ag segregation induced nanofaceting at an asymmetric Cu tilt grain boundary,* arXiv, 2020.

[112] T. Jeske and G. Schmitz, "Influence of the microstructure on the interreaction of Al/Ni investigated by tomographic atom probe," *Materials Science and Engineering: A,* vol. 327, p. 101–108, 4 2002.

[113] T. E. Hsieh and R. W. Balluffi, "Observations of roughening/de-faceting phase transitions in grain boundaries," *Acta Metallurgica,* vol. 37, p. 2133–2139, 8 1989.

[114] Z. Horita, D. J. Smith, M. Nemoto, R. Z. Valiev and T. G. Langdon, "Observations of grain boundary structure in submicrometer-grained Cu and Ni using high-resolution electron microscopy," *Journal of Materials Research,* vol. 13, p. 446–450, 2 1998.

[115] B. Gault, A. Chiaramonti, O. Cojocaru-Mirédin, P. Stender, R. Dubosq, C. Freysoldt, S. K. Makineni, T. Li, M. Moody and J. M. Cairney, "Atom probe tomography," *Nature Reviews Methods Primers,* vol. 1, 7 2021.

[116] S. M. Foiles, "Calculation of grain-boundary segregation in Ni–Cu alloys," *Phys. Rev. B,* vol. 40, p. 11502, 1989.

[117] C. de Boor, "A Practical Guide to Splines," in *Applied Mathematical Sciences*, 1978.

[118] https://www.inspico.eu/Software/Reconstruction-Scito/.

[119] M. R. Chellali, Z. Balogh and G. Schmitz, "Nano-analysis of grain boundary and triple junction transport in nanocrystalline Ni/Cu," *Ultramicroscopy,* vol. 132, p. 164–170, 9 2013.

[120] K. Babinsky, R. D. Kloe, H. Clemens and S. Primig, "A novel approach for site-specific atom probe specimen preparation by focused ion beam and transmission electron backscatter diffraction," *Ultramicroscopy,* vol. 144, p. 9–18, 9 2014.

[121] J. Vrijen and S. Radelaar, "Clustering in Cu-Ni alloys: A diffuse neutron-scattering study," *Physical Review B,* vol. 17, p. 409–421, January 1978.

[122] P. Stender, H. Solodenko, A. Weigel, I. Balla, T. M. Schwarz, J. Ott, M. Roussell, Y. Joshi, R. Duran, M. Al-Shakran, T. Jacob and G. Schmitz, "A Modular Atom Probe Concept: Design, Operational Aspects, and Performance of an Integrated APT-FIB/SEM Solution," *Microscopy and Microanalysis,* p. 1–13, January 2022.

[123] S. Pfeifer, P. Demirci, R. Duran, H. Stolpmann, A. Renfftlen, S. Nemrava, R. Niewa, B. Clauß and M. R. Buchmeiser, "Synthesis of zirconia toughened alumina (ZTA) fibers for high performance materials," *Journal of the European Ceramic Society,* vol. 36, p. 725–731, February 2016.

[124] R. Duran, F. Fischer, S. M. Eich, P. Stender and G. Schmitz, Quantitative Determination of Grain Boundary Segregation in Nanocrystalline CuNi alloys, submitted, 2022.

[125] H. Bubert, "Practical surface analysis A2, Vol. 1. Auger and X-ray photoelectron spectroscopy. 2. Auflage. Herausgegeben {vonD}. Briggs {undM}. P. Seah. Wiley, Chichester, Salle $\mathplus$ Sauerländer, Aarau, 1994. 649 S., Broschur 49.95 {\textsterling}. {\textendash} {ISBN} 0-471-9540-7," *Angewandte Chemie,* vol. 107, p. 1367–1367, 6 1995.

[126] F. Reniers and C. Tewell, "New improvements in energy and spatial (x, y, z) resolution in AES and XPS applications," *Journal of Electron Spectroscopy and Related Phenomena,* vol. 142, p. 1–25, 1 2005.

[127] H. L., Y. W. Liu, W. J. Tong, J. G. Lin and X. F. Wang, "Surface Energy Engineering of Cu Surface by Strain: First-Principles Calculations," *Surface Review and Letters,* vol. 20, p. 1350054, 12 2013.

[128] A. M. Manzoni, S. Haas, J. M. Yu, H. M. Daoud, U. Glatzel, H. Aboulfadl, F. Mücklich, R. Duran, G. Schmitz, D. M. Többens, S. Matsumura, F. Vogel and N. Wanderka, "Evolution of gamma/gammaprime phases, their misfit and volume fractions in Al10Co25Cr8Fe15Ni36Ti6 compositionally complex alloy," *Materials Characterization,* vol. 154, p. 363–376, August 2019.

[129] J. C. Love, F. E. Obenshain and G. Czjzek, "Mössbauer Spectroscopy with 61Ni in Nickel—Transition-Metal Alloys and Nickel Compounds," *Physical Review B,* vol. 3, p. 2827–2840, May 1971.

List of publications

1 Pfeifer, S., Demirci, P., Duran, R., Stolpmann, H., Renfftlen, A., Nemrava, S., Niewa, R., Clauß, B., Buchmeiser, M.
Synthesis of zirconia toughened alumina (ZTA) fibers for high performance materials
Journal of the European Ceramic Society 36 (2016) pp. 725–731

2 Manzoni, A. M., Haas, S., Yu, J. M., Daoud, H. M., Glatzel, U., Aboulfadl, H., Mücklich, F., Duran, R., Schmitz, G., Többens, D.M., Matsumura, S., Vogel, F., Wanderka, N.
Evolution of γ/γ' phases, their misfit and volume fractions in $Al_{10}Co_{25}Cr_8Fe_{15}Ni_{36}Ti_6$ compositionally complex alloy
Materials Characterization 154 (2019) pp. 363–376

3 Stender, P., Solodenko, H., Weigel, A., Balla, I., Schwarz, T. M., Ott, J., Roussel, M., Joshi, Y., Duran, R., Al-Shakran, M., Jacob, T., Schmitz, G.
A Modular Atom Probe Concept: Design, Operational Aspects, and Performance of an Integrated APT-FIB/SEM Solution
Microscopy and Microanalysis 28(4) (2021) pp. 1168-1180

4 Duran, R., Stender, P., Eich, S. M., & Schmitz, G.
Atom Probe Study of the Miscibility Gap in CuNi Thin Films and Microstructure Development
Microscopy and Microanalysis 28(4) (2021) pp. 1359-1369

5 Duran, R., Fischer, F., Eich, S. M., Stender, P., & Schmitz, G.
Quantitative Determination of Grain Boundary Segregation in Nanocrystalline CuNi alloys (submitted)